Thesis presented to the Instituto Tecnológico de Aeronáutica, in partial fulfillment of the requirements for the degree of Doctor of Science in the Graduate Program of Physic, Field of Nonlinear Dynamics and Complex Systems.

Alysson Brhian de Souza Muniz Silva

STATISTICAL STUDY OF GRAVITY WAVES IN THE LOWER ATMOSPHERE AND PREDICTIVE MODELING OF LOW LATITUDE IONOSPHERIC IRREGULARITIES

Thesis approved in its final version by signatories below:

gov.br
Documento assinado digitalmente
MARCO ANTONIO RIDENTI
Data: 18/01/2025 12:45:31-0300
Verifique em https://validar.iti.gov.br

Prof. Dr. Marco Antonio Ridenti
Advisor

Prof. Dr. Francisco Javier Azpilicueta
Co-advisor

Campo Montenegro
São José dos Campos, SP - Brazil
2024

Cataloging-in Publication Data
Documentation and Information Division

de Souza Muniz Silva, Alysson Brhian
Statistical Study of Gravity Waves in the Lower Atmosphere and Predictive Modeling of Low Latitude Ionospheric Irregularities / Alysson Brhian de Souza Muniz Silva.
São José dos Campos, 2024.
142f.

Thesis of Doctor of Science – Course of Physic. Area of Nonlinear Dynamics and Complex Systems – Instituto Tecnológico de Aeronáutica, 2024. Advisor: Prof. Dr. Marco Antonio Ridenti. Co-advisor: Prof. Dr. Francisco Javier Azpilicueta.

1. Gravity Waves. 2. Lower Atmosphere. 3. Atmospheric Physics. 4. Ionosphere. 5. Geophysics. 6. Model Linear Generalized. I. Instituto Tecnológico de Aeronáutica. II. Title.

BIBLIOGRAPHIC REFERENCE

DE SOUZA MUNIZ SILVA, Alysson Brhian. **Statistical Study of Gravity Waves in the Lower Atmosphere and Predictive Modeling of Low Latitude Ionospheric Irregularities**. 2024. 142f. Thesis of Doctor of Science – Instituto Tecnológico de Aeronáutica, São José dos Campos.

CESSION OF RIGHTS

AUTHOR'S NAME: Alysson Brhian de Souza Muniz Silva
PUBLICATION TITLE: Statistical Study of Gravity Waves in the Lower Atmosphere and Predictive Modeling of Low Latitude Ionospheric Irregularities.
PUBLICATION KIND/YEAR: Thesis / 2024

gov.br
Documento assinado digitalmente
ALYSSON BRHIAN DE SOUZA MUNIZ SILVA
Data: 18/01/2025 21:13:14-0300
Verifique em https://validar.iti.gov.br

Alysson Brhian de Souza Muniz Silva
Av. Roma, 673, D125
12.216-510 – São José dos Campos–SP

STATISTICAL STUDY OF GRAVITY WAVES IN THE LOWER ATMOSPHERE AND PREDICTIVE MODELING OF LOW LATITUDE IONOSPHERIC IRREGULARITIES

Alysson Brhian de Souza Muniz Silva

Thesis Committee Composition:

Prof. Dr.	Erico Rempel	President	-	ITA
Prof. Dr.	Marco Antonio Ridenti	Advisor	-	ITA
Prof. Dr.	Francisco Javier Azpilicueta	Co-advisor	-	UNLP
Prof^{a}. Dr^{a}.	Marisa Roberto (*in memorian*)	Co-advisor	-	ITA
Prof. Dr.	Rodrigo Sávio Pessoa	Internal Member	-	ITA
Prof. Dr.	Cristiano Max Wrasse	External Member	-	INPE
Prof. Dr.	Igo Paulino da Silva	External Member	-	UFCG

ITA

I dedicate this to **God**, whose love and guidance sustain me daily. To my dear wife **Léia Rocha**, thank you for your constant support and love. And to our wonderful daughter **Júlia Letícia**, you are my greatest joy and inspiration.

Acknowledgments

I thank God—the creator of the sky, earth, sea, and all that they contain—because without Him, I would not have life or a purpose for my existence. I have dedicated my life project to Him, and He has shown compassion by allowing me to study at the Aeronautics Technology Institute (ITA), a place I have always dreamed of attending.

I would like to express my heartfelt gratitude to my wife, Léia Rocha, for always being by my side during my undergraduate studies. She encouraged me to continue my education while also caring for our daughter, Júlia Letícia. I am thankful to my father, Adilson Costa, for his unwavering support during challenging moments. I also want to thank my mother, Sunamita Maria, and my brothers, Adysson Brhiner and Andrew William, for managing our affairs in Manaus. Additionally, I appreciate my parents (Messias Pucu—*in memoriam* and Marluce Rocha) and my sisters-in-law (Shirley, Lucas, Lorena, Sophia, and Rute) for their assistance with other matters in Manaus, Amazonas.

I am deeply grateful to Professor PhD Erico Rempel for introducing me to the institution and motivating me to enroll in the postgraduate physics program. After my enrollment, he recommended that I work with Professor PhD Marisa Roberto (*in memorian*). I sincerely appreciate Professor Roberto for guiding me on my journey to becoming a researcher. Her knowledge shared during classes and meetings, along with her belief in my potential to pursue a PhD without a master's degree, has been invaluable. I also thank PhD Marco Ridenti for his support from the moment I became a PhD student under Professor Roberto's mentorship. He taught me to write and think like a scientist and later assisted me in completing my thesis. Additionally, I would like to acknowledge PhD Elson Campos, PhD Alessandro Abreu, and PhD José Abalde for their significant contributions to my project, their insightful discussions, and their support during my internship at the *Universidad Nacional de La Plata* (UNLP) in Argentina.

I would like to acknowledge my professors and peers from the National Institute for Space Research (INPE) who provided essential knowledge in Space Geophysics for my thesis. During the COVID-19 pandemic, they, along with Sophia Laranja, an ITA student, supported me throughout my journey. Laranja has been with me every step of my PhD studies.

I would also like to express my gratitude to my supervisors, Professor PhD Maurício Gende and Professor PhD Francisco Azpilicueta at UNLP. They not only guided me on the content but also taught me many things beyond Space Geophysics. Together with the professors and students at UNLP, they engaged in discussions on topics relevant to my research.

Last but not least, I express my appreciation for the support provided by the *Instituto Federal de Educação, Ciência e Tecnologia do Amazonas* (IFAM) and the *Fundação de Amparo à Pesquisa do Amazonas* (FAPEAM). Their assistance made it possible for me to receive support during my stay in *São José dos Campos*, São Paulo, Brazil, and *La Plata*, Buenos Aires, Argentina.

“If I have seen further
it is by standing on the shoulders of Giants.”
— Sir Isaac Newton

Resumo

Esta tese apresenta uma análise estatística detalhada das ondas de gravidade (*graviy waves* - GWs) na baixa atmosfera sobre a região brasileira, bem como um modelo preditivo para irregularidades ionosféricas em baixas latitudes. No contexto das GWs, o estudo avalia perfis de vento e temperatura para determinar as densidades de energia cinética e potencial das GWs utilizando um conjunto de dados abrangente de medições de radiossonda realizadas pelo Instituto de Controle do Espaço Aéreo (ICEA). Variações sazonais e espaciais foram examinadas por meio de agrupamento hierárquico, Transformada Rápida de Fourier e análises do Método dos Mínimos Quadrados. Os resultados mostram que as densidades de energia cinética e potencial das GWs apresentam variações sazonais e espaciais. No contexto da ionosfera, um Modelo Linear Generalizado (*Generalized Linear Model* - GLM) foi desenvolvido para prever condições ionosféricas, treinando com dados de Conteúdo Eletrônico Total (*Total Electron Content* - TEC) coletados ao longo de 12 anos na estação de Brasília (15°S, 47°W). O modelo incorpora variáveis independentes como horário, fluxo solar, índice geomagnético e parâmetros de posição solar. O GLM otimizado demonstrou alta precisão na distinção entre estados ionosféricos regulares e irregulares, aprimorando nossa compreensão da variabilidade do TEC e seus fatores influenciadores. O modelo desenvolvido apresentou uma precisão superior a 90% na previsão de irregularidades ionosféricas, superando outros modelos da literatura. Esta investigação dual avança tanto nosso conhecimento sobre as GWs atmosféricas quanto a previsibilidade de irregularidades ionosféricas, oferecendo ideias para aplicações relacionadas ao clima espacial em sistemas de navegação e comunicação.

Abstract

This thesis presents a detailed statistical analysis of gravity waves (GWs) in the lower atmosphere over the Brazilian region, as well as a predictive model for ionospheric irregularities at low latitudes. In the context of the GWs, the study evaluates wind and temperature profiles to determine the kinetic and potential energy densities of GWs using a comprehensive dataset from radiosonde measurements from the Instituto de Controle do Espaço Aéreo (ICEA). Seasonal and spatial variations were investigated using Hierarchical Clustering, Fast Fourier Transform, and Least Squares Method analyses. The results reveal that the kinetic and potential energy densities of GWs exhibit well-defined seasonal and spatial patterns, clustered regionally. In the context of the ionosphere, a Generalized Linear Model (GLM) was developed to predict ionospheric conditions by training on Total Electron Content (TEC) data collected over 12 years in Brasília station (15°S, 47°W). The model includes independent variables such as time, solar flux, geomagnetic index and solar position parameters. The optimized GLM demonstrated high accuracy in discriminating between regular and irregular ionospheric states, improving our understanding of TEC variability and its influencing drivers. The model developed achieved over 90% accuracy in predicting ionospheric irregularities, outperforming existing models in the literature. This dual investigation advances both our knowledge of atmospheric GWs and the predictability of ionospheric irregularities, providing insights for space weather-related applications in navigation and communication systems.

List of Figures

List of Tables

List of Abbreviations and Acronyms

AC	Agglomerative Coefficient
AUC-ROC	Area Under the Receiver Operating Characteristic Curve
ca	cauchit
CIT	Convectively Induced Turbulence
cl	complement log-log
CV	Coefficient of Variation
DoD	US Department of Defense
DOY	Day Of Year
EAS	Elevation Engle of the Sun
EASr	Elevation Angle of the Sun normalized
EIA	Equatorial Ionization Anomaly
EPB	Equatorial Plasma Bubbles
ESF	Equatorial Spread F
fa	fall
FAR	False Alarm Rate
FFT	Fast Fourier Transform
FN	False Negative
FNR	False Negative Rate
FP	False Positive
FPR	False Positive Rate
fw	fall-winter, dry season
GLM	Generalized Linear Model
GLONASS	Global Orbiting Navigation Satellite System
GNSS	Global Navigation Satellite System
GPS	Global Positioning System
GWs	Gravity Waves
IBGE	*Intituto Brasileiro de Geografia e Estatística*
ICEA	*Instituto de Controle do Espaço Aéreo*
In	Inaccuracy

ITU	International Telecommunication Union
ITZC	Intertropical Convergence Zone
IWLS	Iteratively Reweighted Least Squares
lo	logit
LSM	Least Square Method/Linear Squares Method
LSTID	Large Scale TID
Md	Median
MdC	Centered Moving Medians
MSTID	Medium Scale TID
NA	Not Available
OLR	Ordinary Linear Regression
po	probito
PRE	Pre Reversal Enhancement
PSD	Power Spectrum Density
QBO	Quasi-Biennial Oscillation
RBMC	*Rede Brasileira de Monitoramento Contínuo*
RINEX	Receiver INdependent EXchange
ROC	Receiver Operating Characteristic
ROT	Rate Of TEC
ROTI	ROT Index
S	Lower Stratosphere
sfu	solar flux unit
sp	spring
ss	spring-summer, wet season
SSTID	Small Scale TID
su	summer
T	Troposphere
TEC	Total Electronic Content
TECU	TEC Unit
TID	Traveling Ionospheric Disturbance
TLS	Tropospheric and Lower Stratosphere or Time Left to Sunrise
TLSr	Time Left to Sunrise normalized
TN	True Negative
TP	True Positive
TPWID	Traveling Planetary Wave Ionospheric Disturbance
US	United States of America
UTC	Coordinated Universal Time
UV	UltraViolet
VHF	Very High Frequency

VTEC	Vertical TEC
WAM-IPE	Whole Atmosphere Model-Ionosphere Plasmasphere Electrodynamics
WBMOD	Wideband Ionospheric Scintillation Model
wi	winter

List of Symbols

β	fitting coefficient
δ	Sun declination
γ	growth rate of an ionospheric instability or adiabatic index
$\hat{\omega}$	intrinsic frequency of GW
κ	ratio of specific heat at constant pressure to specific heat at constant volume
λ	wavelenght
μ	mean of a Normal probability distribution function
ν_{in}	collision frequency between ions and neutrons
Ω	Earth's rotation rate
ω_p	plasma frequency
ϕ, L	geographic latitude
ρ	density or correlation between a pair of samples
σ	standard deviation of a Normal probability distribution function
θ	potential temperature or scale parameter of a Gamma distribution
B	magnetic field
c	speed of light in vacuum
c_g	group velocity
c_p	specific heat at constant pressure
c_s	speed of sound
E	electric field
E_K	density of kinetic energy
E_P	density of potential energy
F	obliquity factor
f	oscillation frequency, critical frequency or Coriolis parameter
$F_{10.7}$	solar flux
f_0F_2	critical frequency of the F_2 layer
g	acceleration due to gravity
$g(\cdot)$	link function
h	height
H	height scale or duration of day

h_i, h_I	barycenter of the ionosphere or ionospheric piercing point
$h'F_2$	virtual height of the F_2 layer
J	density of current electric
k	zonal wave number or shape parameter of a Gamma distribution
k_H	horizontal wave number
K_p	planetary K index
l	meridional wave number
M	molar mass or size of series/spatial series
m	vertical wave number
N	Brunt-Vaisälä frequency or quantity of the time series (when indicated)
n	sample size, length of a time series, or specific number
n_e	electron density
p	pressure or probability
Q	heating rate
R	ideal gas constant
r_E	radius of the Earth
$sd(\cdot)$	standard deviation
T	temperature
t	time
u	zonal wind
v	meridional wind
V_n	neutral wind speed
w	vertical wind
x	zonal component of distance
X, Y	dissipation forces
X_k, X^I, Y_k	samples
y	meridional component of distance
Y_k	component of FFT
z	height or angle of zenith
z^I	angle between the signal path and a line passing through the Earth's center and the ionospheric piercing point (IPP) h_i

Contents

1 Introduction

The initial objective of this thesis was to develop a model for forecasting ionospheric irregularities through the utilization of gravity waves (GWs) measurements obtained from radiosondes launched at 32 Brazilian aerodromes. These measurements were to be employed as independent variables, while data from Global Navigation Satellite System (GNSS) receivers were to be used to identify the ionospheric irregularities and serve as a dependent variable. An exploratory analysis of GW characteristics revealed that this study constituted a unique and valuable contribution in its own right. Prior to this study, no research had been conducted on this topic utilizing radiosondes to investigate GWs in Brazilian lower atmosphere. Consequently, a comprehensive statistical investigation into GWs in the Brazilian lower atmosphere was undertaken and published (BRHIAN *et al.*, 2024).

Subsequently, the ionospheric irregularities were identified above a Brazilian Global Navigation Satellite System (GNSS) receiver situated in close proximity to the sbbr's aerodrome. The Rate of Total Electron Content (TEC) Index (ROTI) was deemed an appropriate means for identifying the aforementioned ionospheric irregularities. A multiple regression model was selected for predicting the ionospheric irregularities, employing selected variables extracted from the GWs and others. The explanatory variables utilized in the regression model were the density of energy from GWs, the greater wavelength adjusted in the GWs, the day of year (DOY), the $F_{10.7}$ solar cycle index, and the K_p index representing the state of the magnetosphere.

However, preliminary results from a regression model designed to predict ionospheric irregularities indicated that the variables DOY, $F_{10.7}$ and the K_p index were the most significant explanatory variables. In light of this outcome, it was resolved to alter the objectives of this thesis and to construct a model based on Generalized Linear Models (GLMs) with a Bernoulli distribution for the dependent variable. Initially, an additive GLM was employed to predict ionospheric irregularities with all of the most probable explanatory variables and local time. Additionally, all possible combinations of the raw explanatory variables and all possible combinations of some normalized explanatory variables were considered. However, after extensive data analysis, research, and discussions, it was decided to use eight models, in which the K_p variable is treated as binary data with all possible interactions among the variables. This approach yielded valuable insights, and a second article has been written based on these findings (already submitted and awaiting approval).

This thesis represents a synthesis of two distinct works. The first part is a statistical study of GWs, while the second part is the construction of a probabilistic model for predicting ionospheric irregularities. This thesis commences with a concise overview of GWs, their significance, and the primary references that motivated their study in this context. It then delineates the principal contributions of the research. Subsequently, an overview of forecasting models for ionospheric irregularities — an increasingly pivotal topic in Space Weather research — was presented, accompanied by a discussion of how this thesis offers distinctive insights and contributions to the field.

1.1 Gravity Waves

GWs are atmospheric perturbations caused by the restoring force of gravity that propagate adiabatically in the atmosphere (GOSSARD; HOOKE, 1975; HARGREAVES, 1995; NAPPO, 2013; YIGIT; MEDVEDEV, 2015; MOFFAT-GRIFFIN *et al.*, 2020). They are usually formed by natural events or even human activities such as nuclear bomb or mines (AZEEM *et al.*, 2015; FRITTS; ALEXANDER, 2003; GOSSARD; HOOKE, 1975; HEALE *et al.*, 2020; HUANG *et al.*, 2019; OLIVEIRA *et al.*, 2016; YIGIT, 2015). When GWs are generated in the lower atmosphere they could produces plasma bubbles (KHERANI *et al.*, 2009) and traveling ionospheric disturbances (TID) (YIGIT, 2015).

GWs in the troposphere and lower stratosphere (TLS) have been historically studied by using microbarometers, kites, aircraft, radars, sodars, lidars and satellites (NAPPO, 2013). In this work, GWs were identified using measurements from meteorological balloons (radiosondes), using the same approach used by (YOSHIKI; SATO, 2000). Other similar GW's studies using radiosondes were carried out in other geographic locations: (ZINK; VINCENT, 2001), in Macquarie Island, Australia; (ZHANG; YI, 2005), in Wuhan, China and (OLIVEIRA *et al.*, 2016), in Rio Grande do Norte, Brazil. This thesis analyzed radiosonde measurements carried out in 2014 at 32 aerodromes throughout Brazil by the *Instituto de Controle do Espaço Aéreo* (ICEA) and they were launched daily at 00:00 and 12:00 UTC with the primary objective of providing data on the lower atmosphere for research, weather forecasting, and aviation purposes (BRASIL, 2013; BRASIL, 2017; WORLD METEROLOGICAL ORGANIZATION, 2018). The time averages were computed for two different samples; the first covered the dry season – fall (fa) and winter (wi) – and the other the wet season – spring (sp) and summer (su). As far as we are aware, this is the first work that investigates GWs systematically using radiosonde measurements from a broad net of stations (or aerodromes) maintained by ICEA and distributed throughout the Brazilian territory.

Studies show that GWs generated in the troposphere and lower stratosphere are capable of transmitting energy to the base of the ionosphere, playing a key role in the "seeding" of plasma bubbles and ionospheric disturbances (VADAS *et al.*, 2003; YIGIT, 2015; AYORINDE *et al.*, 2024). As these waves reach higher altitudes, they can trigger initial instabilities that evolve into plasma bubbles due to Rayleigh-Taylor instability. Theoretical and observational models, such as those presented by Heale et al. (2020), support this connection. Furthermore, the spectral characteristics of GWs, such as intrinsic frequency and vertical wavelengths, are critical factors for the efficiency of this coupling process.

We computed the averages of the wind profiles and performed a cluster analysis on them to identify regions where the prevailing winds have similar behavior. This analysis showed that regions having similar latitudes tend to cluster, that is, the wind profiles in each cluster have on average almost the same shape during the same period (wet or dry). Besides, signal processing techniques such as the Fast Fourier Transform (FFT) and the Least Squares Method (LSM), were used to extract quantitative information related to the GWs like amplitude, wavelength, phase shift and energy density from the measured profiles. The magnitude of the variability of the velocity components was quantified by integrating the power spectrum density (PSD), yielding an estimate of the kinetic energy densities of the GWs. The potential energy of the GWs was estimated in a similar fashion using the temperature profiles. Furthermore, it was also investigated the spatio-temporal correlation between the energies measured at different aerodromes. Finally, we identified the quasi-monochromatic GWs in the TLS and compared them with other similar results reported in the literature (VINCENT; ALEXANDER, 2000; ZHANG; YI, 2005; GELLER; GONG, 2010; GONG; GELLER, 2010). By using radiosonde data from several stations over a one-year period, we were able to access the characteristics of GWs covering a vast area under the Brazilian territory and investigate its seasonal and spatial variations. The technique applied in this work allowed to analyze GWs in a spectral range not accessible by satellites or other methods (ALEXANDER, 1998; ALEXANDER *et al.*, 2010; MOFFAT-GRIFFIN *et al.*, 2020). In the end, it was identified and studied quasi-monochromatic GWs in the TLS, finding good agreement between our results and the results reported in the literature (VINCENT; ALEXANDER, 2000; ZHANG; YI, 2005; GELLER; GONG, 2010; GONG; GELLER, 2010).

One more key motivation for studying GWs is their impact on climate modeling. In the stratosphere and mesosphere, where GW amplitudes increase and wave breaking occurs, climate models must account for these waves (ALEXANDER *et al.*, 2010). To accurately model the effects of GWs, it is essential to understand their sources and spectral distribution. Given the broad spectral range of GWs and the variety of their sources, progress in this field requires a cumulative approach, integrating studies from different locations, periods, and measurement techniques.

1.2 Ionosphere

Ionospheric irregularities at low latitudes are known to be the cause of many failures in positioning and communication systems, like degradation of radio propagation, radar clutter and strong radio wave scintillation (SAHAI *et al.*, 2000; MENDILLO *et al.*, 2000; ABDU *et al.*, 2003; SEEBER, 2003; REZENDE *et al.*, 2010; DAS *et al.*, 2010; SEEMALA; VALLADARES, 2011; CHERNIAK *et al.*, 2014; CHIAN *et al.*, 2018; KLIPP *et al.*, 2019; ATABATI *et al.*, 2021; GONZáLEZ, 2022; WOOD *et al.*, 2024). Many observational and theoretical studies have been carried out over the years to advance the understanding of the physical processes that lead to such irregularities, their effects on electromagnetic wave propagation and their phenomenology and climatology (KELLEY, 2008). It is now recognized that such irregularities are caused by Rayleigh-Taylor-type plasma instabilities, which give rise to plasma density depletions that form at the base of the ionosphere, growing over time and moving upward (FARLEY *et al.*, 1970; KELLEY, 2008). Due to their characteristics, these irregularities are referred to as Equatorial Plasma Bubbles (EPBs). Previous studies have demonstrated that EPBs occur mostly at night, move eastward and extend along the Earth's magnetic field lines (KELLEY, 2008).

The accumulated knowledge on this topic, combined with new analytical and computational tools, has enabled many researchers to focus their efforts on forecasting ionospheric events that could potentially disrupt or damage communication and positioning systems. (ABREU *et al.*, 2010; REZENDE *et al.*, 2010; HUBA, 2021; ATABATI *et al.*, 2021; CHERNIAK *et al.*, 2014; GONCHARENKO *et al.*, 2021). Despite many advances in the science of low-latitudes ionosphere, the current ability to predict such irregularities is still limited (MAKELA; MILLER, 2011; CHERNIAK *et al.*, 2014; KIL, 2015). For instance, the unpredictable nature of such irregularities has prevented the certification of navigation systems such as Satellite-Based Augmentation Systems (SBAS) and Ground-Based Augmentation Systems (GBAS) in countries located at low latitudes. Such events may eventually cause loss of lock on GNSS (Global Navigation Satellite Systems) or total loss of signal (DATTA-BARUA *et al.*, 2021), making it impossible to certify GBAS on aerodromes located at low latitudes until safe mitigating solutions or forecasting products are available.

Identified and described for the first time in the 1930s (BERKNER; WELLS, 1934), low latitude ionospheric irregularities have since then been studied using different observational techniques on the ground such as ionosondes, radars, imagers and GNSS receivers (ABDU *et al.*, 2003; MAKELA; OTSUKA, 2012; TSUNODA, 2021; CARMO *et al.*, 2022). Measurements in the space environment, made possible by satellites and rockets, have also been used to study this phenomenon (SCHUNK; NAGY, 2009; KELLEY, 2008). Examples of these are electrostatic probes (LARANJA *et al.*, 2023), magnetometers (STOLLE *et al.*, 2006), photometers (KARAN *et al.*, 2020) and retarding potential analyzers (SU *et al.*, 2001). The extensive observational data obtained through this wide range of techniques has shown that EPBs depend on various factors, such as local time, season, latitude, neutral winds, the intensity of the $E \times B$ drift, the alignment between the terminator and magnetic longitude, solar activity and the solar cycle (ABDU *et al.*, 1992; HARGREAVES, 1995; MENDILLO *et al.*, 2000; ABDU *et al.*, 2003; DABAS *et al.*, 2003; HOFMANN-WELLENHOF *et al.*, 2008; DAS *et al.*, 2010; MAKELA; OTSUKA, 2012; SOUZA *et al.*, 2012; PEREIRA; CAMARGO, 2013; SUBIRANA *et al.*, 2013; CHERNIAK *et al.*, 2014; MACHADO; AGUIAR, 2016; LI *et al.*, 2020; ABDU, 2020; ATABATI *et al.*, 2021; CARMO *et al.*, 2022; WOOD *et al.*, 2024). Besides, geomagnetic conditions (ABREU *et al.*, 2010; CARMO *et al.*, 2022; GONZáLEZ, 2022; ABREU *et al.*, 2023; AA *et al.*, 2024), planetary waves, GWs or TID (FAGUNDES *et al.*, 2009b; FAGUNDES *et al.*, 2009a; AMORIM *et al.*, 2011; SEEMALA; VALLADARES, 2011; GONCHARENKO *et al.*, 2021; GONZáLEZ, 2022; WOOD *et al.*, 2024), natural hazards (ASTAFYEVA, 2019) and human activities (HUANG *et al.*, 2019) can have an influence on this irregularities.

Given the wide range of factors influencing ionospheric irregularities, there has been considerable effort to develop forecasting models using various data inputs. Several studies have applied different modeling techniques to predict ionospheric conditions. For example, Atabati et al. (2021) employed a neural network and genetic algorithm to design a solar-quiet model using variables such as solar flux, F_2 layer height, and sunspot numbers. Similarly, Abdu et al. (2003) used cubic-B splines to model the occurrence of spread-F based on ionosonde data from Fortaleza and Cachoeira Paulista. Other studies, such as those by Rezende et al. (2010) and Das et al. (2010), applied machine learning techniques like bootstrap aggregation and neural networks to predict ionospheric scintillation, using input variables such as vertical drift velocity, solar flux, and S_4. Meanwhile, Souza et al. (2012) developed the Parameterized Regional Ionosphere Model (PARIM), which modeled the F_2 critical frequency without considering geomagnetically perturbed periods. More recent approaches, such as the work by Hysell et al. (2022), have proposed physically-based models, incorporating regional ionospheric irregularity dynamics. Despite some challenges in model accuracy, these studies contribute valuable insights into ionospheric behavior. Additionally, the semi-empirical WBMOD model (SECAN *et al.*, 1995) has been widely used for ionospheric scintillation prediction. However, many models still fail to account for geomagnetic disturbances, which are important for improving the accuracy of ionospheric forecasts, especially during periods of heightened geomagnetic activity. In order to establish a good forecast strategy, it was necessary to identify measurable quantities or known variables that strongly correlate to such irregularities to serve as explanatory variables. Based on the current konwledge about the causes of EPBs, as discussed previously, four explanatory variables (or independent variables) were selected: time left to sunrise, maximum elevation angle of the Sun, $F_{10.7}$ and K_p. This selection accounts for the well-known variations associated with daily, seasonal, solar and magnetospheric state forcing factors, while also being readily accessible on demand.

This study aims to fit the independent variables to forecast whether the ionosphere is regular or irregular. For this purpose, a methodology superior to the Ordinary Linear Model (OLM), known as GLMs, was employed. This type of model can handle many non-Gaussian distributed response variables (JOSHI *et al.*, 2024; WOOD *et al.*, 2024), including binary responses. Additionally, their coefficients provide significant insights into the independent variables that compose the model. Since this quantity is derived from GNSS receiver data, it is particularly suitable for forecasting models due to its availability, good temporal resolution and low missing data ratio (CHERNIAK *et al.*, 2014; HARSHA *et al.*, 2020; CARMO *et al.*, 2022). With the independent variables, the GLM models estimate the probability of such occurrences after being trained – or calibrated, using the more precise terminology. Numerical and statistical tests were conducted to identify the optimal models, considering forecast sensitivity, specificity, Area Under the ROC Curve (AUC-ROC) and parsimony as selection criteria. Parsimony guides researchers in selecting models with fewer variables when multiple models perform similarly, as models with the same performance but fewer variables tend to avoid overfitting and facilitate interpretation (HAIR *et al.*, 2006).

In this study, the models were trained, calibrated and tested using a set of ROTI values extracted from GPS receivers located at *braz* (15°46′48″S, 47°55′45″W), covering the time span from 2010 to 2022. This site was chosen because it is situated beneath the region influenced by the Appleton Anomaly, which occurs in the ionosphere between magnetic latitudes ±15° and ±30° (SEEBER, 2003; REZENDE *et al.*, 2010; KELLEY, 2008; PEREIRA; CAMARGO, 2013; KLIPP *et al.*, 2019; AOL *et al.*, 2020; MARUYAMA, 2020; GONZáLEZ, 2022; WOOD *et al.*, 2024). In this region, ionospheric irregularities are expected to exhibit greater density variations, which can potencially produce stronger scintillation and deleterius effects on GNSS systems (BALAN *et al.*, 1997; MENDILLO *et al.*, 2000). Seemala and Valladares (2011) demonstrated that this area experiences the highest occurrences of plasma depletion during December (KLIPP *et al.*, 2019; AOL *et al.*, 2020).

1.3 Organization of Thesis

This thesis was organized into two main parts: each chapter has the first part focusing on GWs in the Brazilian lower atmosphere during 2014, and the other one on forecasting ionospheric irregularities at a Brazilian station from 2010 to 2022. For this reason, it is recommended that the reader first focus on one part of the thesis, such as the section on gravity waves, and then proceed to the other part, which discusses ionospheric irregularities.

The chapter titled *Theoretical Foundation* started discussing the neutral atmosphere, the GWs including their definition, characteristics, and role in seeding ionospheric irregularities. It also addresses the ionosphere and the physics of ionospheric irregularities and it presents the development of a forecasting model for the state of the ionosphere. In the following chapter, *Methodology*, statistical techniques for extracting and characterizing GWs from radiosonde data are outlined. This chapter also details the identification of ionospheric irregularities, the forecasting model employed, and the statistical methods used to select the best model. The chapter *Results and Discussions* presents statistical analyses of GWs alongside the forecasting model for ionospheric irregularities and examines the alignment of the obtained results with those published in the specialized literature. Finally, key findings are highlighted in the *Conclusion* chapter.

2 Theoretical foundation

2.1 Gravity Waves

2.1.1 The Earth's Neutral Atmosphere

The Earth's atmosphere is typically classified into many layers based on physical properties such as temperature, chemical composition, and plasma density (AHRENS; HENSON, 2018) – where this last one is discussed in section 2.2.1. The chemical composition of the atmosphere can be divided into two main regions. The lower layer, known as the homosphere, maintains a nearly constant proportion of its constituents due to turbulent mixing. Above this, the heterosphere forms, where lighter molecules are separated from heavier ones, with each molecule having a distinct vertical scale height, denoted by H (RISHBETH; GARRIOT, 1969; AHRENS; HENSON, 2018).

The Earth's atmosphere is traditionally divided into four layers based on temperature gradients (KATO, 1980; KIRCHHOFF, 1991; AHRENS; HENSON, 2018):

- **Troposphere**: The layer closest to the Earth's surface extends from the ground up to approximately 15 km at the equator (about 10 km near the poles). This layer contains most of the atmosphere's mass and is where most meteorological phenomena occur. The temperature decreases with altitude in this region due to the adiabatic expansion of convective air.

- **Stratosphere**: Extending from 15 to 50 km in altitude, this layer contains the ozone layer (O_3), which absorbs ultraviolet (UV) radiation from the Sun. The temperature increases with altitude in this layer, primarily due to the absorption of UV radiation by ozone (O_3), water vapor (H_2O) and carbon dioxide (CO_2).

- **Mesosphere**: Located from approximately 50 to 90 km, the temperature decreases with altitude in this layer. The temperature is governed by a balance between the radiative heating of molecular oxygen (O_2) and the radiative cooling of carbon dioxide (CO_2).

- **Thermosphere**: In this layer, temperature increases with altitude due to the absorption of solar radiation. This leads to the dissociation of molecular oxygen (O_2) and the ionization of atomic oxygen (O). The temperature continues to rise until it reaches the maximum known as the exospheric temperature.

An alternative classification of the atmosphere based on temperature divides it into three regions: the lower atmosphere (from the surface to 20 km), the middle atmosphere (from 20 to 80 km), and the upper atmosphere (above 80 km) (NAPPO, 2013).

2.1.2 Definition and Features of GWs

GWs are atmospheric disturbances generated by the balance between gravity and buoyancy forces, which propagate adiabatically, analogous to waves on the surface of water (HINES, 1972; GOSSARD; HOOKE, 1975; GILL, 1982; LANDAU; LIFSHITZ, 1987; SALBY, 2012; NAPPO, 2013; YIGIT; MEDVEDEV, 2015). Though first identified in the 19th century, GWs began to be extensively studied in the 1960s using meteor trail observations. These trails initially had a straight shape but were quickly distorted due to winds in the region of formation. By normalizing the wind profile with respect to wind shear and density variations, it was interpreted as a wave train propagating upward, subject to dissipation during propagation. Furthermore, the theoretical prediction was confirmed that the amplitude of GWs increases exponentially due to the exponential decrease in atmospheric density. (HINES, 1960; HINES, 1972).

Historically, GWs in the TLS have been observed using various instruments, such as microbarometers, kites, aircraft, radars, sodars, lidars, and satellites (HINES, 1972; NAPPO, 2013). This study identifies GWs using radiosondes (meteorological balloons), a method also employed by Yoshiki e Sato (2000) to study GWs at the Earth's poles. Radiosondes have been utilized in other similar studies at various locations, including Macquarie Island, Australia (ZINK; VINCENT, 2001); Wuhan, China (ZHANG; YI, 2005); Rothera, Antarctic Peninsula (MOFFAT-GRIFFIN *et al.*, 2011); and Rio Grande do Norte, Brazil (OLIVEIRA *et al.*, 2016). Radiosondes typically reach altitudes of approximately 30 km (ALLEN; VINCENT, 1995; FRITTS; ALEXANDER, 2003; MOFFAT-GRIFFIN *et al.*, 2011; BRASIL, 2020), measuring profiles of wind, temperature, and other meteorological variables along their ascent (WORLD METEROLOGICAL ORGANIZATION, 2018). These measurements provide quantitative data on GWs (ALLEN; VINCENT, 1995; ALEXANDER *et al.*, 2010; NAPPO, 2013), and can be used to estimate the kinetic and potential energy densities of GWs (GELLER; GONG, 2010). In the TLS, the average vertical wavelength of GWs is approximately 5.5 km in the troposphere and 3.5 km in the lower stratosphere (ZHANG; YI, 2005). Additionally, the occurrence of GWs in the troposphere exhibits seasonal variation, while in the lower stratosphere, it is modulated by the quasi-biennial oscillation

(QBO) (ZHANG *et al.*, 2012; HEALE *et al.*, 2020).

GWs are typically generated by various natural phenomena, including topographic sources, tropospheric convection, jet streams, shear instability, geostrophic adjustment, frontal systems, earthquakes, volcanic eruptions, auroral heating, eclipse cooling, turbulence, and wave interactions. Human activities, such as nuclear explosions and mining, can also generate GWs (HINES, 1972; GOSSARD; HOOKE, 1975; FRITTS; ALEXANDER, 2003; FAGUNDES *et al.*, 2008; ALEXANDER *et al.*, 2010; PAULINO *et al.*, 2011; NAPPO, 2013; AZEEM *et al.*, 2015; YIGIT, 2015; OLIVEIRA *et al.*, 2016; HUANG *et al.*, 2019; GIONGO *et al.*, 2020; HEALE *et al.*, 2020). GWs that originate in the lower atmosphere can break and generate new waves at higher altitudes, as demonstrated by Vadas *et al.* (2003), cited by Yigit (2015), simulated by Heale et al. (2020), and observed in radio occultation by Ayorinde *et al.* (2023, 2024). GWs can also arise in regions experiencing convectively induced turbulence (CIT), typically due to cloud convective activity. These regions are of particular importance for aeronautics, as they are difficult to detect and predict. Furthermore, such turbulence can occur even at significant distances from the storm cloud formation areas. Studying GWs in the lower atmosphere is essential for aviation, given that aircraft routinely traverse altitudes of 9 - 13 km (SHARMAN; TRIER, 2018). In higher altitudes, GWs can break in the middle and upper atmosphere (VADAS *et al.*, 2003; NAPPO, 2013; GIONGO *et al.*, 2020; HEALE *et al.*, 2020), generating new GWs through nonlinear wave interactions (SHARMAN; TRIER, 2018; CHIAN *et al.*, 2018). Additionally, GWs can interact with tidal or planetary waves, damping specific modes and altering their oscillation structures (FORBES; GARRET, 1979; FORBES, 1979; HEALE *et al.*, 2020).

When the atmospheric flow is both inertially and gravitationally stable, displaced air parcels resist rotation and buoyancy, leading to oscillations known as *inertial gravity waves*. Low-frequency GWs, or inertia-gravity waves, are those for which the movement of Earth's rotation has an important influence (FRITTS; ALEXANDER, 2003). In mid-latitude tropospheric regions, these oscillations have frequencies in the range $f \leq |\hat{\omega}| \leq N$, with periods ranging from 12 minutes to 15 hours - where f is the Coriolis frequency and N is a Brunt-Väisälä frequency, where they will be defined in Subsection 2.1.3. This range justifies the inclusion of the Coriolis force in the governing equations (HINES, 1960; HOLTON, 2004; ALEXANDER *et al.*, 2010; FAGUNDES *et al.*, 2009b; FAGUNDES *et al.*, 2009a; SALBY, 2012; NAPPO, 2013; YIGIT; MEDVEDEV, 2015).

GWs that propagate in a stratified atmosphere are referred to as internal waves, because they travel vertically within a "wave envelope", depositing energy and momentum in the upper atmosphere where the wave eventually breaks or dissipates. This deposition contributes to mass mixing and temperature changes in the global circulation. On the one hand, the highest energy and momentum deposition in the middle atmosphere occurs in the equatorial regions, followed by the mid-latitudes (HINES, 1960; HINES, 1972; LANDAU;

LIFSHITZ, 1987; NAPPO, 2013; GIONGO *et al.*, 2020; HEALE *et al.*, 2020). On the other hand, when geomagnetic storms enhance particle precipitation at high latitudes through atmospheric Joule heating, GWs are generated and propagate toward the equator over a period of approximately 8 to 12 hours. This occurs within the layers of the middle and upper atmosphere (FAGUNDES *et al.*, 2008).

2.1.3 Equations that Describe the GWs

Due to the broad spectrum of GWs in the lower atmosphere, models based on monochromatic GWs are inadequate for capturing their full behavior, but monochromatic GWs give pieces of evidence about general behaviors. To make this simplification more general, the full spectra of intrinsic frequencies $\hat{\omega}$ should be considered, such that $f \leq |\hat{\omega}| \leq N$, where f represents the Coriolis frequency (to be defined later) (NAPPO, 2013). GWs exhibit time scales ranging from a few minutes to several hours, and their horizontal wavelengths vary from 100 m to 1,000 km (MOFFAT-GRIFFIN *et al.*, 2011; MOFFAT-GRIFFIN *et al.*, 2020).

GWs are typically described by linear theory applied to the conservation equations for mass, momentum, and energy in a stratified, stable and inviscid atmosphere, where macroscopic quantities (e.g., density, pressure, and temperature) vary with altitude. Given that particle collisions occur on much smaller spatial and temporal scales compared to macroscopic quantities, fluid dynamics is a suitable approximation for atmospheric behavior (KATO, 1980). Under these assumptions, molecular motion can be neglected, and the atmosphere is treated as a continuous medium, with small volumes relative to the total volume, but still containing a large number of molecules (HOLTON, 2004).

A coordinate system chosen to solve this equations is the Cartesian plane xy that tangentially touches the Earth's surface, known as the β-plane (HOLTON, 1975; VOLLAND, 1988; SALBY, 2012; HOLTON, 2004). Thus in this coordinate system, x represents the zonal component (positive eastward), y represents the meridional component (positive northward), and z is the vertical direction (positive upward) (STULL, 1988; HERRERA; MORETT, 2016). With this reference frame - and using the same reasoning as in the equations from the work of Fritts and Alexander (2003) - the conservation equations that model GWs are:

$$\frac{du}{dt} - fv + \frac{1}{\rho}\frac{\partial p}{\partial x} = X, \tag{2.1}$$

$$\frac{dv}{dt} + fu + \frac{1}{\rho}\frac{\partial p}{\partial y} = Y, \tag{2.2}$$

$$\frac{dw}{dt} + \frac{1}{\rho}\frac{\partial p}{\partial z} + g = 0, \tag{2.3}$$

$$\frac{1}{\rho}\frac{d\rho}{dt} + \frac{\partial u}{\partial x} + \frac{\partial v}{\partial y} + \frac{\partial w}{\partial z} = 0, \tag{2.4}$$

$$\frac{d\theta}{dt} = Q, \tag{2.5}$$

where $\frac{d}{dt}$ represents the total derivative (or convective derivative); (u, v, w) is the fluid velocity vector; X and Y are generalized forces (such as viscosity force or hydrodynamic force); Q is the heating rate; p is the pressure; ρ is the density such that $\rho = \rho_0 \exp\left(-\frac{z - z_0}{H}\right)$, where $\rho_0 = \rho(z_0)$ and $H < 8$ km (HOLTON, 2004), representing the scale height (which in the lower atmosphere can be considered approximately constant due to mixing effects generated by turbulence in the homosphere, increasing to 6.5 km in the stratosphere (ALEXANDER *et al.*, 2010)); $f = 2\Omega \sin \phi$ is the Coriolis parameter, where $\Omega = 7.292 \cdot 10^{-5}$ rad/s is the Earth's rotation rate and ϕ is the latitude (KATO, 1980; HOLTON, 2004; GELLER; GONG, 2010; NAPPO, 2013; SHARMAN; TRIER, 2018). In addition to these equations, the definition of potential temperature θ is included, which is the temperature a parcel of air would have if brought adiabatically from p to p_0:

$$\theta = \frac{p}{\rho R}\left(\frac{p_0}{p}\right)^{\kappa}. \tag{2.6}$$

This potential temperature equation completes the set of equations describing atmospheric motion. Equation (2.6) typically assumes $p_0 = p(z_0) = 1,000$ hPa, $R = 287$ J/(kg·K) as the ideal gas constant (HOLTON, 2004), and $\kappa = \frac{c_p}{c_v}$ as the ratio of specific heats at constant pressure and volume.

Therefore, the nonlinear equations (2.1)-(2.6) can be linearized, as the oscillations are small compared to the mean terms (FRITTS, 1984; FRITTS; ALEXANDER, 2003; HOLTON, 2004; SALBY, 2012), through the following decompositions:

$$(u, v, w) = (\overline{u(z)}, \overline{v(z)}, 0) + (u'(t), v'(t), w'(t)) \tag{2.7}$$

$$\theta = \overline{\theta(z)} + \theta'(z, t) \tag{2.8}$$

$$p = \overline{p(z)} + p'(z, t) \tag{2.9}$$

$$\rho = \overline{\rho(z)} + \rho'(z, t) \tag{2.10}$$

where the overbar denotes the mean value of the quantities and the prime symbol $'$ represents a harmonic perturbation whose expression will be defined in equation (2.20). If the atmosphere is at rest, then p' and ρ' will have zero value (HOLTON, 2004).

Therefore, the equations (2.1)-(2.6), without dissipative or external forces, are linearized over a horizontally hydrostatically balanced atmosphere. The atmosphere below 100 km can be considered inviscid, as momentum transfer primarily occurs through turbulent motion (HOLTON, 2004; HEALE *et al.*, 2020). Using the aforementioned decompositions and retaining only first-order terms (FRITTS; ALEXANDER, 2003):

$$\frac{Du'}{Dt} + w'\frac{\partial \overline{u}}{\partial z} - fv' + \frac{\partial}{\partial x}\left(\frac{p'}{\overline{\rho}}\right) = 0, \tag{2.11}$$

$$\frac{Dv'}{Dt} + w'\frac{\partial \overline{v}}{\partial z} + fu' + \frac{\partial}{\partial y}\left(\frac{p'}{\overline{\rho}}\right) = 0, \tag{2.12}$$

$$\frac{Dw'}{Dt} + \frac{\partial}{\partial z}\left(\frac{p'}{\overline{\rho}}\right) - \frac{1}{H}\left(\frac{p'}{\overline{\rho}}\right) + g\left[\frac{\rho'}{\overline{\rho}}\right] = 0, \tag{2.13}$$

$$\frac{D}{Dt}\left(\frac{\theta'}{\overline{\theta}}\right) + w'\frac{N^2}{g} = 0, \tag{2.14}$$

$$\frac{D}{Dt}\left[\frac{\rho'}{\overline{\rho}}\right] + \frac{\partial u'}{\partial x} + \frac{\partial v'}{\partial y} + \frac{\partial w'}{\partial z} - \frac{w'}{H} = 0, \tag{2.15}$$

$$\frac{\theta'}{\overline{\theta}} = \frac{1}{c_s^2}\left(\frac{p'}{\overline{\rho}}\right) - \left[\frac{\rho'}{\overline{\rho}}\right]. \tag{2.16}$$

The term $N = \sqrt{g\left(\frac{\partial \ln \theta}{\partial z}\right)}$ represents the Brunt-Väisälä frequency (or buoyancy frequency), where the speed of sound is defined by $c_s^2 = \kappa\frac{p}{\rho}$ (NAPPO, 2013). The derivative operator $\frac{D}{Dt}$ denotes differentiation following fluid motion (KATO, 1980) and is defined as follows:

$$\frac{D}{Dt} = \frac{\partial}{\partial t} + \overline{u}\frac{\partial}{\partial x} + \overline{v}\frac{\partial}{\partial y}. \tag{2.17}$$

The value of the Brunt-Väisälä frequency $\frac{N}{2\pi}$ is approximately of the order of 2.9 mHz in the lower atmosphere (HUANG *et al.*, 2019).

If we substitute the definition of potential temperature (2.6) into the definition of the Brunt-Väisälä frequency N, then:

$$N^2 = g\left(\frac{1}{T}\frac{\partial T}{\partial z} - \frac{R}{c_p P}\frac{\partial P}{\partial z}\right). \tag{2.18}$$

Using the thermodynamic state relations, the hydrostatic pressure equation, the ideal gas law for dry air, and an isothermal atmosphere, it is possible to show that:

$$N^2 = g^2\frac{\gamma - 1}{\gamma}\frac{M_{ar}}{RT} \tag{2.19}$$

where $\gamma = \frac{c_p}{c_v}$ is the adiabatic index.

Progressive waves can be characterized by their amplitudes and phases (HOLTON, 2004). Thus, if we neglect the shear terms in equations (2.11) and (2.12) in the velocity term product, assume $(\overline{u}, \overline{v})$ and N varying very slowly over a wave cycle vertically, and consider the existence of a plane wave for the following perturbations (expressed in complex Fourier form (HINES, 1960)), then (FRITTS, 1984; FRITTS; ALEXANDER, 2003; GELLER; GONG, 2010):

$$\left(u', v', w', \frac{\theta'}{\overline{\theta}}, \frac{p'}{\overline{p}}, \frac{\rho'}{\overline{\rho}}\right) = \left(\tilde{u}, \tilde{v}, \tilde{w}, \tilde{\theta}, \tilde{p}, \tilde{\rho}\right) \exp\left[i(\mathbf{k}\cdot\mathbf{r} - \omega t) + \frac{z}{2H}\right] \tag{2.20}$$

where $\mathbf{k} = (k_H, m) = (k, l, m)$ is the wave number vector, k_H is the horizontal wave number, $\mathbf{r} = (x, y, z)$, ω is the relative (Eulerian) frequency, and the term $\exp\left(\frac{z}{2H}\right)$ is necessary to compensate for the density decrease with height and ensure energy conservation with increasing oscillation amplitudes (HINES, 1960; HINES, 1972). Generally, a two-dimensional plane wave solution of the form $e^{i(k_x x + k_z z - \omega t)}$ is sufficient (HARGREAVES, 1995).

As gravity waves propagate upwards, they increase in amplitude proportional to $\exp\left(z\frac{\gamma g}{2c_s^2}\right)$. This can be understood in terms of energy flux, as the atmosphere decreases in proportion to $\exp\left(-z\frac{\gamma g}{2c_s^2}\right)$. However, this amplitude increase competes with damping effects due to energy dissipation such as molecular viscosity and thermal conductivity (HINES, 1960; SALBY, 2012; HUANG *et al.*, 2019; HEALE *et al.*, 2020) occurring in the middle and upper atmosphere (HINES, 1972; FORBES; GARRET, 1979; FORBES, 1979; AYORINDE *et al.*, 2023; AYORINDE *et al.*, 2024). With these considerations, equations (2.11)-(2.16) transform into the following algebraic equations (GOSSARD; HOOKE, 1975; FRITTS; ALEXANDER, 2003):

$$-i\hat{\omega}\tilde{u} - f\tilde{v} + ik\tilde{p} = 0 \tag{2.21}$$

$$-i\hat{\omega}\tilde{v} - f\tilde{u} + il\tilde{p} = 0 \tag{2.22}$$

$$-i\hat{\omega}\tilde{w} + \left(im - \frac{1}{2H}\right)\tilde{p} = -g\tilde{\rho} \tag{2.23}$$

$$-i\hat{\omega}\tilde{\theta} + \left(\frac{N^2}{g}\right)\tilde{w} = 0 \tag{2.24}$$

$$-i\hat{\omega}\tilde{\rho} + ik\tilde{u} + il\tilde{v} + \left(im - \frac{1}{2H}\right)\tilde{w} = 0 \tag{2.25}$$

$$\tilde{\theta} = \frac{\tilde{p}}{c_s^2} - \tilde{\rho} \tag{2.26}$$

and the term $\hat{\omega} = \omega - (k\overline{u} + l\overline{v})$ represents the intrinsic frequency, i.e., the frequency of the wave in the reference frame of the fluid motion - the second and third terms denote the Doppler shift. The negative sign indicates westward phase propagation relative to the mean wind (GOSSARD; HOOKE, 1975; HOLTON, 2004; SALBY, 2012).

Equations (2.21)-(2.26) can be solved to find the wave dispersion relation, provided that the determinant of the coefficients equals zero:

$$\underbrace{\begin{vmatrix} -i\hat{\omega} & -f & 0 & ik & 0 & 0 \\ f & -i\hat{\omega} & 0 & il & 0 & 0 \\ 0 & 0 & -i\hat{\omega} & \left(im - \frac{1}{2H}\right) & g & 0 \\ 0 & 0 & \frac{N^2}{g} & 0 & 0 & -i\hat{\omega} \\ ik & il & \left(im - \frac{1}{2H}\right) & 0 & -i\hat{\omega} & 0 \\ 0 & 0 & 0 & -\frac{1}{c_s^2} & 1 & 1 \end{vmatrix}}_{(\tilde{u},\tilde{v},\tilde{w},\tilde{p},\tilde{\rho},\tilde{\theta})} = 0.$$

The imaginary part of the determinant yields the relationship:

$$\frac{g}{c_s^2} = \frac{1}{H}. \tag{2.27}$$

Substituting the above result into the real part of the determinant, it is possible to show that the dispersion relation of a gravity-acoustic wave can be written as:

$$\hat{\omega}^2 \left[k^2 + l^2 + m^2 + \frac{1}{4H^2} - \frac{(\hat{\omega}^2 - f^2)}{c_s^2}\right] = N^2(k^2 + l^2) + f^2 \left(m^2 + \frac{1}{4H^2}\right). \tag{2.28}$$

The equation (2.28) relates both acoustic and gravity waves. Therefore, under the Boussinesq approximation, where an incompressible atmosphere is considered ($c_s \to \infty$) to eliminate sound waves (HOLTON, 2004), the dispersion relation of a gravity wave can be written as (FRITTS; ALEXANDER, 2003; ALEXANDER *et al.*, 2010; NAPPO, 2013; YIGIT, 2015):

$$\hat{\omega}^2 = \frac{N^2(k^2 + l^2) + f^2 \left(m^2 + \frac{1}{4H^2}\right)}{k^2 + l^2 + m^2 + \frac{1}{4H^2}} \tag{2.29}$$

or alternatively through the vertical wave number:

$$m^2 = \frac{k_H^2(N^2 - \hat{\omega}^2)}{\hat{\omega}^2 - f^2} - \frac{1}{4H^2} = \frac{(k^2 + l^2)(N^2 - \hat{\omega}^2)}{\hat{\omega}^2 - f^2} - \frac{1}{4H^2}, \tag{2.30}$$

where internal GWs propagating vertically have real wave numbers in all directions and are constrained by $f \leq |\hat{\omega}| \leq N$. Altitudes where $\hat{\omega} \to 0$ are referred to as *critical levels.* GWs near and below these critical levels often become unstable and dissipate, a process known as *critical level filtering.* The horizontal wavelength $\lambda_H = \frac{2\pi}{k_H}$ can range from a few kilometers to thousands of kilometers, while λ_z theoretically ranges from 0 to ∞, making it impossible for a single instrument to cover all these length scales (HINES, 1972; ALEXANDER *et al.*, 2010; GIONGO *et al.*, 2020). Therefore, knowing that $H \to \infty$ and $N >> \hat{\omega}$, the equation (2.29) simplifies for mid-latitude regions to:

$$m^2 = k_H^2 \frac{N^2}{\hat{\omega}^2 - f^2}. \tag{2.31}$$

In the case where $m \to 0$, the wave may be reflected. Above this reflection point, the wave becomes *evanescent* and decays exponentially. However, if a GW enters in a region between two reflection points, the wave will be ducted between them as if entering a duct. Waves with $\lambda_H > 10$ km are generally considered significant in the middle atmosphere, since that small horizontal wavelengths are easier to be reflected and trapped at lower altitudes (HINES, 1972; FRITTS; ALEXANDER, 2003; HEALE *et al.*, 2020; AYORINDE *et al.*, 2023). In a more comprehensive theory considering an atmosphere with thermal gradients, phenomena such as reflection and ducting must be taken into account in GW propagation. Reflections and refractions of GWs occur in regions with density gradients, temperature gradients, or wind shear over a wide range of altitudes, complicating the prediction of GW propagation (HINES, 1972; HUANG *et al.*, 2019; NGUYEN *et al.*, 2022).

The quantity describing energy transport and wave packet propagation is the group velocity, defined as the derivative of the angular frequency of the wave with respect to the wave number (SALBY, 2012; NAPPO, 2013):

$$c_{gx} = \frac{\partial \omega}{\partial k} = \overline{u} + \frac{k(N^2 - \hat{\omega}^2)}{\hat{\omega}\left(k^2 + l^2 + m^2 + \dfrac{1}{4H^2}\right)} \tag{2.32}$$

$$c_{gy} = \frac{\partial \omega}{\partial l} = \overline{v} + \frac{l(N^2 - \hat{\omega}^2)}{\hat{\omega}\left(k^2 + l^2 + m^2 + \dfrac{1}{4H^2}\right)} \tag{2.33}$$

$$c_{gz} = \frac{\partial \omega}{\partial m} = \frac{-m(N^2 - \hat{\omega}^2)}{\hat{\omega}\left(k^2 + l^2 + m^2 + \dfrac{1}{4H^2}\right)}. \tag{2.34}$$

The value of the vertical wave propagation parameter m is negative for group velocity directed upwards, indicating that the wave energy will propagate upwards if the wave phase propagates downwards (HINES, 1960; HOLTON, 2004).

In the lower atmosphere, the velocity perturbation in the direction perpendicular to the direction of propagation is no longer zero. This perturbation grows in magnitude as the intrinsic frequency decreases toward the Coriolis frequency $\hat{\omega} \sim f$ (FRITTS; ALEXANDER, 2003). In general, the magnitude of the vertical wavenumber $|m|$ is much greater than the magnitude of the horizontal wavenumber $|k_H|$, as shown by the dispersion relation in Equation (2.29). Substituting into Equations (2.32) - (2.34):

$$c_g \sim \left(\frac{k_H(N^2 - f^2)}{f^2\left(k_H^2 + m^2 + \dfrac{1}{4H^2}\right)}, 0 \right), \tag{2.35}$$

where $\overrightarrow{c_g} \propto \overrightarrow{k_H}$, meaning that GWs propagate mainly horizontally (HUANG *et al.*, 2019).

The amplitudes of Equations (2.21)-(2.26) can be combined to generate various relationships between the perturbations of the quantities, known as polarization relations. Combining Equations (2.21) and (2.22), we obtain the following equation that allows us to determine the intrinsic frequency of any type of GWs (GOSSARD; HOOKE, 1975; FRITTS; ALEXANDER, 2003):

$$\tilde{u} = \frac{i\hat{\omega}k - fl}{i\hat{\omega}l + fk}\tilde{v}. \tag{2.36}$$

At low altitudes, the most important disturbances are those of low frequency, because the internal waves are influenced by the Earth's rotation. They have a helical characteristic and can propagate both upward and downward. In the southern hemisphere, for example, a wind profile rotating counterclockwise indicates that GWs are propagating upward (ALLEN; VINCENT, 1995; ZHANG; YI, 2005). Furthermore, many experiments demonstrate invariance in the vertical wavenumber and frequency spectra of waves, even with decreasing density with altitude (ALLEN; VINCENT, 1995).

For a zonally propagating from inertia-gravity waves, where $l \to 0$, the amplitude of the meridional velocity derived from (2.36) is calculated as:

$$\tilde{v} = -i\frac{f}{\hat{\omega}}\tilde{u}. \tag{2.37}$$

At latitudes near the equator where $f \sim 0$ the polarization relationship (2.36) and the dispersion relation of equation (2.29), become:

$$\tilde{u} = \frac{k}{l}\tilde{v} \tag{2.38}$$

$$m^2 = k_H^2\frac{N^2}{\hat{\omega}^2}. \tag{2.39}$$

A way to obtain the intrinsic frequency $\hat{\omega}$ experimentally is by fitting an ellipse on the hodograph, provided that the ratio of the major axis to the minor axis is exactly $\frac{\hat{\omega}}{f}$ (TSUDA *et al.*, 1990; VINCENT *et al.*, 1997; VINCENT; ALEXANDER, 2000), for latitudes not near the equator.

Suppose a quasi-monochromatic wave of a GW has a horizontal velocity such that its velocity components are phase-shifted by $\Delta\phi$ which can be modeled as:

$$(u, v) = (a \sin(\hat{\omega} t), b \sin(\hat{\omega} t + \Delta\phi)) \, . \tag{2.40}$$

Similarly, where a and b are the amplitudes of the GW with $a > b$, the magnitude of this velocity can be written as:

$$u^2 = \sin^2(\hat{\omega} t)^2 (a^2 + b^2 \cos^2 \Delta\phi) + \cos^2(\hat{\omega} t)(b^2 \sin^2 \Delta\phi) + 2 \sin(\hat{\omega} t) \cos(\hat{\omega} t)(b^2 \sin \Delta\phi \cos \Delta\phi) \tag{2.41}$$

.

Similarly, the critical points of the velocity magnitude occur when $\hat{\omega} t = n\pi$ or $\hat{\omega} t = n\frac{\pi}{2}$, such as $n \in \mathbb{Z}$. Thus, the critical points for the smallest and largest values of the magnitude will be respectively:

$$u_{\parallel}^2 = b^2 \sin^2 \Delta\phi \tag{2.42}$$

$$u_{\perp}^2 = a^2 + b^2 \sin^2 \Delta\phi \tag{2.43}$$

.

Therefore, the ratio between the maximum and minimum magnitude of the velocity will be:

$$\frac{u_{\perp}}{u_{\parallel}} = \sqrt{\frac{a^2 + b^2 \sin^2 \Delta\phi}{b^2 \cos^2 \Delta\phi}} \tag{2.44}$$

.

For the case where $\Delta\phi = 90°$, the equation (2.44) becomes similar to the magnitude of equation (2.37). This allows us to estimate $\frac{f}{\hat{\omega}}$ as the ratio between the major axis and the minor axis of an ellipse derived from a hodograph that may contain a quasi-monochromatic GW.

2.2 Ionosphere

2.2.1 The Earth's Ionosphere

The ionosphere is an ionized layer of the Earth's atmosphere, subdivided according to its electron density, composition, and electrodynamic environment. It is typically divided into five distinct layers (RISHBETH; GARRIOT, 1969; KATO, 1980; KIRCHHOFF, 1991; BATISTA *et al.*, 2003; RICHARDS, 2008; KELLEY, 2008; SCHUNK; NAGY, 2009):

- D **layer**: The lowest daytime ionospheric region, located approximately between 50 and 80 km in altitude. It is primarily influenced by soft X-rays and Lyman-α radiation. In this region, the electron density is not high enough to significantly affect radio wave propagation, but it serves as a signal attenuator.
- E **layer**: An ionospheric layer found approximately between 80 and 130 km in altitude. It has the highest electrical conductivity (Hall and Pedersen) and is the layer where electrical currents develop. During the daytime, it maintains a nearly constant height. In winter, its electron density decreases due to lower solar radiation. Ionization in this region is caused by extreme ultraviolet (EUV) and ultraviolet (UV) solar radiation.
- F_1 **layer**: A daytime region located between 130 and 200 km, with a peak electron concentration around 200 km. In this layer, ionization losses transition from being quadratic to linear, according to Chapman's theory of ionospheric layers (KIRCHHOFF, 1991). The characteristics of the F_1 layer are strongly correlated with sunspot numbers (SEEBER, 2003). Ionization in this region is similar to that in the E layer.
- F_2 **layer**: The highest and most ionized region of the ionosphere, extending from 200 to 400 km in altitude. Its peak electron concentration occurs during the summer. The F_2 layer is primarily ionized by solar soft X-rays.
- F_3 **layer**: This layer appears in the equatorial region during the daytime when a specific interaction between the winds and Appleton's diffusion elevates the plasma above the F_2 layer (BALAN *et al.*, 1997; BATISTA *et al.*, 2003).

Generally, the F_1 and F_2 layers are present during the daytime and are strongly influenced by the geomagnetic field, because at these altitudes, the atmosphere is nearly rarefied and the plasma moves almost freely along the geomagnetic field lines. Additionally, during nighttime, when solar radiation is absent, ions recombine rapidly, causing the E and F_2 layers to become more prominent (RICHARDS, 2008; EMMERT J.AND RICHMOND; DROB, 2010).

2.2.2 Phenomena in the Ionosphere

Appleton discovered the Earth's ionized layer in 1924 (KATO, 1980), now known as the ionosphere. This layer forms when radiation from the Sun and outer space interacts with neutral atmospheric gases, ionizing them and creating plasma. The resulting ionization is significant enough to influence radio wave propagation (RISHBETH; GARRIOT, 1969; FAGUNDES *et al.*, 2008; MUKHERJEE *et al.*, 2010; CHERNIAK *et al.*, 2014; AHRENS; HENSON, 2018; PIMENTA, 2020). Radio waves, particularly those with frequencies between 500 kHz and 30 MHz, travel over long distances through the ionosphere, which acts as a mirror or pipeline for AM radio broadcasts, auxiliary aviation navigation and amateur shortwave communication (RICHARDS, 2008).

But this transmission became affected when ionospheric scintillations appear. The ionospheric scintillations are caused by plasma degradation and refer to rapid fluctuations in the amplitude and phase of GNSS radio signals, occurring over timescales of seconds as the signals pass through the ionosphere (SAHAI *et al.*, 2000; SEEBER, 2003; CHERNIAK *et al.*, 2014; CHIAN *et al.*, 2018; AOL *et al.*, 2020; NGUYEN *et al.*, 2022). These ionospheric scintillations are strongly seasonal and influenced by various factors, including solar activity, time of year, local time, geographic location, and the frequency of the transmitted signal. Scintillations are most commonly observed in regions near between 20°S and 20°N of the magnetic latitude, as well as in the auroral and polar regions (CHERNIAK *et al.*, 2014). So, understanding these irregularities is essential for Space Weather research besides other areas (KIL, 2015; MAKELA; MILLER, 2011).

Various types of irregularities occur in the ionospheric region, and the terminology used to describe them depends on the detection instruments employed. For example, in the equatorial F layer, the phenomenon known as *equatorial spread F* (ESF) has been studied since 1930, involving irregularities detected by ionosondes. Satellites *in situ* measurements registered similar irregularities, often manifested as electrons density depletions relative to the background ionosphere. These are referred to as *depletions*, *bite-outs*, or *plasma holes*. In contrast, terms like *plumes* and *wings* describe turbulent morphologies observed via radar. The term *bubble* is used to describe plasma irregularities associated with ESF. Observations suggest that these plasma bubbles have a shell-like shape (PI *et al.*, 1997; MA; MARUYAMA, 2006; FAGUNDES *et al.*, 2009a; AMORIM *et al.*, 2012; KIL, 2015; AOL *et al.*, 2020; LI *et al.*, 2020).

An important phenomenon in the ionosphere is the dynamo effect, which occurs when winds cause ions to move along geomagnetic field lines, generating an electric field (RISHBETH; GARRIOT, 1969). This movement creates a current density $\mathbf{J}$, where the scalar product $\mathbf{J} \cdot \mathbf{E}$ is negative, and the electric forces act in the opposite direction to the charge separation source (KELLEY, 2008). The dynamo effect plays a crucial role in understanding plasma behavior in the F layer, particularly the pre-reversal enhancement (PRE), where plasma rises during twilight in regions near the magnetic equator (Figure 2.1) (MAKELA; MILLER, 2011).

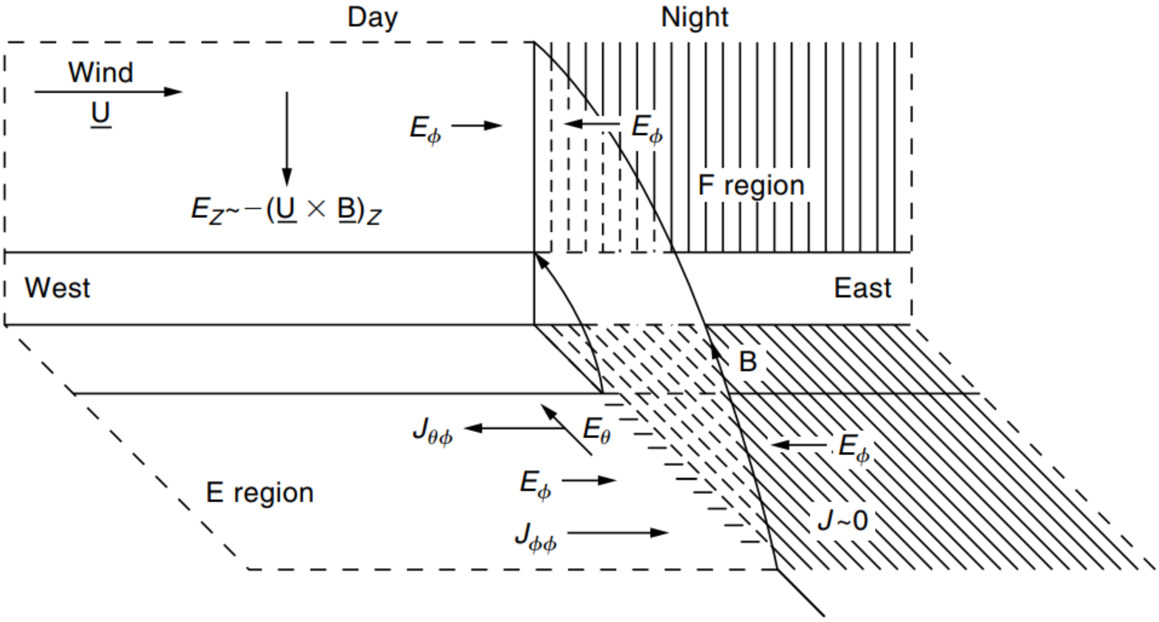

FIGURE 2.1 – Simplified model of the F layer pre-reversal peak resulting from a uniform thermospheric wind **U** (KELLEY, 2008).

The PRE occurs during sunset, near the terminator, in the sunlit region, as a result of the lifting of plasma from the lower ionospheric layers. In the daytime side, near the magnetic equator, a zonal thermospheric wind, denoted by **U**, directed eastward, is observed in the F layer. Depending on the alignment between the terminator and the magnetic field (ABDU, 2020; LI *et al.*, 2020), a vertical current, $\mathbf{U} \times \mathbf{B}$, is generated. During the equinoxes, the conductivity in the E region decreases more rapidly, and the alignment of the solar terminator with the magnetic meridian promotes a more significant vertical plasma displacement, which fosters the formation of plasma bubbles (LI *et al.*, 2020).

Because the circuit formed by the E and F layers is not closed due to rapid recombination in the lower layers, a downward polarization electric field $\mathbf{E}_z$ is induced. This field is mapped along magnetic field lines to the E layer, generating an electric field $\mathbf{E}_\theta$ directed toward the equator. This electric field drives a westward Hall current, $\mathbf{J}_{\theta\phi}$. However, because the conductivity on the nighttime side is very low, the current is restricted to the daytime side. As a result, negative polarization charges accumulate at the terminator. Consequently, polarization fields, $\mathbf{E}_\phi$, form on both sides of the terminator, and a Pedersen current, $\mathbf{J}_{\phi\phi}$, cancels the Hall current.

The electric field directed toward the terminator is then mapped to the F layer along the magnetic field lines, driving a drift that causes the plasma to rise on the daytime side and fall on the nighttime side (KELLEY, 2008; FAGUNDES *et al.*, 2009a). The amplitude and duration of the electric field that drives this drift depend on various factors, including: the intensity and direction of the winds in the F region; changes in conductivity in the E and F regions; the behavior of the E layer dynamo; asymmetry between the two hemispheres; and other factors such as seasonality, geomagnetic activity, and solar activity. Magnetic storms can also alter the direction of the electric field, reversing it from east to west and inhibiting the lifting of plasma (FAGUNDES *et al.*, 2008).

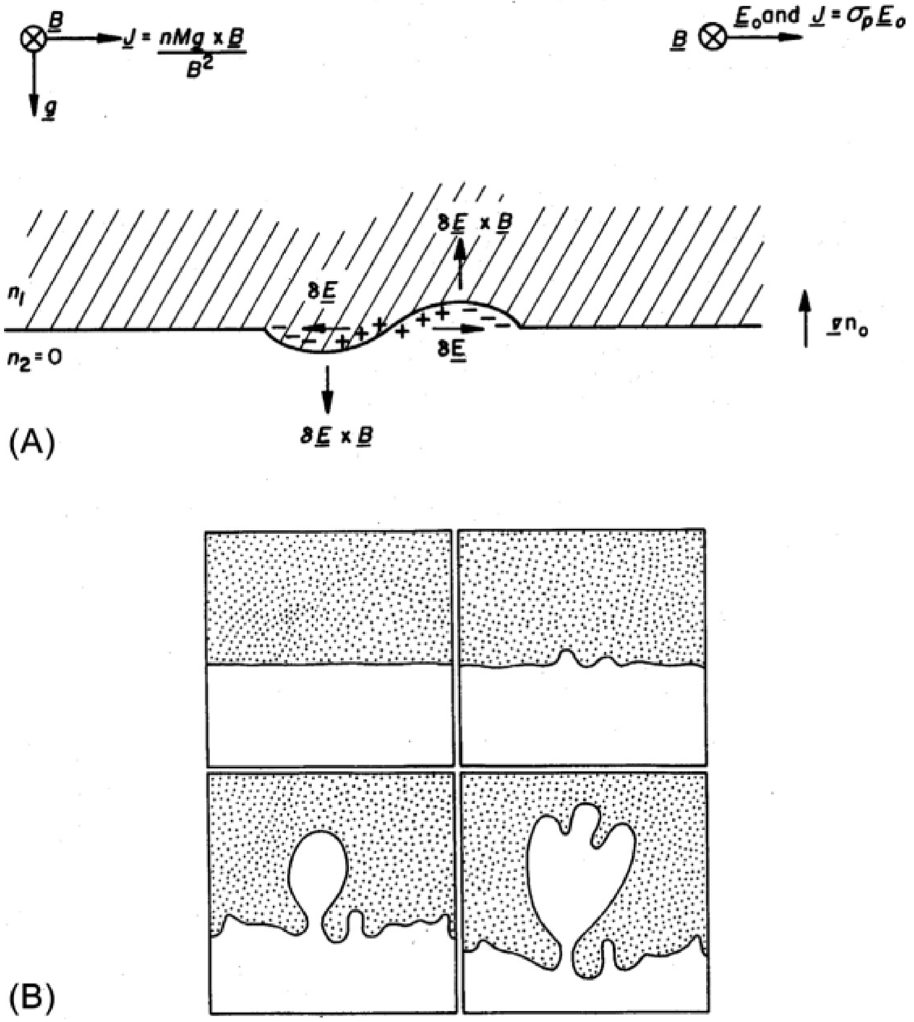

FIGURE 2.2 – Illustration of instability growth in the F layer: (A) Schematic diagram of plasma analogies to Rayleigh-Taylor instabilities in an equatorial geometry and (B) images showing the growth of Rayleigh-Taylor instabilities in a denser fluid over a less dense fluid (KELLEY, 2008).

The PRE phenomenon explains the significant increase in plasma velocity during twilight, followed by a reversal of direction in the early hours of the night. As plasma is lifted, a region of low plasma density forms, creating a vertical density gradient that points upward. Consequently, a denser region above a less dense one becomes unstable. Small instabilities in the lower layers, potentially triggered by gravity waves and the PRE, can cause low-density plasma to move into the high-density region, resembling a bubble rising in water.

The PRE lifts plasma near the magnetic equator, but due to low radiation, diffusion, and gravity, this plasma descends along geomagnetic field lines to latitudes near ±20°, forming a region known as the Equatorial Ionization Anomaly (EIA), or Appleton's anomaly (PI *et al.*, 1997; KELLEY, 2008; MUKHERJEE *et al.*, 2010; FAGUNDES *et al.*, 2009a; MAKELA; MILLER, 2011; ABDU, 2020; AOL *et al.*, 2020; LI *et al.*, 2020; NGUYEN *et al.*, 2022). Significant PRE values are associated with peaks in EIA concentration. However, if the PRE does not develop sufficiently, ionospheric irregularities may remain confined to the magnetic equator. This attenuation of PRE may be influenced by the westward electric field generated by the Prompt Penetration Electric Field (PPEF) during magnetically disturbed periods (SAHAI *et al.*, 2000; FAGUNDES *et al.*, 2008; FAGUNDES *et al.*, 2009b). Additionally, phenomena such as planetary waves and geomagnetic storms can modulate and control the PRE (SAHAI *et al.*, 2000; FAGUNDES *et al.*, 2009b; FAGUNDES *et al.*, 2009a).

The formation of these plasma bubbles has been theoretically explained by the Rayleigh-Taylor instability, a mechanism first proposed by Dungey (DUNGEY, 1956). In the presence of a disturbance, where the ionization density gradient points upward, gravity force induces a westward ion current. This ion current generates an electric polarization field $\delta\mathbf{E}$, as shown in Figure 2.2A. When $\delta\mathbf{E}$ is oriented eastward, it produces a vertical drift $\delta\mathbf{E} \times \mathbf{B}$ of ions and electrons, causing the low-density region to rise into the denser plasma region, akin to the behavior of a bubble, as depicted in Figure 2.2B. As the plasma in the reduced-density region increases, the relative density reduction intensifies, leading to a stronger eastward electric polarization field. This further accelerates the upward movement of the rarefied plasma, amplifying the electric polarization field and the associated vertical drift. This feedback mechanism leads to the nonlinear growth of the instability and the formation of degraded plasma regions, aligned with the magnetic field, commonly referred to as plasma bubbles.

From the electron continuity, ion and electron momentum, and current equations, the local growth rate of the Rayleigh-Taylor instability can be derived and defined as (MA; MARUYAMA, 2006; MAKELA; MILLER, 2011; ABDU, 2020; AOL *et al.*, 2020; HUBA, 2021):

$$\gamma = \frac{1}{n_0}\frac{\partial n_0}{\partial x}\left(\frac{g}{\nu_{in}} + V_n - \frac{cE_0}{B_0}\right) \tag{2.45}$$

where n_0 is the electron density, g is the gravitational acceleration, ν_{in} is the ion-neutral collision frequency, E_0 is the electric field, B_0 is the Earth's magnetic field, V_n is the neutral wind velocity, and c is the speed of light in vacuum.

Equatorial Plasma Bubbles (EPBs) are disturbances in the ionosphere that primarily occur at low latitudes. These bubbles are associated with various atmospheric and ionospheric phenomena, including gravity waves, planetary waves, tidal waves, PRE, and Travelling Ionospheric Disturbances (TIDs) resulting from geomagnetic storms, or a combination of these factors (MA; MARUYAMA, 2006; FAGUNDES *et al.*, 2009b; FAGUNDES *et al.*, 2009a; AMORIM *et al.*, 2011). Also, geomagnetic storms can influence EPB formation for up to 2 to 4 days (FAGUNDES *et al.*, 2009b), altering ion concentration in the ionosphere. The ion concentration can either increase (positive phase) or decrease (negative phase) compared with non-disturbed days (quiet time, $K_p < 2$) (PIMENTA *et al.*, 2008; FAGUNDES *et al.*, 2008; ABREU *et al.*, 2023). These bubbles typically have horizontal dimensions on the order of thousands of kilometers, with longitudinal width extending from meters to several hundred kilometers. They reach altitudes between 1,500 and 2,500 km and generally move eastward (SAHAI *et al.*, 2000; CHIAN *et al.*, 2018).

These EPBs are typically observable during the night (CHIAN *et al.*, 2018) and into the early morning hours (MAKELA; MILLER, 2011), representing the largest source of ionospheric irregularities during these periods. As solar radiation completes the flux tubes (i.e., geomagnetic field lines) at dawn, EPBs decrease in scale and eventually dissipate (LI *et al.*, 2020). Also, EPBs exhibit self-organizing behaviors such as bifurcation, merging, splitting, and reconnection, which are nonlinear processes that can lead to further instabilities and generate turbulent structures in the ionosphere (CHIAN *et al.*, 2018).

EPBs also exhibit seasonal variations that depend on factors such as the solar cycle, local time, latitude, and time of year (LI *et al.*, 2020). In the Northern Hemisphere, EPBs are more frequent during the summer season. During periods of low solar activity, EPBs tend to develop later in the evening due to reduced instability rates in the lower F layer and weaker vertical background winds (ABDU *et al.*, 2003; MAKELA; MILLER, 2011). In Brazil, EPBs are less frequent from May to August and more frequent from October to March (ABDU *et al.*, 2003; SEEMALA; VALLADARES, 2011). A marked shift in EPB activity is observed between August and October, during the transition from the winter to the spring season. This transition is likely driven by a significant increase in thermospheric wind intensity.

During periods of high solar activity, the occurrence of plasma bubbles increases from 19:30 to 21:00 LT. Also, in this period the electron densities and the O_2^+ are larger than during low solar activity period due of the higher solar flux. In contrast, during periods of low solar activity, plasma bubble growth is slower, peaking around 22:00 LT (SAHAI *et al.*, 2000; FAGUNDES *et al.*, 2009b; FAGUNDES *et al.*, 2009a). When an EPB occurs between 18:00 and 21:00 LT, it is considered “fresh”, indicating it has developed locally. If it appears later, it is referred to as “fossil”, suggesting it originated at a significant distance (FAGUNDES *et al.*, 2009b; FAGUNDES *et al.*, 2009a).

The most prominent characteristics of EPBs, such as occurrence rate, duration, and depth, are typically observed during equinoxes, summer, and periods of high solar activity (SAHAI *et al.*, 2000; LI *et al.*, 2020). A study conducted in the Northern Hemisphere, specifically in Hong Kong, with data from 9 GNSS stations over the period 2013–2019, found that the occurrence rate, depth, and duration of ionospheric irregularities peaked during equinox months and reached minima during the winter. These values were also dependent on solar activity. Additionally, two asymmetries were identified: the solstitial asymmetry, where irregularities were more frequent in summer than winter, and the equinoctial asymmetry, with irregularities occurring more frequently in spring than in autumn (PEREIRA; CAMARGO, 2013; LI *et al.*, 2020).

At mid and high latitudes, the Total Electron Content (TEC) – where in summary the TEC represent a quantity of electrons between one receptor and one satellite (see section 2.2.4) – can sometimes be higher in the winter than in the summer, particularly during the day. This phenomenon is attributed to the increase in the ratio of atomic oxygen [O] to molecular nitrogen [N_2], caused by the convection of atomic oxygen from the summer hemisphere to the winter hemisphere (MUKHERJEE *et al.*, 2010; YASYUKEVICH *et al.*, 2018; AZPILICUETA; NAVA, 2021).

Various instruments can be used to detect ionospheric irregularities, such as those that measure TEC in the ionosphere. EPBs can cause large gradients and irregularities in TEC, leading to scattering and diffraction of radio waves, which in turn results in rapid fluctuations (or scintillations) in the amplitude and phase of the received signals (MUKHERJEE *et al.*, 2010; CHERNIAK *et al.*, 2015; AOL *et al.*, 2020; LI *et al.*, 2020). TEC measurements are typically obtained from signals transmitted by a network of GNSS (Global Navigation Satellite System) satellites and collected by ground-based stations (MUKHERJEE *et al.*, 2010; ABDU, 2020). For this reason, TEC was used in this work to identify when there was a irregular ionosphere.

2.2.3 Gravitational Waves as a Seeding Mechanism for the Ionospheric Irregularities

In 1957, a study was published analyzing the coupling between the troposphere and ionosphere through the examination of cold fronts using the parameters from the F_2 layer as the virtual altitude ($h'F_2$) and the ordinary frequency (f_0F_2) (BAUER, 1957). This study concluded that there was a strong correlation between the passage of cold fronts and the characteristics of the F_2 layer. However, three years later, Hines's seminal paper (1960) proposed that TIDs are caused by GWs originating from the troposphere (HINES, 1972; AMORIM *et al.*, 2012). In 1962, Gossard observed that GWs have periods ranging from 10 minutes to 2 hours (NAPPO, 2013). In the late 1960s and early 1970s, satellites observed instances of plasma depletion at night in the upper F layer (KIL, 2015). At this time, it was already hypothesized that a GWs reaching high altitudes could lead to atmospheric heating comparable to that caused by solar radiation. This heating would alter the local dynamics and disturb the ionospheric distribution, ultimately influencing global communication that depends on radio wave propagation (HINES, 1972).

Subsequent studies on the saturation, dissipation, and momentum deposition of GWs demonstrated their significant role in transporting energy and momentum from the lower to the upper atmosphere (TSUDA *et al.*, 1990; AMORIM *et al.*, 2011; HEALE *et al.*, 2020). Additional works revealed the coupling between the neutral atmosphere and ions, leading to diffusion effects, energy dissipation, anisotropy in TID generation, and heating due to GW damping (HUANG *et al.*, 2019; HARGREAVES, 1995). Thus, GWs and plasma instabilities are present in the thermosphere due to heating processes, contributing to the emergence of various scales of ionospheric irregularities. These processes intensify significantly during geomagnetic storms and have a profound effect on the propagation of transionospheric radio signals (PI *et al.*, 1997).

In 2015, a study for the first time visually confirmed the generation of concentric GWs in the troposphere, which subsequently reached the ionosphere. This observation was made using multiple instruments (AZEEM *et al.*, 2015). Previous experimental studies, such as those conducted during the Spread F Experiment (SpreadFEx) campaign in 2005 (PAULINO *et al.*, 2011), had already demonstrated that GWs generated in the lower atmosphere can trigger irregularities in the upper atmosphere (KHERANI *et al.*, 2009).

However, the propagation and dissipation of GWs depend on thermodynamic conditions and the characteristics of the waves, such as phase velocity, period, and wavelength. Three key conditions are necessary for GWs to generate plasma bubbles in the ionosphere (PAULINO *et al.*, 2011):

1. GWs must penetrate into the lower part of the F layer;
2. The amplitude of the wave must be large enough to modify the thermodynamic properties of the local atmosphere;
3. The phase velocity of the wave must be such that it generates resonance between the wave and the formation of the plasma bubble.

Despite these findings, there is still a lack of experimental work that definitively demonstrates the presence of the seed for plasma bubble formation in the ionosphere prior to the formation of the plasma bubble itself. Additionally, more experiments are needed to establish a clear link between the triggering of plasma bubble formation and GWs in the lower atmosphere (TAORI *et al.*, 2011).

2.2.4 The Total Electronic Content

As previously mentioned, the ionosphere is divided into regions with distinct characteristics, such as peaks in electron density. These electron densities vary seasonally, influenced by factors such as the time of day, time of year, latitude and solar activity. The electron density is directly related to the critical frequency, which is the frequency at which radio waves of a given frequency and angle of incidence are reflected back to the ground. The study of this phenomenon began with the advent of radio transmission in the early 20th century, when the anomalies in radio wave propagation were first observed (KIL, 2015).

The ionized region, with electron density n_e (electrons/m^3), has a refractive index n given by (SEEBER, 2003; RICHARDS, 2008):

$$n = \sqrt{1 - \frac{\omega_p^2}{\omega^2}} \tag{2.46}$$

$$\omega_p^2 = \frac{n_e e^2}{m\varepsilon}, \tag{2.47}$$

where ω_p is the plasma frequency, e is the electron charge, m is the electron mass, ε is the vacuum permittivity, and ω is the angular frequency of the incident radio wave.

The ionosphere can be considered a dispersive medium because the speed of electromagnetic waves within it depends on the frequency of the waves. In this medium, electrons cause a delay in the group velocity and an advance in the phase velocity. Higher frequencies, however, are less affected by the ionosphere. This is particularly evident for electromagnetic waves in the microwave range, spanning from 10^7 to 10^{10} Hz (SEEBER, 2003; LI *et al.*, 2020). The irregularities, when appears in an ionosphere, are responsible for scintillation and are characterized by spatial gradients, whose typical scale is much larger than the wavelength of the incident waves in this frequency range (PI *et al.*, 1997).

An incident ray directed toward the ionosphere undergoes refraction in the upper layers due to the variation in electron density, until it reaches a refractive index n_k, where the radio wave propagates perpendicular to the vertical and begins to travel toward the Earth, as illustrated in Figure 2.3. We can use Snell's Law to express the condition for refraction at the ionospheric boundary:

$$\sin i = n_k \tag{2.48}$$

where i is the angle of incidence and n_k is the refractive index at the point where the ray from the electromagnetic wavefront starts to return to the Earth's surface.

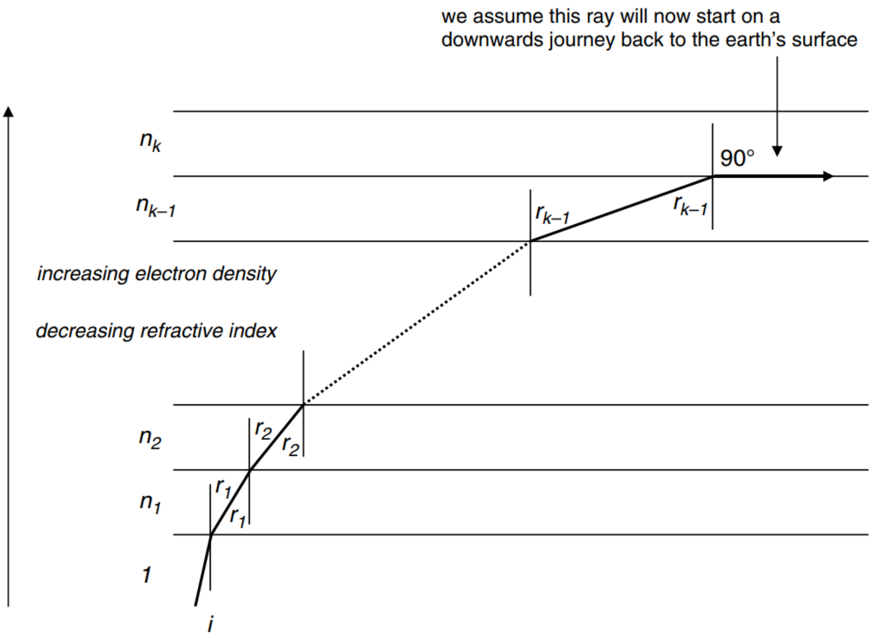

FIGURE 2.3 – The refraction of a radio wavefront in an ionospheric layer occurs when the wavefront begins to return to the Earth's surface. This happens when the angle of refraction, r_k, and the normal to the surface are both 90° (RICHARDS, 2008). Here, r_k represents the angle of refraction in the ionospheric layer k.

If we combine (2.46) and (2.48), it is possible to determine the density of the ionosphere where reflection occurs. This happens specifically when $i = 0°$ relative to the horizontal (RICHARDS, 2008):

$$f_0 = \frac{\omega_p}{2\pi} \approx 9\sqrt{n_{e,max}}, \tag{2.49}$$

where f_0 is the *critical frequency* (Hz) of the wave and $n_{e,max}$ is the electron density (electrons/m^3) at the layer with the maximum density. If the frequency of a wave exceeds f_0, the wave will escape the ionosphere and will not return to Earth. This equation is important because it relates the frequency of an electromagnetic wave to the point in the ionosphere where the wave will be reflected to the Earth.

By measuring the time interval Δt between the emission and return of a radio wave at a specific frequency, and assuming the propagation path is a vacuum, we can determine the *virtual height* Δh of the electron density, given by $\Delta h = c\Delta t$. This quantity is termed "virtual" because the path between the Earth's surface and the peak electron density in the ionosphere do not have refractive index constant along the path (RICHARDS, 2008).

The errors associated with the ionospheric path are proportional to TEC, which is defined as (SEEBER, 2003; HOFMANN-WELLENHOF *et al.*, 2008; MUKHERJEE *et al.*, 2010;

PEREIRA; CAMARGO, 2013; CHERNIAK *et al.*, 2015; NGUYEN *et al.*, 2022):

$$TEC = \int_S^R n_e(s)\, ds, \tag{2.50}$$

where the integral is taken over the signal path s between the satellite S and the receiver R, with n_e representing the electron density along the path. In other words, TEC represents the total number of electrons contained in a column from the receiver to the satellite, with a base area of 1 m^2 (PEREIRA; CAMARGO, 2013). The unit of TEC (TECU) is 10^{16} electrons/m^2 (PI *et al.*, 1997; SEEBER, 2003; HOFMANN-WELLENHOF *et al.*, 2008; RICHARDS, 2008; NGUYEN *et al.*, 2022). TIDs propagating through the ionosphere can be detected via TEC signatures reveling not only natural but also artificial phenomena that had occurred in the lower atmosphere (HUANG *et al.*, 2019).

To compare TEC values across stations, the vertical projection of TEC, known as VTEC, is used. VTEC is defined as (SEEBER, 2003; HOFMANN-WELLENHOF *et al.*, 2008):

$$VTEC = TEC \cos z^I = TEC \frac{1}{F}, \tag{2.51}$$

where F is the obliquity factor, and z^I is the angle between the signal path and the line passing through the Earth's center to the *ionospheric piercing point* (IPP) at altitude h_i, as shown in Figure (2.4). Some studies suggest that the IPP is located approximately 350 km above the Earth's surface (RICHARDS, 2008; CHERNIAK *et al.*, 2014; HARSHA *et al.*, 2020).

The highest VTEC values are typically observed between 12:00 and 15:00 LT, regardless of the season. Moreover, higher VTEC values are recorded during the equinoxes compared to the summer months due to changes in neutral gas composition. In winter, the atmosphere tends to be more mixed, with descending atmospheric fluids, while in summer, these fluids rise. During winter, the greatest standard deviations (i.e., volatility) in VTEC occur between noon and sunset (MUKHERJEE *et al.*, 2010).

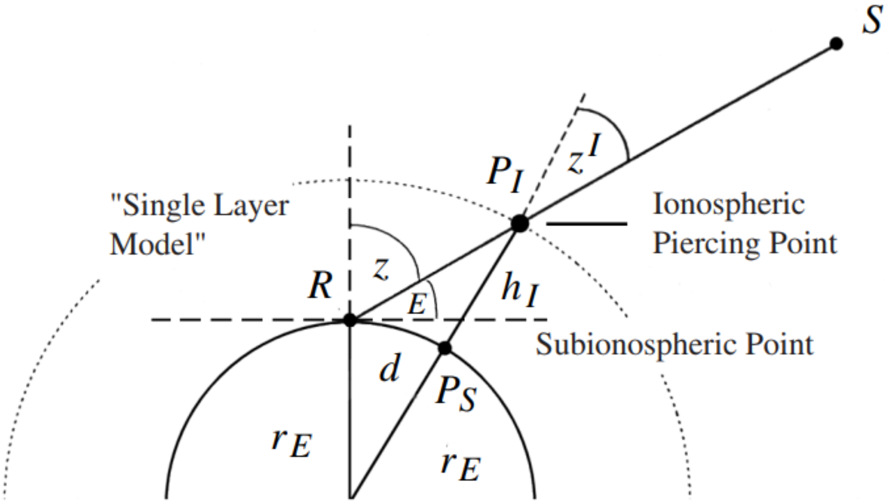

FIGURE 2.4 – Model where the ionosphere is represented by a simple layer (SEEBER, 2003).

In the Figure 2.4, P_I represents the IPP along the signal path from the satellite S to the receiver R, while P_S is the subionospheric point, and r_E is the Earth's radius (EMMERT J.AND RICHMOND; DROB, 2010). The angle z^I is the zenith angle from the satellite S to the observer R. Using these definitions, the angle z^I can be calculated as (SEEBER, 2003):

$$z^I = \arcsin\left(\frac{r_E}{r_E + h_I}\sin z\right). \tag{2.52}$$

TEC values range from 10^{16} to 10^{19} electrons/m^2 (or from 1 to 1,000 TECU) along the radio wave path. This density is highly variable and depends on several factors, including geographical location, time of day, season, and solar activity (SEEBER, 2003; HOFMANN-WELLENHOF *et al.*, 2008; PEREIRA; CAMARGO, 2013).

The equatorial ionosphere is characterized by high electron density, with various phenomena occurring in this region (PEREIRA; CAMARGO, 2013). Latitudes located into an EIA exhibit high TEC values, where plasma is elevated at the magnetic equator during the day and descends due to gravity and diffusion along magnetic field lines (SEEBER, 2003; MARUYAMA, 2020), analogous to a water source rising vertically through a jet and descending laterally (PEREIRA; CAMARGO, 2013). The EIA region also exhibits significant diurnal changes in TEC, primarily driven by the intensity of the equatorial electrojet (MUKHERJEE *et al.*, 2010). During some geomagnetic storms driven by the southward orientation of the interplanetary magnetic field (B_z), TEC values in the EIA region decrease. This reduction is influenced by changes in neutral composition, enhanced recombination, and meridional winds driven by asymmetric energy deposition at the poles (FAGUNDES *et al.*, 2008; HARSHA *et al.*, 2020). Thus, TEC maps are valuable for investigating ionospheric gradients resulting from geomagnetic storms, the EIA, plasma bubbles, TIDs, and gravity waves (HARSHA *et al.*, 2020).

Particularly, in the Brazilian sector, a peak in electron density is observed between 12:00 and 16:00 LT. A second peak occurs at low latitudes between 21:00 and 22:00 LT, after sunset, with this second peak exceeding the afternoon peak. Seasonally, the lowest electron density values are observed around the summer and winter solstices, while the highest values are observed during the equinox months of March-April and September-October, according to data published by Pereira and Camargo (2013) and other studies (ABDU *et al.*, 2003; SEEMALA; VALLADARES, 2011).

2.2.5 Global Navigation Satellite System - GNSS

TEC data are collected by a constellation of satellites that are part of the *Global Navigation Satellite System* (GNSS), including the *Global Positioning System* (GPS) operated by the United States, *GALILEO* operated by the European Union, and *Global Orbiting Navigation Satellite System* (GLONASS) operated by Russia (SEEBER, 2003; DARDARI *et al.*, 2012; PEREIRA; CAMARGO, 2013), among others. These satellite constellations are strategically important for various modern applications such as defense, civil protection, agriculture, and transportation. Particularly, the GPS constellation consists of 31 satellites positioned in 6 orbital planes centered on Earth. Each plane can contain 5 to 6 satellites, and each satellite orbits approximately 20,200 km above the Earth's surface, completing one orbit in about 11 hours and 58 minutes (DARDARI *et al.*, 2012). Ionospheric TEC maps, for instance, are generated using data from GPS operations and are relevant to GNSS users (HARSHA *et al.*, 2020). This thesis utilized GPS data collected from *braz* receiver station (MACHADO; AGUIAR, 2016) where this location and other details are more explained in section 4.2.1.

GPS is authorized for public use and offers positioning accuracy of approximately ±10 to ±15 meters on land, sea, air, and space. It has been operational since 1973 under the *US Department of Defense* (DoD) and was made available for civilian use starting in 1983. The GPS constellation design ensures a minimum of 4 satellites above the horizon at any given time. However, if large-scale irregularities in electron density affect the receiver's signal path, the receiver may lose signals from multiple satellites simultaneously, thereby disrupting navigation or degrading accuracy. Depending on the intensity of such scintillations, there may be a risk of failure in GNSS navigation continuity and availability. Despite decades of study on atmospheric irregularities, the exact effects of these irregularities on GPS signals are still not fully understood, leaving the navigation system vulnerable, particularly during intense events. When such events occur, significant fluctuations in TEC can complicate phase ambiguity resolution, increase the frequency of undetected or uncorrected *cycle slips*, and cause GNSS signal loss (PI *et al.*, 1997; MA; MARUYAMA, 2006; CHERNIAK *et al.*, 2014; FAGUNDES *et al.*, 2008; AOL *et al.*, 2020; LUO *et al.*, 2022; NGUYEN *et al.*, 2022).

The frequencies produced by GPS satellites correspond to the fundamental frequency $f_0 = 10.23$ MHz or $f_0 = 10.22999999543$ MHz, when accounting for relativistic effects. Each satellite transmits two frequencies in the L-band (1-2 GHz) for civilian use, derived from the fundamental frequency within the spectrum allocated by the *International Telecommunication Union* (ITU) (PI *et al.*, 1997; MCDONALD, 2002; SEEBER, 2003; RICHARDS, 2008; HOFMANN-WELLENHOF *et al.*, 2008):

$$L_1 : 154 \times 10.23\,\mathrm{MHz} = 1575.42\,\mathrm{MHz} \sim 19.0\,\mathrm{cm} \tag{2.53}$$

$$L_2 : 120 \times 10.23\,\mathrm{MHz} = 1227.60\,\mathrm{MHz} \sim 24.4\,\mathrm{cm}. \tag{2.54}$$

These two frequencies, when combined, help eliminate the largest sources of first-order error (HOFMANN-WELLENHOF *et al.*, 2008; PEREIRA; CAMARGO, 2013). TEC is directly proportional to the ionospheric *delay* between the L_1 and L_2 signals (HARSHA *et al.*, 2020). Consequently, when L-band radio waves from navigation systems pass through the ionosphere, they experience delays in propagation time, as well as changes in phase, amplitude, and polarization (MA; MARUYAMA, 2006; PEREIRA; CAMARGO, 2013).

2.2.6 Models of Forecast for the Ionopshere State

Given the availability of data on the factors affecting the occurrence of ionospheric irregularities, a natural progression is to develop forecasting strategies. Several studies have already attempted to predict the state of the ionosphere using various models and input data. For instance, Atabati et al. (2021) applied a neural network combined with a genetic algorithm to design a solar-quiet model, using input variables such as the maximum F_2 layer height, vertical drift, solar flux, sunspot numbers, and the K_p index. Abdu et al. (2003) used cubic-B splines to model spread-F occurrence, based on ionosonde data from Fortaleza (3.9°S, 38.45°W, dip angle: -9°) and Cachoeira Paulista (22.6°S, 315°E, dip angle: -28°) covering the period from 1978 to 1990. Their model included local time, season, solar flux, and latitude as explanatory variables.

Rezende et al. (2010) employed ionosonde data from São Luís (2.3°S, 44.2°W, dip angle: -1.5°) and GNSS receivers from both São Luís and São José dos Campos (23.1°S, 45.8°W, dip angle: -32°) to predict ionospheric scintillation. Their model utilized bootstrap aggregation and decision tree algorithms, with input variables including vertical drift velocity over the equator, solar flux, F layer virtual height ($h'F$), and S_4. This model, based on ionosonde data recorded between 17:00 and 19:00 LT from 2000 to 2002 under magnetic quiet conditions, achieved a classification accuracy of 95.5%. Another study by Das et al. (2010) also used S_4 measurements — from VHF and L-band signals — recorded in Kolkata (22.58°N, 88.38°E, dip angle: 32°N) from 1996 to 2006, under magnetic quiet conditions. Their neural network-based model used input variables such as local time, month of the year, and mean monthly solar flux, achieving a mean square error of 0.36.

Souza et al. (2012) modeled the F_2 critical frequency using multidimensional Fourier series, with input variables including day of the year, latitude, longitude, altitude, and time, for four locations in South America. Their model, called the Parameterized Regional Ionosphere Model (PARIM), did not account for geomagnetically perturbed periods. Goncharenko et al. (2021) modeled the TEC at a mid-latitude location (45° N, 0° E) using input variables such as solar flux, season, geomagnetic activity, and the cross-modulation of these factors.

A recent study by Hysell et al. (2022) proposed an entirely physical model — in contrast to semi-empirical ones — based on a regional ionospheric irregularity model coupled with the Whole Atmosphere Model-Ionosphere Plasmasphere Electrodynamics (WAM-IPE). Their model was designed to reproduce data from Incoherent Scatter Radar (ISR) measurements collected at the Jicamarca Radio Observatory in September 2021. While the model did not achieve high accuracy due to factors such as the nonlinear nature of the equations, inaccuracies in the input data, and the absence of initial oscillations (e.g., gravity waves), it provided a detailed description of the ionospheric irregularities, including their spatiotemporal distribution over a certain length scale, in a deterministic manner. Finally, the Wideband Ionospheric Scintillation Model (WBMOD), a semi-empirical model developed in the 1970s, should also be mentioned. WBMOD uses input quantities such as location, day of the year, time of day, and the K_p index (SECAN *et al.*, 1995).

Several other studies, such as the one by Klipp et al. (KLIPP *et al.*, 2019), also propose models to predict the state of the ionosphere. However, most of these models do not account for geomagnetically perturbed periods.

3 Methodology

3.1 Gravity Waves

3.1.1 Data Description and Instrumentation

Radiosondes are meteorological devices designed to measure atmospheric parameters *in situ*, such as temperature, humidity, pressure, and wind speed. Attached to a weather balloon, these instruments transmit data back to ground receivers in real-time. Radiosondes are capable of reaching altitudes of approximately 30 km, traversing up to 300 km horizontally from the launch site. Their robustness enables operations under extreme environmental conditions, including temperatures ranging from -95°C to 50°C and pressures below 1% of Earth's surface pressure (DABBERDT; TURTIAINEN, 2015; WORLD METEROLOGICAL ORGANIZATION, 2018). A photo of an operator preparing for a radiosonde launch and an scheme about the radiosonde components are depicted in Figure 3.1.

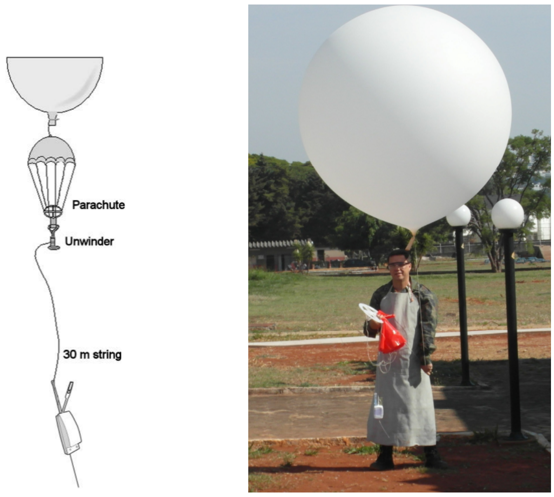

FIGURE 3.1 – Typical schematic of meteorological balloon components (radiosonde on the left) and an operator preparing for a radiosonde launch (right). (BRASIL, 2013; DABBERDT; TURTIAINEN, 2015).

In Brazil, radiosonde launches are conducted in compliance with national regulations established by the Brazilian Air Force (*Comando da Aeronáutica*) and international standards set by the World Meteorological Organization (WMO). The *Vaisala RS92-SGP* model is one of the primary radiosondes used within the country, favored for its precision and reliability in capturing atmospheric profiles, particularly for studies involving GWs (OLIVEIRA, 2016; BRASIL, 2022).

The data collected from radiosondes are critical for a range of applications, including weather forecasting, climate modeling, and atmospheric research. For instance, analyzing small-scale fluctuations in temperature profiles captured by radiosondes provides valuable insights into GWs activity. These phenomena are pivotal in understanding energy and momentum transfer in the atmosphere, especially in tropical regions like Brazil (FRITTS; ALEXANDER, 2003; NAPPO, 2013).

By adhering to globally standardized launch schedules—typically at 00:00 and 12:00 UTC — Brazil's radiosonde network contributes to international meteorological datasets, ensuring consistent and high-quality observations. The integration of advanced tracking technologies, such as GPS, enhances the accuracy of wind measurements, facilitating the comprehensive analysis of atmospheric dynamics (DABBERDT; TURTIAINEN, 2015; WORLD METEROLOGICAL ORGANIZATION, 2018).

The radiosonde measurements used in this thesis were collected in 32 aerodromes throughout the Brazilian territory in 2014, as shown in Figure 3.2. The choice of this data set was guided by the need of covering the largest area of the Brazilian territory in a time period of at least one year. The radiosondes performed measurements of wind, temperature, humidity and pressure as a function of altitude and sent them to the ground station by radio signal. All the launches of radiosondes officially take place in Brazil at 00:00 and 12:00 UTC and usually start 30 to 45 min before the standard time, according to national and international recommendations (BRASIL, 2013; BRASIL, 2017; WORLD METEROLOGICAL ORGANIZATION, 2018).

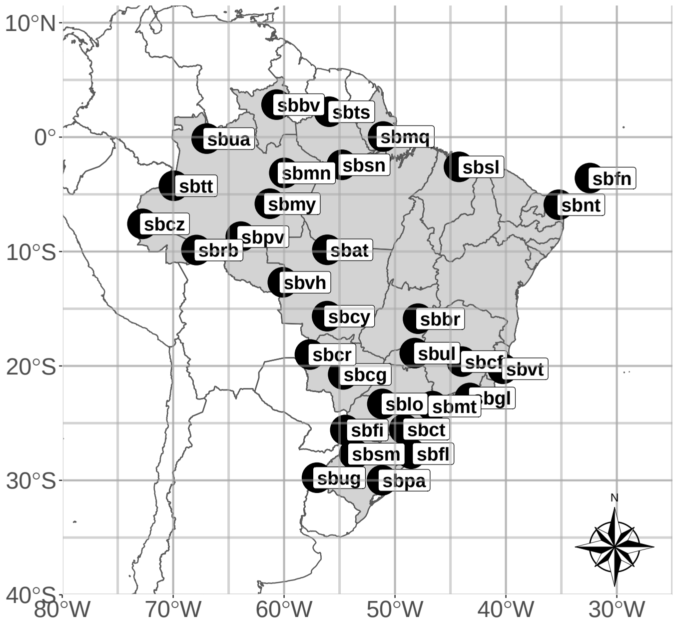

FIGURE 3.2 – The maps show the aerodromes operated by ICEA that provided the radiosonde data used in this study. The characteristics of the aerodromes are shown in Table 3.1.1. The geographic descriptions of each aerodrome are shown in Table 3.1.1 (BRHIAN *et al.*, 2024)

In some dates in 2014 the measurements were not performed and these cases were classified as missing data or not available (NA). In many aerodromes, measurements were performed almost twice a day, totalling nearly 730 measurements. On average, each station performed around 400 valid measurements in the troposphere and around 320 measurements in the lower stratosphere. Typically, more measurements were carried out during the dry period (fall/winter). Table 3.2 shows the number of profiles analysed by period, kind of energy and atmospheric layer, summing up a total of 49,652 valid wind and temperature profiles. The number of profiles used to compute the kinetic and potential energy densities are presented separately because the first is derived from wind altitude profiles while the second is derived from temperature profiles. In some cases, one type of measurement may be present while the other not, which explains why for a given time period the number of measurements are not the same. It should also be noted that samples sizes of troposphere measurements are around 10% larger than the ones of stratosphere measurements due to the fact that some radiosondes fail before reaching the threshold altitude of the stratospheric analysis layer, which is set at 25 km.

TABLE 3.1 – Information of aerodromos controled by ICEA during 2014 (BRHIAN *et al.*, 2024).

	Aerodrome	City	UF	Latitude (°)	Longitude (°)	Altitude (m)	Region
1	sbat	ALTA FLORESTA	MT	-9.87	-56.10	289	CO
2	sbbr	BRASÍLIA	DF	-15.87	-47.92	1066	CO
3	sbbv	BOA VISTA	RR	2.84	-60.69	84	N
4	sbcf	CONFINS	MG	-19.62	-43.97	827	SE
5	sbcg	CAMPO GRANDE	MS	-20.47	-54.67	559	CO
6	sbcr	CORUMBÁ	MS	-19.01	-57.67	141	CO
7	sbct	CURITIBA	PR	-25.53	-49.18	911	S
8	sbcy	VÁRZEA GRANDE	MT	-15.65	-56.12	188	CO
9	sbcz	CRUZEIRO DO SUL	AC	-7.60	-72.77	194	N
10	sbfi	FOZ DO IGUAÇU	PR	-25.60	-54.48	240	S
11	sbfl	FLORIANÓPOLIS	SC	-27.67	-48.55	5	S
12	sbfn	FERNANDO DE NORONHA	PE	-3.85	-32.43	58	NE
13	sbgl	RIO DE JANEIRO	RJ	-22.81	-43.25	9	SE
14	sblo	LONDRINA	PR	-23.33	-51.14	569	S
15	sbmn	MANAUS	AM	-3.04	-60.05	80	N
16	sbmq	MACAPÁ	AP	0.05	-51.07	17	N
17	sbmt	SÃO PAULO	SP	-23.51	-46.63	722	SE
18	sbmy	MANICORÉ	AM	-5.82	-61.28	53	N
19	sbnt	NATAL	RN	-5.90	-35.23	52	NE
20	sbpa	PORTO ALEGRE	RS	-29.99	-51.17	4	S
21	sbpv	PORTO VELHO	RO	-8.71	-63.90	88	N
22	sbrb	RIO BRANCO	AC	-9.87	-67.90	193	N
23	sbsl	SÃO LUÍS	MA	-2.59	-44.24	54	NE
24	sbsm	SANTA MARIA	RS	-29.71	-53.69	88	S
25	sbsn	SANTARÉM	PA	-2.42	-54.79	60	N
26	sbts	ÓBIDOS	PA	-2.22	-55.93	344	N
27	sbtt	TABATINGA	AM	-4.25	-69.94	85	N
28	sbua	SÃO GABRIEL DA CACHOEIRA	AM	-0.15	-66.99	76	N
29	sbug	URUGUAIANA	RS	-29.78	-57.04	78	S
30	sbul	UBERLÂNDIA	MG	-18.88	-48.23	943	SE
31	sbvh	VILHENA	RO	-12.69	-60.10	615	N
32	sbvt	VITÓRIA	ES	-20.26	-40.29	3	SE

The vertical spacing of the radiosonde measurements ranged between 40 m to 90 m, with median value of 60 m. Since all the analyses to be described next required regularly spaced data, all the profiles were interpolated to a 50 m grid using a standard linear interpolation method (MOFFAT-GRIFFIN *et al.*, 2011).

TABLE 3.2 – Number of radiosonde altitude profiles used to estimate the potential and kinetic energy densities in 2014 for the 32 aerodromes (BRHIAN *et al.*, 2024).

		Dry	**Wet**	Total
Troposphere	**Kinetics**	7,296	6,332	13,628
	Potential	6,659	6,457	13,116
	Total	13,955	12,789	*26,744*
Lower Stratosphere	**Kinetics**	5,380	5,094	10,474
	Potential	6,503	5,931	12,434
	Total	11,883	11,025	*22,908*

3.1.2 Cluster Analysis

Cluster analysis was performed to identify regions with similar wind profiles and energy density patterns for GWs. This method enables the classification of aerodromes into groups where atmospheric conditions, such as seasonal and spatial variability, exhibit similar behavior. By grouping the data, it becomes possible to simplify the analysis, highlight regional differences, and investigate how these variations influence the propagation and characteristics of GWs.

Before the search for GWs, we studied the overall behaviour of the wind height profiles. The objective of this study was to verify the consistency of the data while also getting some insight on the mean atmosphere dynamics over the studied period. The study of the wind profiles was aided by a cluster analysis, as follows. Firstly, a metric was chosen to calculate the distance between one profile and another - the Euclidean distance metric (not to be confused with the physical space distance between two points in planar topology). As there were 32 stations, then $\binom{32}{2} = 496$ (the notation $\binom{n}{k}$ corresponds to the binomial coefficient, defined as $\binom{n}{k} = \frac{n!}{k!(n-k)!}$ - it is used to compute the number of ways of selecting k items without replacement and order distinction from a collection of n items) distance measurements were need to build the dissimilarity matrix (or proximity). After that, the clusters were computed using the following hierarchical linking methods: average, single, complete and Ward's method (HAIR *et al.*, 2006). In order to choose the best linking method, they were ranked according to their agglomerative coefficient (AC), defined as (KAUFMAN; ROUSSEEUW, 2005; PANDOVE *et al.*, 2018):

$$AC = \frac{1}{n} \sum_{i=1}^{n} [1 - r(i)], \tag{3.1}$$

where n is the total number of profiles and $r(i)$ is the distance from the first cluster in which the profile was inserted divided by the distance in the final step of the algorithm. The values of AC range from 0 (indicating that no clustering was found) to 1 (indicating strong clustering structure). The Ward's linking method proved to be optimal in all cases. Also, a number of 5 clusters was found to be a reasonable choice based on standard statistical criteria (KAUFMAN; ROUSSEEUW, 2005).

3.1.3 Kinetic and Potential Energy Densities

Next, we determined the kinetic and potential energy densities of GWs in the troposphere (surface–11 km) and lower stratosphere (18–25 km). The tropopause region was purposely avoided, following the approach of other works that apply the same method (GELLER; GONG, 2010; VINCENT; ALEXANDER, 2000; YOSHIKI; SATO, 2000; ZHANG; YI, 2005; MOFFAT-GRIFFIN *et al.*, 2011; MOFFAT-GRIFFIN *et al.*, 2020). The reason for that choice is that the tropopause region usually presents strong wind shear and variation, which can be mistakenly taken as a GW effect. Also, in the temperature case, the tropopause minimum may yield spurious oscillations that could be mistakenly taken as

GWs. Figure 3.3 shows a radiosonde hodograph where the wind in the tropopause region presents strong variation.

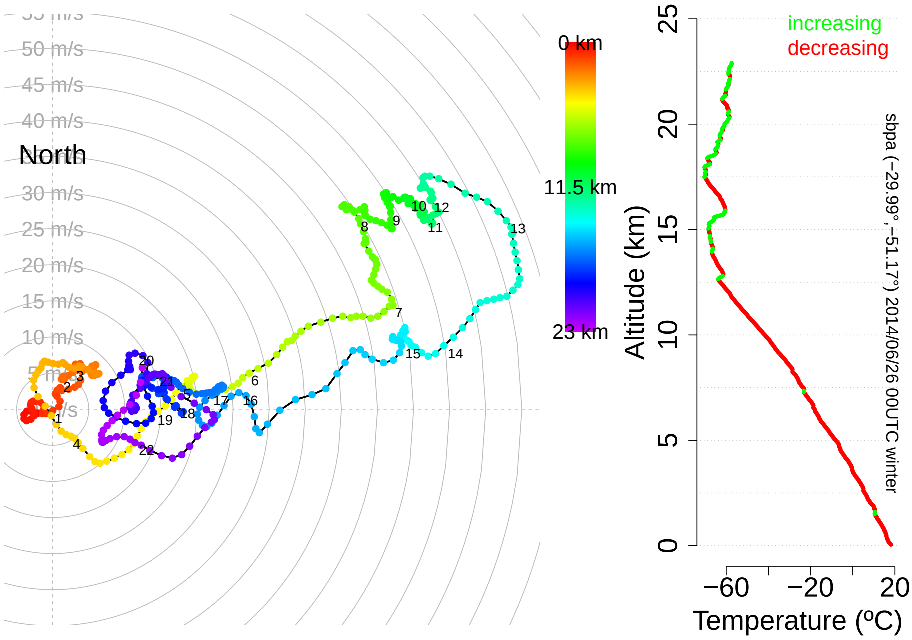

FIGURE 3.3 – Hodograph (left) and temperature profile (right) from sbpa's aerodrome $(-29.99°, -51.17°)$ on 26^{th}, June 2014 at 00:00 UTC. The increasing and decreasing color code represent when the temperature gradient are respectively positive or negative. The numbers along the hodograph represent altitude levels (BRHIAN *et al.*, 2024).

The kinetic energy E_K and the potential energy E_P densities are defined as (GILL, 1982; GELLER; GONG, 2010; STULL, 1988; VINCENT; ALEXANDER, 2000; YOSHIKI; SATO, 2000; ZHANG; YI, 2005; MOFFAT-GRIFFIN *et al.*, 2011; MOFFAT-GRIFFIN *et al.*, 2020; AYORINDE *et al.*, 2023; AYORINDE *et al.*, 2024):

$$E_K = \frac{1}{2}(\overline{u'^2} + \overline{v'^2}) \tag{3.2}$$

$$E_P = \frac{1}{2}\frac{g^2\overline{T'^2}}{N^2 T_0^2} \ , \tag{3.3}$$

where $N = g\sqrt{\frac{\gamma-1}{\gamma}\frac{M_{air}}{RT_0}}$ is the *Brunt-Väisälä* frequency, overline correspond to averaged values over the layer length, primed variables correspond to wave perturbation, u is the zonal wind, v is the meridional wind, $g = 9.81$ m/s^2 is the mean gravitational acceleration, $\gamma = 1.4$ is the adiabatic index of air, $M_{air} = 28.96 \times 10^{-3}$ kg/mol is the molar mass of air, $R = 8.31$ J/(mol·K) is the ideal gas constant, $T_0 = T_0(z)$ is the unperturbed background temperature and T' is the perturbation from T_0, both of which were computed after the detrending procedure described next.

The estimate of primed amplitudes was made by a Linear Squares Method (LSM) procedure that removed the background wind or temperature assuming that it had a parabolic shape (VINCENT *et al.*, 1997; ZHANG; YI, 2005; MOFFAT-GRIFFIN *et al.*, 2011), i.e.

$$y' = y - \hat{a}h^2 - \hat{b}h - \hat{c}\ . \tag{3.4}$$

After removing the trend, the Power Spectrum Density (PSD) was computed using the FFT (MARTINSON, 2018; PRESS *et al.*, 2007; STULL, 1988). The quadratic sum of the FFT components yields the mean kinetic and potential energy densities (STULL, 1988). The mean square of the primed quantities is computed as (VINCENT; ALEXANDER, 2000; ZHANG; YI, 2005):

$$\overline{y'^2} = \frac{1}{2M}\sum_{k=0}^{M-1} Y_k' Y_k'^{*}\ , \tag{3.5}$$

where $\hat{a}$, $\hat{b}$ and $\hat{c}$ are coefficients to be determined, Y_k' is the FFT component and $Y_k'^{*}$ its conjugate and M is the size of the time/spatial series. An example of a detrended profile is shown in Figure 3.4. The amplitude, wavelength, and phase of the profiles were estimated using the FFT. Subsequently, the wavelength was further refined by applying the LSM on a grid of wavelengths with a 25-meter resolution. Since energy densities are computed using the amplitudes of the FFT components for a given layer, the energy densities are only layer dependent, not height dependent.

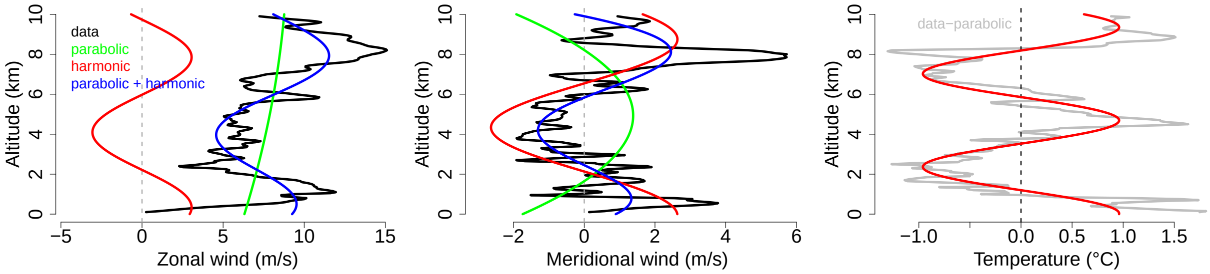

FIGURE 3.4 – Zonal wind (left), meridional wind (middle) and temperature minus parabolic fit radiosonde altitude profile (right) from aerodrome SBMN (Manaus - Brazil) measured in 05/14/2014 at 12:00 UTC (black) and the fitting curve (blue). The lines corresponding to the harmonic (red), parabolic (green) contributions for the fitting curve and the data minus parabolic fitting curve (gray - only for temperature profile) are also shown (BRHIAN *et al.*, 2024).

The energy densities are computed for all profiles where data was available over the full extent of the layer range. The overall statistics of the energy density provides information about the state of perturbation of the TLS. In order to verify the existence of a trend in the time series of the kinetic and potential energy densities we used a nonlinear smoother called Centered Moving Medians (MdC) with bandwidth equal to h. The median is a robust measure of the central tendency, defined as the value separating the higher half from the lower half of a data sample. The median has the advantage of not being influenced by outliers. If $\{X_1, X_2, \ldots, X_N\}$ is a time series of size N, then the MdC filter Y_i is defined as (ARCE, 2005; COWPERTWAIT; METCALFE, 2009):

$$Y_i = Md[X_{i-h}, ..., X_i, ..., X_{i+h}] \ , \tag{3.6}$$

where i ranges from $h+1$ to $N-h$ and $Md[\cdot]$ is the median of the values within brackets. Note that the MdC filter can not be applied to data samples where $i \leq h$ or $i \geq N-h$.

After estimating the kinetic and potential energy in each atmospheric layer, this work determined the probability density function (PDF) for each dataset. It was observed that the energy values were strictly positive, as expected, and exhibited asymmetry in their distributions. Therefore, the recommended probability density function for fitting this type of data was the Gamma distribution $X \sim Gamma(k, \theta)$, where X is a random variable, is defined as (JOHNSON *et al.*, 1995; DEVORE, 2016):

$$f(x|k,\theta) = \frac{x^{k-1} e^{-\frac{x}{\theta}}}{\theta^k \Gamma(k)}, \ x > 0 \tag{3.7}$$

where $k > 0$ is the shape parameter, $\theta > 0$ is the scale parameter, and $\Gamma(k) = \int_0^\infty t^{k-i} e^{-t} dt$ is the Gamma function.

The mean (μ) and standard deviation (σ) of the Gamma distribution can be computed using the shape and scale of a Gamma Distribution parameter as (JOHNSON *et al.*, 1995; DEVORE, 2016):

$$\mu = k\theta, \ \sigma = \sqrt{k}\theta. \tag{3.8}$$

For comparison, the Normal distribution $X \sim Normal(\mu, \sigma)$, commonly used for symmetric data, is defined as:

$$f(x|\mu,\sigma) = \frac{1}{\sqrt{2\pi\sigma^2}} \exp\left(-\frac{(x-\mu)^2}{2\sigma^2}\right), \ x \in \mathbb{R}, \tag{3.9}$$

where μ is the mean and σ is the standard deviation. However, the Normal distribution is unsuitable for this study due to its support on the entire real line, which contradicts the strictly positive nature of the energy data.

We used the Spearman's correlation coefficient to investigate the spatial correlations in the kinetic and potential energy densities between distinct aerodromes. This nonparametric and nonlinear statistics was chosen in this case because the data was not normally distributed (DEVORE, 2016). The Spearman's coefficient consider positive correlation (or monotonic increase) when its value is close to 1, negative correlation (or monotonic decrease) when its value is close to -1 and without correlation when its value is close to 0 (BAGDONAVICIUS *et al.*, 2011; BISHARA; HITTNER, 2012; GIBBONS; CHAKRABORTI, 2011; KANJI, 2006). The correlation coefficients were plotted against the Haversine distance (great circle distance) between the aerodromes (BRUMMELEN, 2013).

The Spearman's correlation coefficient was also used to investigate the correlation between physical quantities measured in the troposphere and the lower stratosphere. In this case, the pair of variables subjected to correlation calculation belonged to the same aerodrome or distinct aerodromes. The Spearman's correlation coefficient was then computed over all available launches. Using this approach, we aimed at verifying quantitatively the strength of the coupling between GWs in the troposphere and GWs in the lower stratosphere. If GWs observed by the radiosonde on the troposphere often propagate to the stratosphere, or vice versa, then there is a physical reason to expect correlations on the wave amplitudes and energy densities. If no correlation is observed, then we may speculate that GWs in the wave frequency interval measured by radiosondes do not cross the tropopause.

3.1.4 Monochromatic GWs

The values of the dominant wavelengths of the winds and temperature profiles of GWs were not always consistent with each other. In the case of monochromatic waves, the dominant wavelengths must be consistent. To identify monochromatic waves, we used the following procedure. Firstly, we took the wavenumber of the highest FFT component of a given height profile (e.g., zonal wind) as a guess of the vertical wavelength. After that, linear LSM (PRESS *et al.*, 2007) was used to estimate the phase and amplitude of the dominant sinusoidal component of the wave, while its wavelength was estimated using a search algorithm in an evenly spaced grid with spacing $\Delta\lambda = 25$ m between 0.5 and 12.0 km. This procedure was repeated for the remaining two height profiles (*e.g.*, meridional wind and temperature). A quasi-monochromatic (NAPPO, 2013; MOFFAT-GRIFFIN *et al.*, 2011) GW was assigned only if the coefficient of variation (CV) of the three wavelengths was less than or equal to 20%, following the same approach of Zhang e Yi (2005). The CV is defined as the ratio between the standard deviation σ_{λ_z} to the mean $\overline{\lambda_z}$ from the vertical wavelengths (DEVORE, 2016):

$$CV = \frac{\sigma_{\lambda_z}}{\lambda_z}. \tag{3.10}$$

Once the vertical wavelength and the phase of the wave in each wind component are known, it is possible to determine other wave parameters such as wave frequency and horizontal wavelength. This requires the application of the dispersion and polarization relations derived from the theory of linear plane wave propagation for GWs (FRITTS; ALEXANDER, 2003; NAPPO, 2013; SCHUNK; NAGY, 2009).

To determine the wave-frequency (see Equation 2.37), we used the polarization relation (FRITTS; ALEXANDER, 2003; NAPPO, 2013; ZHANG; YI, 2005):

$$\tilde{v} = -i\frac{f}{\hat{\omega}}\tilde{u}, \tag{3.11}$$

where f is the Coriolis frequency, $\tilde{v}$ and $\tilde{u}$ are the complex horizontal amplitudes of the harmonic functions representing the wind oscillations due to GWs and $\hat{\omega}$ is its intrinsic angular frequency. The amplitudes $\tilde{v}$ and $\tilde{u}$ were extracted graphically from the hodographs of the horizontal wind components described by the fitted harmonic functions (ZHANG; YI, 2005). Equation 3.11 is valid in latitude ranges not so close to the equator where Coriolis force is negligible ($f \approx 0$), the polarization relations are not useful to determine $\hat{\omega}$, because the wave is not circularly polarized. Equation 3.11 shows that $\tilde{v}$ and $\tilde{u}$ are lagged by $\pi/2$ and the ratio between the major axis and the minor axis of the ellipsis generated by the wind hodograph of the monochromatic wave equals $\hat{\omega}/f$. A latitude threshold of 20° was chosen so that only data from stations south of this latitude was used in the analysis. By doing so, it can be safely assumed that $\hat{\omega} > f$, like discussed in Subsection 2.1.2. Once the ratio $\hat{\omega}/f$ is computed from the empirically determined hodograph, it is multiplied by the Coriolis frequency. This method can be applied to determine $\hat{\omega}$ if both buoyancy and Coriolis forces are important, in which case GWs are referred to as inertia-gravity waves (FRITTS; ALEXANDER, 2003). This is the case for GWs detected by radiosonde data, for which the measurable vertical wavelengths fit within the range of inertia-gravity waves where $\hat{\omega} \gtrsim f$ (FRITTS; ALEXANDER, 2003).

The horizontal wave-number k_H (with corresponding wavelength λ_H) can also be determined. This was done using the following dispersion relation,

$$k_H^2 = k_z^2\frac{\hat{\omega}^2 - f^2}{N^2}. \tag{3.12}$$

This dispersion relation is derived using a linear non-dissipative plane wave propagation theory for GWs (NAPPO, 2013) when assuming that $N \gg \hat{\omega}$ and $1/(4H^2) \ll k_z^2$, where H is the atmospheric scale height.

3.2 Ionosphere

After the detailed analysis of GWs in the Brazilian lower atmosphere, it is appropriate to transition to the second part of this investigation, which focuses on predicting ionospheric irregularities. In this section, we present the methodology used to develop a predictive model based on GLMs, tailored to the specificities of ionospheric conditions at low latitudes. This model was constructed using 12 years (from 1^{st}, January of 2010 to 18^{th}, April of 2022) of data collected from the Brasília station (braz), incorporating variables such as the K_p index, solar flux ($F_{10.7}$), time left to sunrise (TLS), and the maximum Elevation Angle of the Sun (EAS). The following subsections detail the process of constructing, calibrating, and validating the model, highlighting its statistical foundation and the importance of each explanatory variable.

The workflow of the classification model is summarized below. In the next sections, each of these steps is discussed in detail.

1. The state of the ionosphere was classified as *regular* or *irregular* using 5-minute ROTI values, with a classification of *irregular* if ROTI ≥ 0.5 and *regular* otherwise;
2. Four quantities were selected as explanatory variables: time left to sunrise (TLS), the elevation angle of the Sun (EAS), $F_{10.7}$ index and K_p. Their interactions were also used as explanatory variables;
3. Eight different models, presented in Table 4.5, were developed to classify the state of the ionosphere by taking different link functions and factor variables;
4. The data was randomly split, allocating 70% for training and 30% for testing;
5. A threshold criterion was established to classify the ionosphere state, a confusion matrix was computed and several metrics, including False Negative Rate (FNR), False Positive Rate (FPR) and Area Under the Receiver Operating Characteristic Curve (AUC-ROC), were evaluated;
6. The GLM model with a *logit* link function was analyzed in detail, leveraging the fact that its coefficients and odds ratios are easier to interpret;
7. Finally, all models were evaluated and selected based on their FNR, FPR and AUC-ROC values, besides of parcimony.

3.2.1 Rate of TEC Index - ROTI

The GPS data was retrieved from a database maintained by the *Brazilian Network for Continuous Monitoring* (RBMC), which is a network of geodetic stations managed by the Brazilian Institute of Geography and Statistics (IBGE). Each station is equipped with a high-performance GNSS receiver that provides correction data for GNSS positioning (INSTITUTO BRASILEIRO DE GEOGRAFIA E ESTATÍSTICA, 2024).

The data was downloaded as standard RINEX (Receiver INdependent EXchange) files in format version 2.11 (CHERNIAK *et al.*, 2015; IGS, 2024). The *Slant Total Electron Content*, designated here as TEC, was evaluated using free software (SEEMALA, 2024) made available by Seemala and Valladares (2011) and was detailed in (SEEMALA, 2023). This software implements processing procedures proposed by Zhang *et al.* (2009), which have been widely applied in other ionospheric studies (ATABATI *et al.*, 2021; CARMO *et al.*, 2021; CARMO *et al.*, 2022; GONZáLEZ, 2022; ABREU *et al.*, 2023).

To compute the Rate of TEC Index (ROTI), the *Rate of TEC* (ROT) must be evaluated. This quantity is defined as the numerical time derivative of TEC, expressed in units of TECU/min, *e.g.* $ROT = \dfrac{TEC(t+\Delta t) - TEC(t)}{\Delta t}$, where Δt is the time difference between two acquisitions. The ROTI was computed as the standard deviation of the ROT values within a 5-minute interval, following the instructions provided by Pi *et al.* (1997). Formally, the ROTI is defined as:

$$ROTI = \sqrt{\overline{ROT^2} - \overline{ROT}^2} = sd(ROT), \tag{3.13}$$

where $sd(\cdot)$ denotes the standard deviation of the ROT within a 5-minute interval. To minimize noise and multipath errors, an elevation mask of 30° was applied to all GPS satellite data (MA; MARUYAMA, 2006; ZHANG *et al.*, 2009; REZENDE *et al.*, 2010; SEEMALA; VALLADARES, 2011; ATABATI *et al.*, 2021; CARMO *et al.*, 2022; GONZáLEZ, 2022; LUO *et al.*, 2022; NGUYEN *et al.*, 2022).

At each 5-minute interval, the ROTI values for each satellite were sampled and their third quartile was computed. If the third quartile was lower than 0.5, the ionosphere was classified as *regular*; otherwise, it was classified as *irregular* (MA; MARUYAMA, 2006; CHERNIAK *et al.*, 2014; HARSHA *et al.*, 2020; PI *et al.*, 1997). The third quartile was chosen instead of the mean because it is less sensitive to outliers, which may occur when the elevation is near the 30° limit. Additionally, this method allows for the selection of conditions where at least 25% of the satellites exhibit large ROTI values. With an average of 8 to 12 visible satellites in the GPS constellation (SEEMALA; VALLADARES, 2011), setting the threshold at the median may result in more than 4 viable satellites for geolocation.

However, if only 4 to 7 satellites are available, it is prudent to set the threshold above the median value for safety.

3.2.2 Independent Variables

The model is based on four explanatory variables: time left to sunrise (TLS), the elevation angle of the Sun (EAS), $F_{10.7}$ and K_p. The first variable, TLS, accounts for the dependence of the ionospheric irregularities on the daily variability. The second variable, EAS, accounts for seasonal variability. The third variable, $F_{10.7}$ index, accounts for the dependence of ionospheric irregularities on solar activity. Lastly, the fourth variable, the K_p index, accounts for geomagnetic activity. Each variable is discussed in the next subsections.

3.2.2.1 Time Left to Sunrise - TLS

The TLS variable is defined as the number of hours remaining until sunrise, measured from sunset. It is calculated using the following equations (MEEUS, 1998; OLIVEIRA FILHO; SARAIVA, 2011):

$$\begin{aligned} \text{TLS} &= \left[\left(\frac{H_{day}}{2} - 12\right) - t\right] \mod 24 \ , && (3.14) \\ H_{day} &= 2 \times \left|\frac{1}{15} \arccos(-\tan L \times \tan\delta)\right| \ , && (3.15) \\ \delta &= 23.44 \times \sin\left(360 \times \frac{DOY + 284}{365}\right), && (3.16) \end{aligned}$$

where H_{day} is the duration of daylight, t is a local time, mod denotes modular arithmetic, L is the geographic latitude, DOY is the *day of year* and δ is the solar declination.

The TLS variable is particularly relevant because certain irregularities, such as EPBs, are known to occur with greater frequency after sunset and around midnight (ABDU *et al.*, 2003), as illustrated in Figure 4.20. This probability tends to be higher at the beginning of the night, suggesting that larger values of TLS are associated with an increased likelihood of observing ionospheric irregularities.

The TLS value defined above was normalized, in order to obtain values between 0 and 1, by dividing it by the duration of the night, ensuring its maximum value remains invariant. For instance, if the local time is 21:00 LT and the raw TLS is 10 hours, the normalized variable ($TLSr$) is computed as follows:

$$\text{TLSr (21 h)} = \frac{(6\,\text{h} - 21\,\text{h}) \mod 24}{10\,\text{h}} = \frac{9}{10} = 0.9.$$

3.2.2.2 Maximum Elevation Angle of the Sun - EAS

The EAS variable represents the maximum angle between the position of the Sun in the sky and the horizon line for any given day. It primarily depends on geographic latitude and the DOY. The algorithm used to compute the EAS can be found in Van Doninck (2016).

This variable was used to account for the seasonal dependence of the ionospheric irregularities. In the Brazilian sector, it is established that irregularities are rare in winter but common during the period between the spring equinox and the autumn equinox, known as the Spread-F season or scintillation season (ABDU *et al.*, 1992; ABDU *et al.*, 2003). When irregularities occur in winter, they are typically associated with TIDs (AMORIM *et al.*, 2011; AMORIM *et al.*, 2012). The EAS is particularly suited for this purpose, as it reaches its maximum value at the summer solstice, its minimum value at the winter solstice and takes intermediate values during the equinoxes in Brazilian territory (ABDU, 2001; KLIPP *et al.*, 2019; ABDU, 2020).

A simple linear interpolation is applied between the minimum (50.63°) and maximum (86.66°) EAS values from braz station for normalization, in order to obtain values between 0 and 1. For example, if EAS in braz station is 70° on a given DOY, the normalized value ($EASr$) is computed as follows:

$$\text{EASr } (70^\circ) = \frac{70^\circ - 50.63^\circ}{86.66^\circ - 50.63^\circ} = \frac{19.37}{36.03} \cong 0.54 \ .$$

3.2.2.3 $F_{10.7}$ and K_p indices

The $F_{10.7}$ index is a widely used proxy for solar activity, well correlated with the sunspot number (TAPPING, 2013; KLIPP *et al.*, 2019; WOOD *et al.*, 2024). It measures the flux of electromagnetic waves with a wavelength of 10.7 cm (or a frequency of 2.8 GHz) emitted by the Sun. Higher solar activity corresponds to increased UV output, leading to greater rates of photoionization in the ionosphere (SCHUNK; NAGY, 2009; ASTAFYEVA, 2019; KLIPP *et al.*, 2019; GONCHARENKO *et al.*, 2021; WOOD *et al.*, 2024). Consequently, during periods of high solar activity, the ionosphere exhibits larger peak and integrated plasma densities, which increases the likelihood of ionospheric irregularities, as described by Rayleigh-Taylor Instability theory (MAKELA; MILLER, 2011; ABDU, 2020; HUBA, 2021;

GONZáLEZ, 2022). In this study, $F_{10.7}$ was normalized through linear interpolation between the minimum (63.4 sfu) and maximum (257.0 sfu) values observed during solar cycle 24, with missing data assigned the mean value (97.34 sfu).

The K_p index is a 3-hour measure of the geomagnetic component H, derived from 11 worldwide magnetometer stations. It reflects the strength of geomagnetic storms, as variations in the H component indicate geomagnetic activity. Ionospheric irregularities can be triggered or suppressed by the prompt penetration of electric fields or the disturbance dynamo electric fields following geomagnetic storms (HARGREAVES, 1995; ROSTOKER, 1972; CAMPBELL, 2003; OLSEN; STOLLE, 2017; GONCHARENKO *et al.*, 2021; GONZáLEZ, 2022; CARMO *et al.*, 2022; ABREU *et al.*, 2023). Despite the paradoxical behavior of storm time conditions, the model assumes that greater values of K_p should, on average, increase the probability of the occurrence of ionospheric irregularities. Based on the K_p index, data were classified into three categories according to the criteria from the British Geological Survey (BGS) and the National Oceanic and Atmospheric Administration (NOAA) (NOAA, 2024; BRITISH GEOLOGICAL SURVEY, 2024): *quiet* if $K_p \leq 3+$ (ATABATI *et al.*, 2021), *active* if $3+ < K_p \leq 5-$ and *storm* if $K_p > 5-$. Models were organized into two groups: in the first, K_p was labeled as *quiet* (Q), *active* (A), or *storm* (S); in the second, the data were categorized as *quiet* (Q) or *active-storm* (AS).

The K_p and $F_{10.7}$ indices were downloaded from the GSFC/SPDF OMNIWeb interface at https://omniweb.gsfc.nasa.gov (NASA, 2024).

3.2.3 Generalized Linear Models - GLMs

The Generalized Linear Models (GLMs) are an extension of Ordinary Linear Regression (OLR) models. In OLR, the dependent variable μ is a linear function of the independent variables; in contrast, GLMs relate a function of the dependent variable, $g(\mu)$, to the independent variables in a linear fashion. The function $g(\mu)$, known as the link function, is a monotonous function. The dependent variable can follow any Probability Distribution Function (PDF) from the Exponential Family, such as Normal, Gamma, or Poisson distributions (DOBSON; BARNETT, 2018; FARAWAY, 2006; JOSHI *et al.*, 2024). In this work, μ represents a probability p.

The response variables are represented by a set of binary values $Y = \{Y_1, Y_2, \ldots, Y_N\}$, where each element indicates the state of the ionosphere (*regular* or *irregular*) at a given time. These values are independent and identically distributed, governed by a Bernoulli PDF:

$$Y|\mathbf{X} \sim \text{Bernoulli}(p), \tag{3.17}$$

where Y is “1” if ROTI ≥ 0.5 and “0” otherwise, $\boldsymbol{X}$ are the explanatory variables and p is the probability of success.

The probability p of observing an irregularity is modeled as a function of the independent variables $\mathbf{X}^i = [1, X^i_{F_{10.7}r}, X^i_{\text{EASr}}, X^i_{\text{TLSr}}, X^i_{K_p}]^T$, typically using a sigmoid function:

$$p_i = E(Y_i|\mathbf{X}^i) = \frac{1}{1 + e^{-\beta \mathbf{X}^i}} \ , \tag{3.18}$$

where $\boldsymbol{\beta} = [\beta_0, \beta_1, \ldots, \beta_M]$ is a vector of parameters. This can be expressed as:

$$\boldsymbol{\beta}\mathbf{X}^i = \ln\left(\frac{p_i}{1 - p_i}\right) = \text{logit}(p_i) = g(p_i). \tag{3.19}$$

Here, $\frac{p_i}{1-p_i}$ is the *odds ratio*, indicating how many times success is more likely than failure. Equation 3.19 explicitly shows the linear relationship between $g(p_i)$ and $\mathbf{X}^i$.

In the context of GLMs with a Bernoulli distribution, the link function establishes the relationship between the linear predictor $g(p)$ and the mean of the response variable p, which represents the probability of success. Since probabilities must lie within the range $[0, 1]$, the link function must map the real line $\mathbb{R}$ to this interval (MCCULLOCH; SEARLE, 2001; FARAWAY, 2006; MYERS *et al.*, 2010; DOBSON; BARNETT, 2018).

The following characteristics are required for the link function in a Bernoulli GLM (MCCULLOCH; SEARLE, 2001; FARAWAY, 2006; MYERS *et al.*, 2010; DOBSON; BARNETT, 2018):

- **Monotonicity**: The function must be monotonic, ensuring a one-to-one relationship between the linear predictor $g(p)$ and the response probability p;
- **Valid Mapping**: It must map all real values of $g(p)$ (from $-\infty$ to $+\infty$) to probabilities in $[0, 1]$; and
- **Interpretability**: The chosen link function should align with the theoretical or practical context of the data, enhancing interpretability.

While the *logit* function is commonly used, other link functions can also be employed, including *probit*, *complement log-log* and *cauchit* (JOHNSON *et al.*, 1995; MCCULLOCH; SEARLE, 2001; MYERS *et al.*, 2010; R Core Team, 2020):

$$\begin{aligned} g(p) &= \Phi^{-1}(p), \qquad (3.20)\\ g(p) &= \ln[-\ln(1-p)], \qquad (3.21)\\ g(p) &= \tan\left(\pi p + \frac{\pi}{2}\right). \qquad (3.22) \end{aligned}$$

Some phenomena may be better represented by considering interactions between explanatory variables. These interaction terms are denoted by a colon (":") and are expressed as products of the variables, for example:

$$X_{\mathrm{EASr}_i} : X_{\mathrm{TLSr}_i} \equiv X_{\mathrm{EASr}_i} \cdot X_{\mathrm{TLSr}_i} \ .$$

A two-variable GLM with interaction can be represented as:

$$g(p) = \beta_0 + \beta_1 X_1 + \beta_2 X_2 + \beta_{1:2} X_1 : X_2 \equiv X_1 * X_2, \qquad (3.23)$$

where $*$ indicates all possible combinations of variables X_1 and X_2. If X_2 is binary, like K_p, this can be expressed as:

$$g(p) = \begin{cases} \beta_0 + \beta_1 X_1, & \text{if } X_2 = 0,\\ (\beta_0 + \beta_2) + (\beta_1 + \beta_{1:2}) X_1, & \text{if } X_2 = 1. \end{cases} \qquad (3.24)$$

The Maximum Likelihood Method can be applied to estimate the optimal $\boldsymbol{\beta}$ for a given set of dependent Y and independent $\mathbf{X}$ variables. In this work, the *Iteratively Reweighted Least Squares* (IWLS) method was used for parameter estimation, evaluated in *R* using an available package (DOBSON; BARNETT, 2018; R Core Team, 2020).

In this study, the software *R* (version 3.6.3) was used for statistical analysis and modeling. *R* is an open-source programming language widely utilized for data analysis, statistical computing, and graphical visualization (FARAWAY, 2006; DOBSON; BARNETT, 2018; R Core Team, 2020). Several packages within *R* were employed to implement the GLMs and evaluate their performance as, for example, the function `glm()` form the `stats` package. Additionally, the `pROC` package was used to calculate and visualize Receiver Operating Characteristic (ROC) curves and the Area Under the Curve (AUC) to assess the model's performance. The `caret` package facilitated cross-validation and model selection through its functions for partitioning data and evaluating prediction accuracy. Both AUC-ROC and the cross-validation are explained in the next section.

3.2.4 Confusion Matrix

The quality of the results was evaluated using a *confusion matrix*, which is a 2 × 2 matrix where each element corresponds to one of the following quantities: TN (true negative), FN (false negative), FP (false positive) and TP (true positive) (LARNER, 2021). These statistics not only indicate the model's performance but also assist in selecting the optimal model. A representation of the confusion matrix is shown in Figure 3.5. The quantities are defined as follows:

- TN: The count of cases where both the predicted and reference ionospheric conditions are classified as *regular*;
- TP: The count of cases where both the predicted and reference ionospheric conditions are classified as *irregular*;
- FN: The count of cases where the predicted ionospheric condition is classified as *regular*, but the reference is *irregular*; and
- FP: The count of cases where the predicted ionospheric condition is classified as *irregular*, but the reference is *regular.*

To construct the confusion matrix, a set of predicted and known ionospheric conditions (*regular* or *irregular*) is required. In this study, 70% of the data was randomly selected for model calibration, while the remaining 30% was used for testing (PEñA; TSAY, 2021; JOSHI *et al.*, 2024). The confusion matrix was computed and the associated statistics were evaluated for each model version. Intuitively, the goal is to maximize true positive (TP) and true negative (TN) rates. However, achieving exact matches for all cases is rarely feasible, necessitating the establishment of performance metrics to compare models. In this study, we selected three key metrics: the False Positive Rate (FPR), the False Negative Rate (FNR) and the Area Under the ROC Curve ($AUC - ROC$), where ROC stands for Receiver Operating Characteristic (HANLEY; MCNEIL, 1982; HAIR *et al.*, 2006; LARNER, 2021; JOSHI *et al.*, 2024).

The FPR quantifies the rate at which the ionosphere is classified as *irregular* when it is actually *regular.* It is defined as

$$FPR = \frac{FP}{FP + TN} \ , \tag{3.25}$$

where its complement is referred to as *Specificity.* This quantity should be minimized; however, an alert system can tolerate a certain level of $FPR.$ While a high False Alarm Rate may incur costs, it does not necessarily reduce the alert system's effectiveness, provided that positive alerts are consistently taken seriously.

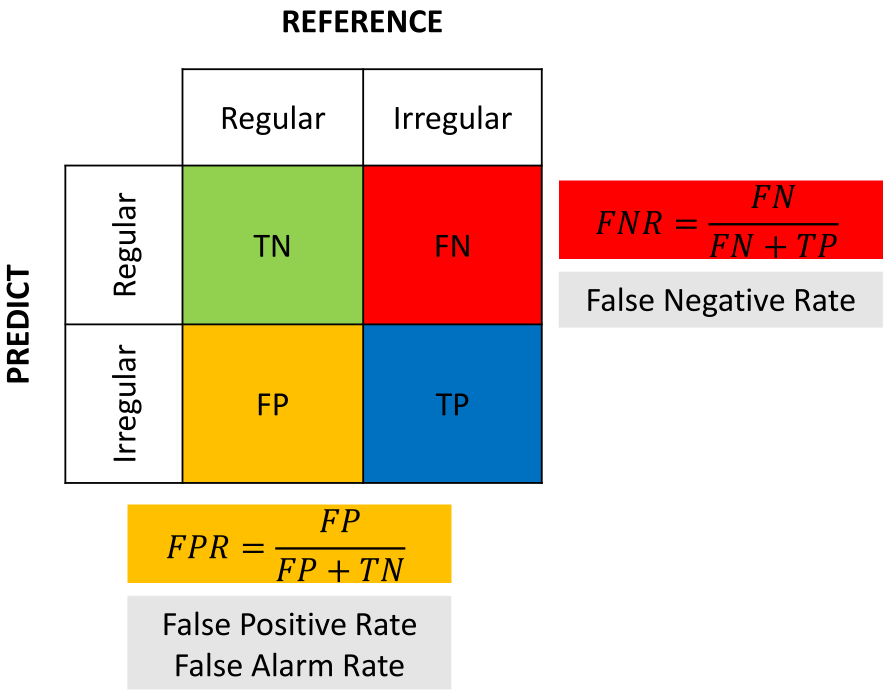

FIGURE 3.5 – Schematic representation of confusion matrix.

The FNR quantifies the rate at which the ionosphere is classified as *regular* when it is actually *irregular*. It is defined as

$$FNR = \frac{FN}{FN + TP} \ , \tag{3.26}$$

with its complement being *Sensitivity*. This metric should be kept as low as possible, as alert systems typically cannot tolerate high FNR values. A compromise between FNR and FPR is often necessary and designing a model that yields low values for both can be challenging. Therefore, the best model is chosen among those that achieve a prescribed low level of FNR while maintaining the lowest possible FPR.

The $AUC - ROC$ measures the effectiveness of a classification model in distinguishing between positive and negative examples. It is defined as the area under the curve representing *Sensitivity* $(1 - FNR)$ versus FPR, with values ranging from 0 to 1. Some authors, as cited by Laner (2021) and in a recent paper (JOSHI *et al.*, 2024), suggest that good models achieve an $AUC - ROC$ greater than 0.70.

Another relevant figure of merit is the $Inaccuracy$ (In), which represents the overall error rate, defined as the ratio of all erroneous classifications to all predictions (LARNER, 2021):

$$In = \frac{FN + FP}{T} \ , \tag{3.27}$$

where $T = TN+FP+FN+TP$. In this work, it is observed that $FP \gg FN$ and $TN \gg TP$, as *irregular* events are relatively rare compared to the total dataset. Consequently, In and FPR are often indistinguishable, given that

$$In = \frac{FN + FP}{TN + FP + FN + TP} \approx \frac{FP}{FP + TN} = FPR \; . \tag{3.28}$$

For this reason, the In statistic was not used in our analysis; instead, the FPR was used to evaluate the error performance.

4 Results and Discussions

4.1 Gravity Waves

4.1.1 Wind Profiles

The temporal averages of the zonal and meridional components wind height profiles were computed for each location, for each atmospheric layer and for each season, i.e., the dry and wet seasons, which were defined earlier. The temporal mean of the profiles give us a measure of the prevailing winds. The zonal winds are stronger than the meridional winds (PALMÉN *et al.*, 1969) and hence are easier to differentiate - compare the winds profiles in Figures 4.1 and 4.2.

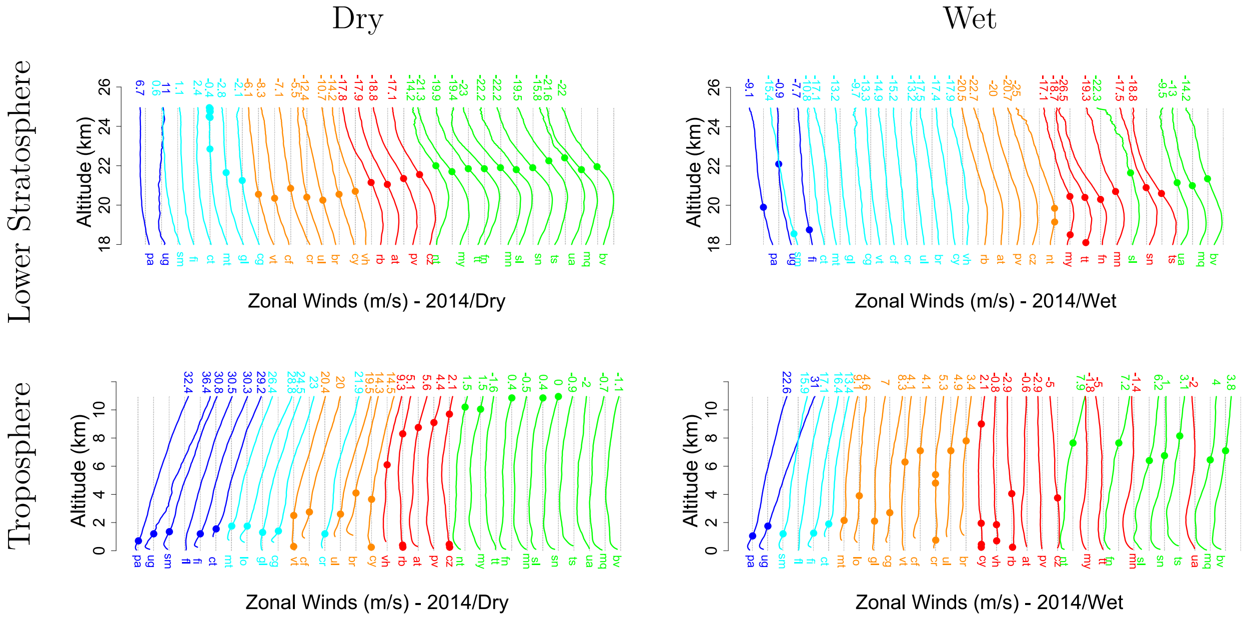

FIGURE 4.1 – Temporal averages of the zonal wind height profiles for each aerodrome (where in the bottom, for example, *bv* is equivalent to *sbbv*) during the dry (left) and wet (right) periods. The profiles are presented for the troposphere (bottom) and lower stratosphere (top). The profiles are grouped by similarities among zonal winds into five clusters, each represented by a different color. The vertical dashed lines represent a wind speed of 10 m/s, the top-colored numbers are the velocity at the last altitude in each layer, and the colored points indicate where the direction of zonal wind changes.

The five clusters of from zonal winds height profiles (see Figure 4.1) were labeled by colors red (R), green (G), orange (O), cyan (C) and blue (B) and are also represented in the geographic map in Figure 4.3, showing that the profiles cluster according to latitude range.

The hodographs in Figure 4.4 show the behavior of the prevailing winds in the grouped samples, facilitating the comparison between the wind profiles and the identification of similarities among samples of the same group.

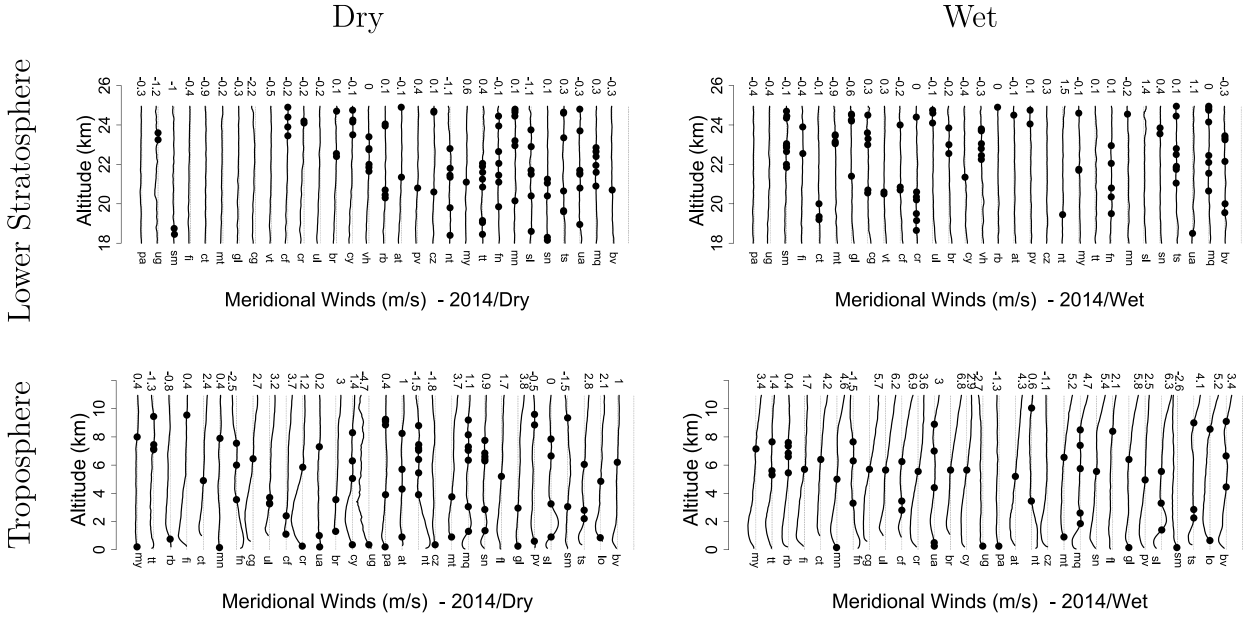

FIGURE 4.2 – The same of Figure 4.1, but applied for meridional winds.

The cluster analysis have shown that wind profiles located in the same latitude range usually have similar features. This was expected since the atmospheric circulation cells and geostrophic flow have a strong latitudinal dependence. The wind profiles (Figure 4.1 and 4.3 and the hodographs in Figure 4.4) have shown that clusters R and G, near the equator, have similar features. The clusters C, B and O, in the south, also have similar features, but they differ significantly from clusters R and G, located near the equator. Besides the differences in the wind profiles due to latitude, there is also some significant seasonal dependence. These differences in the seasonality of winds are important because they can influence the vertical wavelength of the GWs (AYORINDE *et al.*, 2023). In what follows, these differences are discussed in more detail.

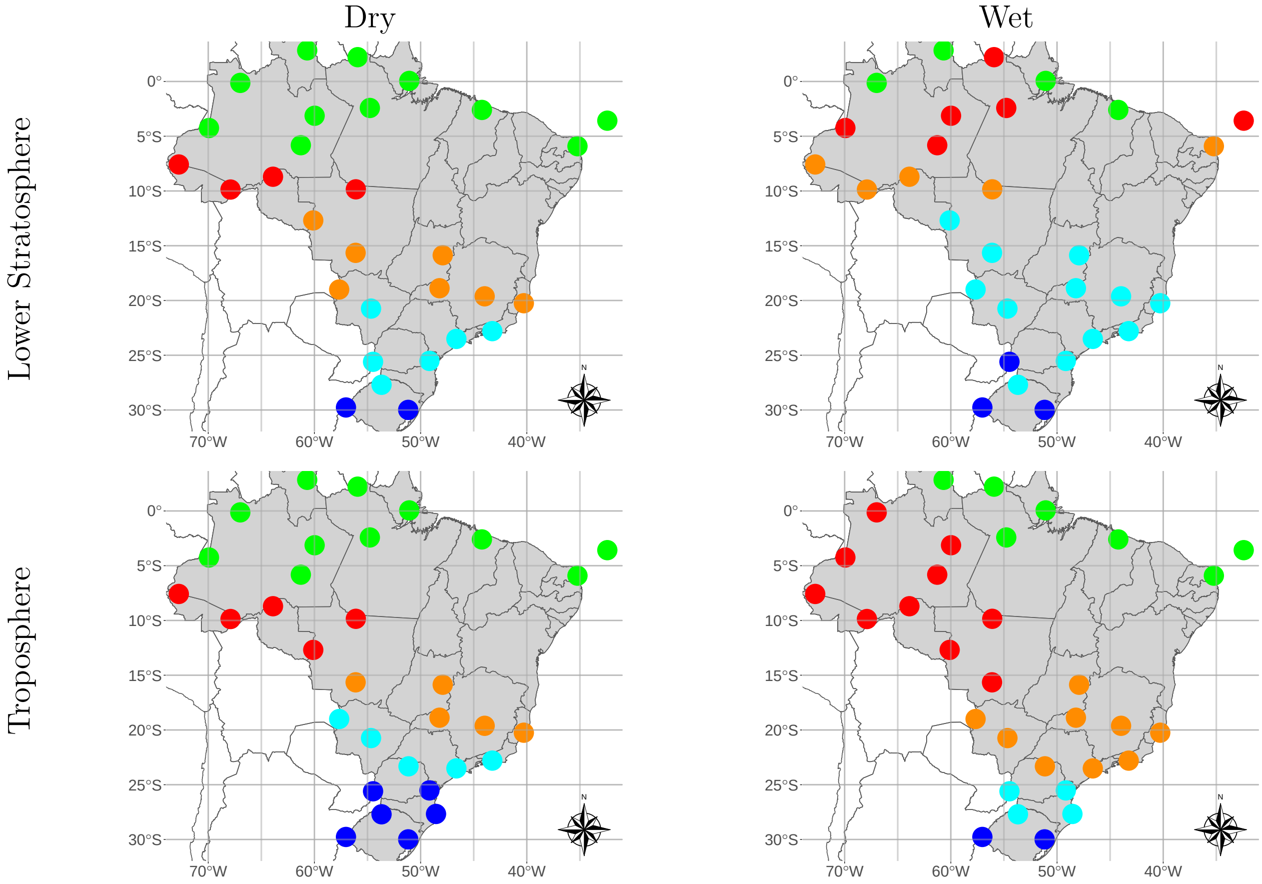

FIGURE 4.3 – The points locate the aerodrome position on the map while the color indicates to which cluster it belongs according to the atmosphere layer (troposphere on bottom; lower stratosphere on top) and season (dry on left; wet on right). The zonal winds was the variable on which the cluster analysis was performed (BRHIAN *et al.*, 2024).

In the studied region encompassing most of the Brazilian territory, the prevailing winds near the Earth's surface are characterized by weak easterlies. These winds are weak due to attenuation in the fluid boundary layer (AHRENS; HENSON, 2018; LU; VECCHI, 2015). As altitude increases up to the tropopause, the winds get increasingly eastward, achieving the highest speeds in the subtropical regions in the winter. In the tropical/subtropical regions, it is also possible to identify weak northward winds near the surface that reverts southward as the altitude increases, characterizing the so called Hadley cell, a convective roll located between the equator and the tropics where the winds next to the ground converge to the ITCZ. Also, the comparison between the tropospheric wind profiles in the dry season with the wind profiles in the wet season shows, for each cluster, an increase in the average magnitude of the eastward winds at the top of the troposphere. As it will be seen later, the kinetic energy of GWs in the troposphere are higher in the dry months, which is probably a result of these stronger winds observed in tropical/subtropical locations.

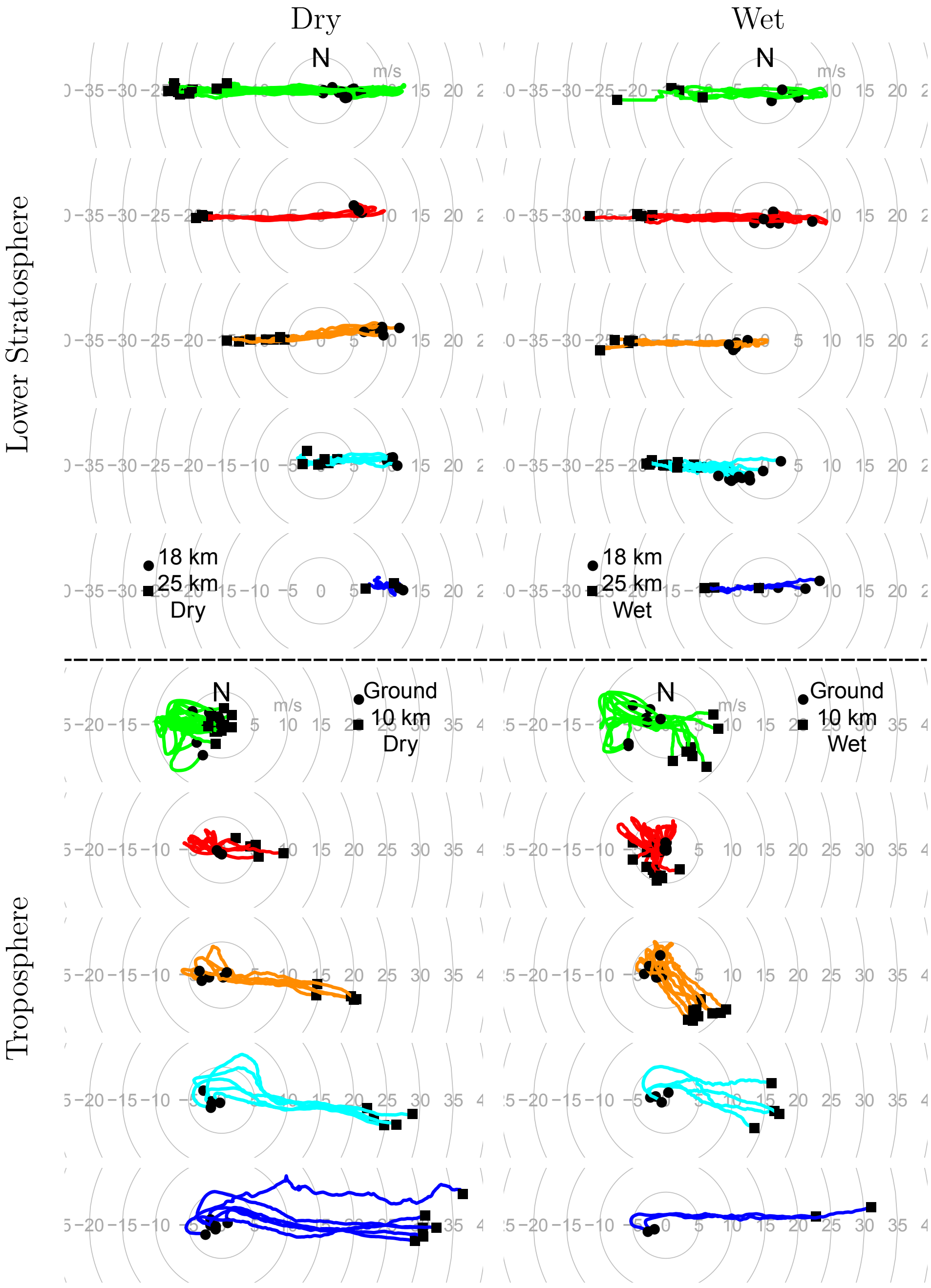

FIGURE 4.4 – Hodographs grouped according to the cluster analysis of the zonal winds in the lower stratosphere and troposphere in 2014 and presented in Figure 4.3. The left panels refer to the dry season, while the right panels refer to the wet period. The top panels refer to lower stratosphere layer and the bottom one refer to troposphere layer. The positive horizontal axis correspond to westerlies (eastward winds) while the positive vertical axis correspond to southerlies (northward winds) (BRHIAN *et al.*, 2024).

The example hodograph presented in Figure 3.3, discussed earlier in Section 2, shows that very intense winds occur in the tropopause. The hodograph shows a jet stream with wind magnitudes reaching up to 70 m/s in the latitude region between -20° and -30°, where the encounter between the Hadley cell and the Ferrel cell is expected (PALMÉN *et al.*, 1969; AYORINDE *et al.*, 2023). As it will be seen later, the turbulence and the high convection speeds in the tropopause may explain the uncoupling between GWs in the troposphere and the low stratosphere. GWs that propagate into this perturbed intermediate layer tend to be absorbed or destroyed in this turbulence region (AHRENS; HENSON, 2018; ARCHER; CALDEIRA, 2008; FRITTS; ALEXANDER, 2003; MASTRANTONIO *et al.*, 1976; ROSSBY; WILLET, 1948; YIGIT, 2015).

The wind profiles were analysed in the altitude range between 18 km and 25 km to study the lower stratosphere (Figure 4.4). The way the samples grouped into clusters was similar to the troposphere case, i.e., the zonal winds grouped according to latitude (GELLER; GONG, 2010; VINCENT *et al.*, 1997). The hodographs in Figure 4.4 show that the winds near 18 km tended to be eastward and the winds at higher altitudes tended to be westward. The change of direction in the winds in the lower stratosphere occurred at higher altitudes in the dry period. The magnitude of the winds near the equator at 25 km altitude was stronger than the magnitude of the winds in middle latitudes at the same altitude.

4.1.2 Brazilian GWs in the Lower Atmosphere

As in the case of the study of the wind profiles, here the analysis was split according to the atmospheric layer (troposphere/lower stratosphere) and the season (dry/wet). For each condition and each aerodrome (see Appendix A), the distributions of the kinetic and potential energy densities were studied by fitting the corresponding histograms to the gamma and normal distributions, see Figure 4.5 and 4.6. In the end, we calculate the average and standard deviations of each fitting parameter, shown in Table 4.1, to understand how much the values of energy increase or decrease, as well as to understand how dispersed the values are. During the dry season, mechanical energy in the lower atmosphere is generally higher than during the wet season, likely because thermal driving plays a more significant role compared to eddy-driven processes. In contrast, during the wet season, eddy-driven processes dominate over thermal driving, resulting in lower mechanical energy (KANG; LU, 2012; HOSKINS; YANG, 2023). We also note that, in general, the distribution of the energies did not depend on the time of the day when it was collected, whether it was dusk or dawn, see the Figures A.1 and A.2. The adherence test of Kolmogorov-Smirnov was used to test the adherence of the fitted distribution to the data. The p-values computed for the gamma distribution fittings have shown, with a level of significance of 5%, that the null hypothesis (H_0: the tested distribution is the data distribution) could not be rejected. In other words, the gamma distribution provided good fits for the distributions of both kinetic and potential energy densities.

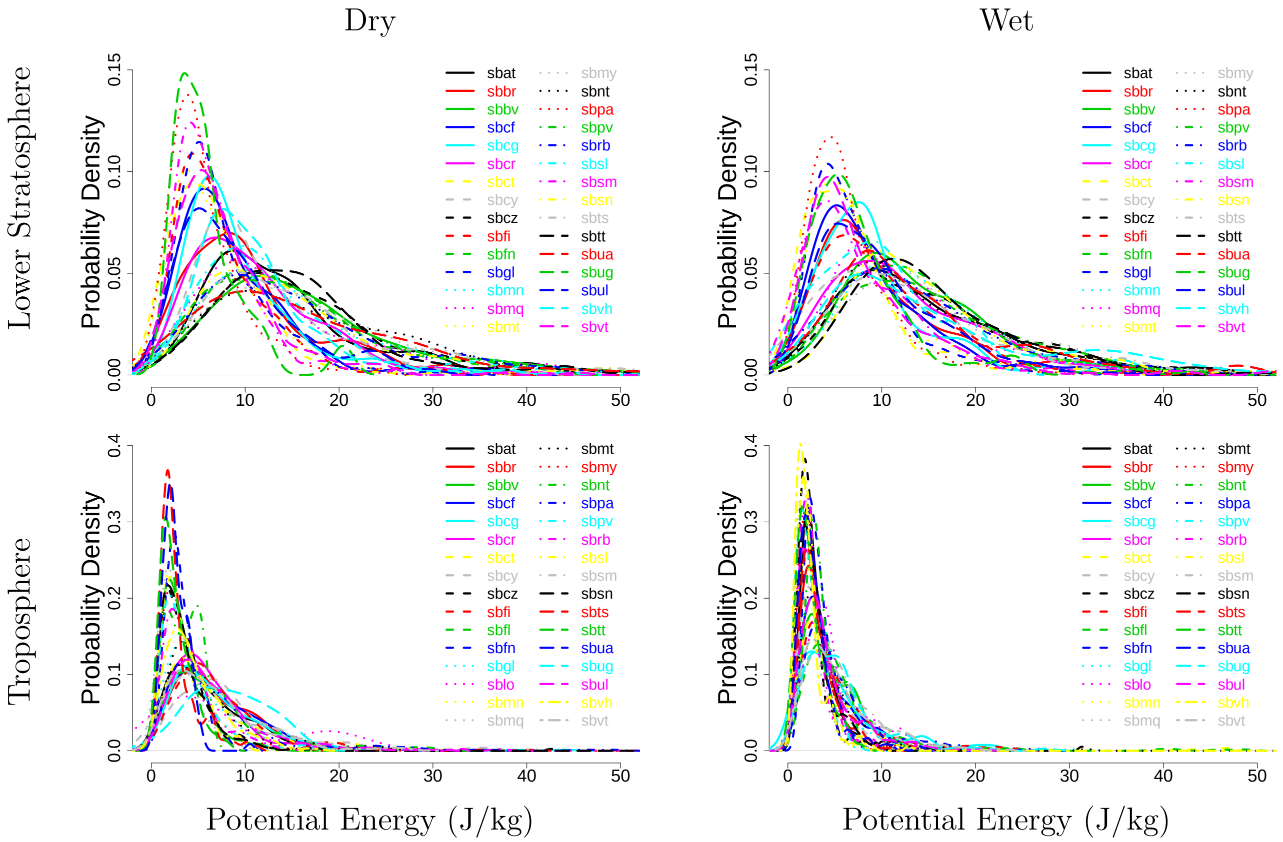

FIGURE 4.5 – Probability Density estimation of potential energy (J/kg) from each aerodrome during the dry and wet season in 2014 from the troposphere and lower stratosphere layer. Note that the shape of the probability density can be modeled as a Gamma distribution. The adjustment of Gamma distribution for the values from other energies and layers was estimated and organized in Appendix A and summarized in Table 4.1.

The fitting parameters show that the energy densities in the lower stratosphere were typically greater than the energy densities in the troposphere, possibly due to the fact that the increase in the magnitude of perturbations (u', v', T') is associated with the decrease in the density with increasing altitude. Besides, the energy densities in the dry season are typically greater than the energy densities in the wet season (NAPPO, 2013; VINCENT *et al.*, 1997). We also note that the fitted gamma distribution is right-skewed. Its deviation from normality justifies the use of robust statistical estimators (e.g. using median instead of average) to study the typical time trend of the energy densities.

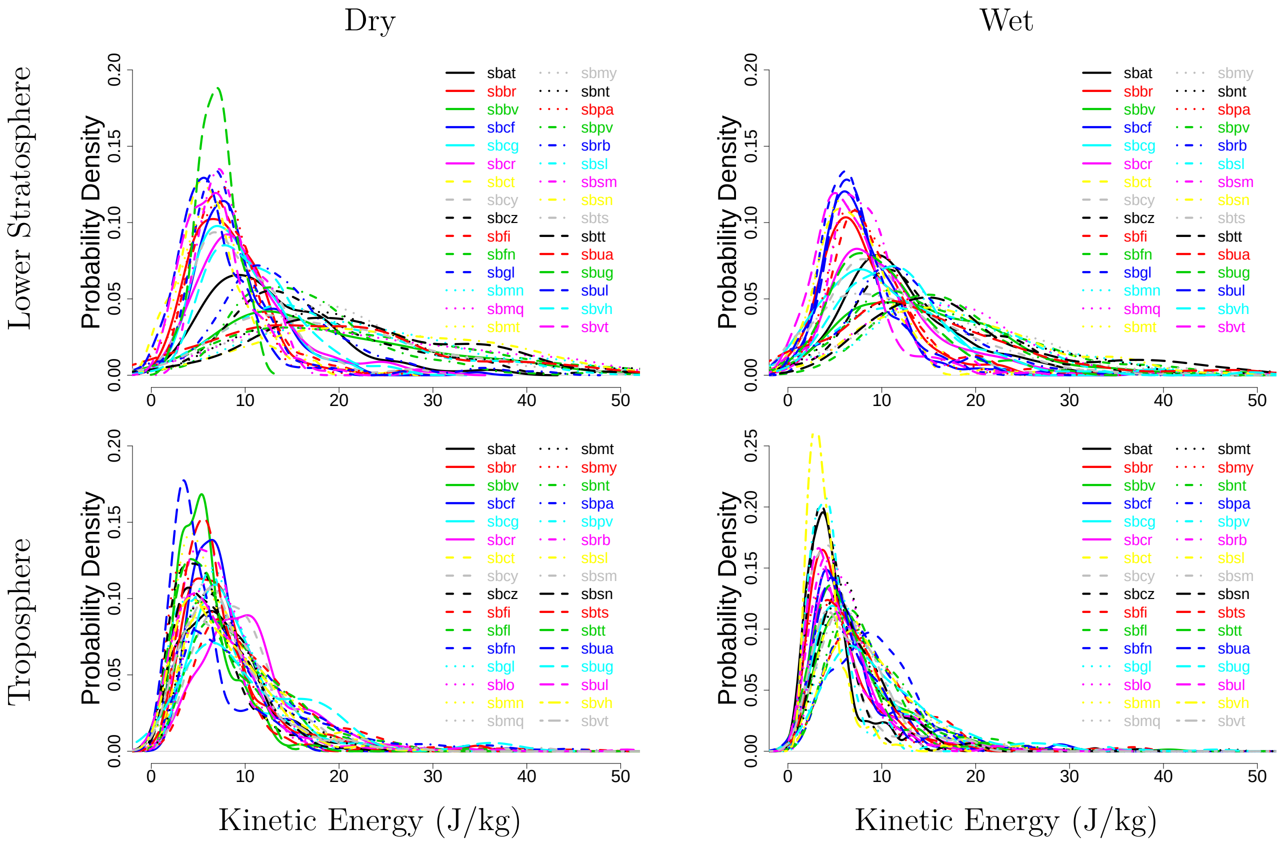

FIGURE 4.6 – The same of Figure 4.5, but considering kinetic energy.

In Figure 4.7 we show the time series of the energy densities in 2014 for the troposphere and the lower stratosphere. The lines in gray are the moving median ($h = 15$) for each aerodrome, the black line is the average over all aerodromes and the red lines are the envelopes formed by the addition and subtraction of one standard deviation about the average. The energy densities in the lower stratosphere had a greater dispersion than the energy densities in the troposphere. Also, the average values in the lower stratosphere were around 50% higher than the values in the troposphere. This observation is consistent with the expected increase of the wave amplitudes as a function of altitude, as explained before.

The energy densities in the troposphere were greater in the winter, late autumn and early spring, a behavior that was also observed in other studies (ALLEN; VINCENT, 1995; GELLER; GONG, 2010) and likely explained by the eddy driving to be more dominant during the wet season (KANG; LU, 2012; HOSKINS; YANG, 2023). A study using radiosonde measurements of temperature in the Australian sector (12°-68°S,78°-159°E) from June 1991 to May 1992 (ALLEN; VINCENT, 1995) reported larger values in the potential energy densities in the period from July to October (ALLEN; VINCENT, 1995). Another work by Geller and Gong (2010), based on radiosonde measurements from many stations in the US, covering the sector (~5°-70°N) from January 1998 to December 2006, found that the maximum values of kinetic and potential energy densities occurred during the winter period, as our results. The authors also reported that the energy density values had latitudinal dependency, with greater values occurring close to 35°N.

TABLE 4.1 – Average values, computed over the 32 aerodromes, of the parameters of the gamma and normal distributions of the energy densities. The values are separated by atmospheric layer, troposphere (T) and lower stratosphere (S), and period, dry and wet. We used the Kolmogorov-Smirnov's adherence test with 5 % of significance level and all the fittings passed the test. The values a ± b represents the average ± standard deviation.

		Kinetic		**Potencial**	
		Dry	**Wet**	**Dry**	**Wet**
GAMMA	**S**	3.5±1.8	2.6±0.7	2.2±0.4	1.9±0.4
		(4.9±3.3)	(5.1±2.5)	(5.8±2.4)	(6.2±1.5)
shape[adimensional]	**T**	3.2±0.8	3.3±0.7	2.2±0.6	2.5±0.8
(scale[J/kg])		(2.8±1.1)	(2.3±0.8)	(2.7±1.2)	(1.7±0.8)
NORMAL	**S**	14.1±6.5	12.3±4.0	12.4±4.2	12.1±3.0
		(7.6±4.0)	(7.1±2.5)	(9.1±3.6)	(8.8±1.9)
mean[J/kg]	**T**	8.3±1.6	7.3±1.6	5.4±1.8	3.8±1.1
(sd[J/kg])		(6.8±4.9)	(5.4±2.9)	(4.9±4.0)	(3.1±1.5)

In the lower stratosphere case there was a slight increase in the kinetic energy density in the same period (ALEXANDER *et al.*, 2010; ALLEN; VINCENT, 1995; GELLER; GONG, 2010), but no clear trend in the potential energy density. Other work published by Ayorinde et. al. (2023), by using COSMIC-2 and METOP radio occultation measurements during 2020 e 2021, found higher values in the potential energy in the lower stratosphere near the equator (±10°) during the fall station. A study by Ayorinde et. al. (2024), utilizing radio occultation and analyzing 20 years of data, reveals that GWs predominantly influence the tropical region (±20°) at altitudes of 20-30 km, an area characterized by intense deep convective activities. Besides, they showed during this period that GWs in the lower stratosphere are influenced by 11-annual, biannual, anual, and semianual variation. Geller and Gong (2010) observed maximum values of kinetic and potential energy densities during the winter, and Moffat-Griffin et. al. (2011), with a study with radiosondes in the small islands near 60° S of latitude, highlighted that in this region is likely a huge source of GWs. However, the reasons for the sources of the GWs in this region have likely not been well determined. They also reported that the kinetic energy density maximum values were observed close to 35 °N, while the potential energy density maximum values were observed at equatorial latitudes. We also highlight that, in our results, the kinetic energy density in the lower stratosphere was typically greater than the potential energy density. This result agrees with the findings of a previous work by Vincent and Alexander (2000), which used radiosonde data, covering a period of six years, to determine the kinetic and potential energy densities over the Indian Ocean (12°S,97°E) in the lower stratosphere.

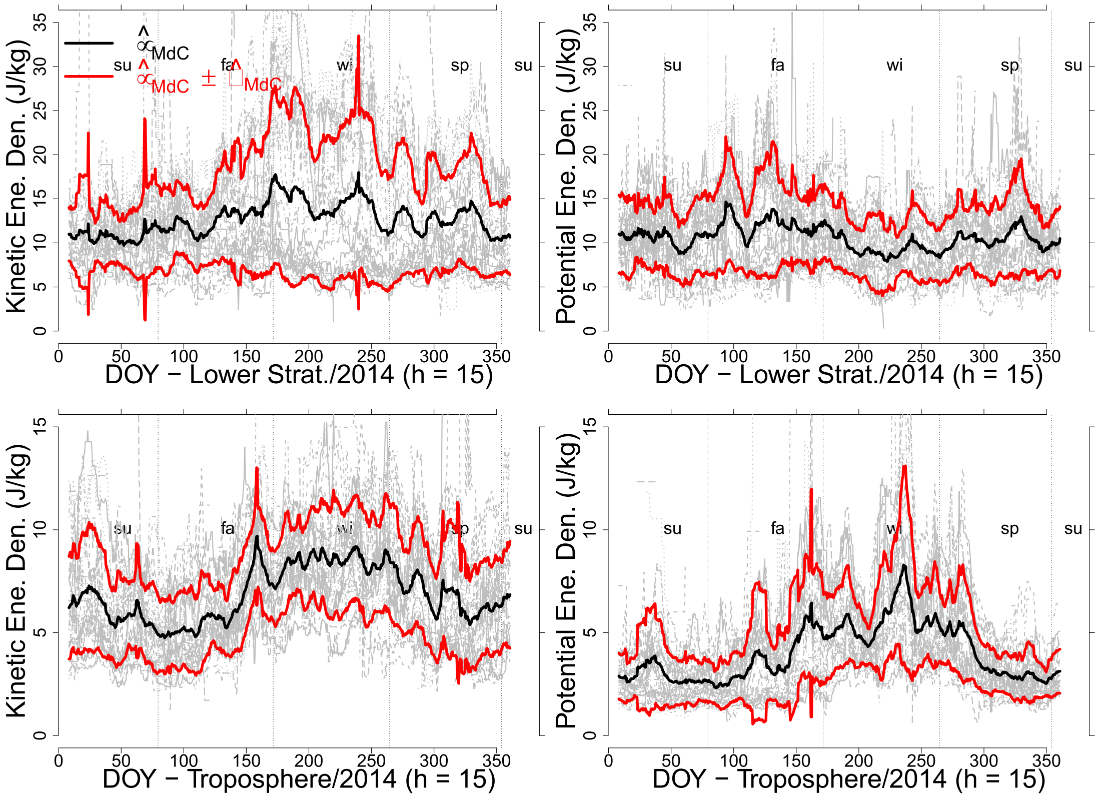

FIGURE 4.7 – The lines in gray are the moving median (h = 15) for each aerodrome, the black line is the average of the medians ($\hat{\mu}_{MdC}$) over the aerodromes and the red lines are the envelopes formed by the addition and the subtraction of one standard deviation about the average ($\hat{\sigma}_{MdC}$). The kinetic energy and potential energy densities in the lower stratosphere are shown on the two plots on the top, while the same quantities in the troposphere are shown in the two plots on the bottom (BRHIAN *et al.*, 2024).

The thickness of the envelopes (red curves in Figure 4.7) was smaller in the troposphere, for both kinetic and potential energy densities. These results show that either the variability of the energies are amplified in the transition from the troposphere to the lower stratosphere or the variability is produced in the lower stratosphere itself from perturbing processes that are not related to the state of the troposphere below 12 km. The results also show that the volatility of the potential energy density in the lower stratosphere was greater in the dry period, a behavior that was also found in measurements from Australia (ALLEN; VINCENT, 1995).

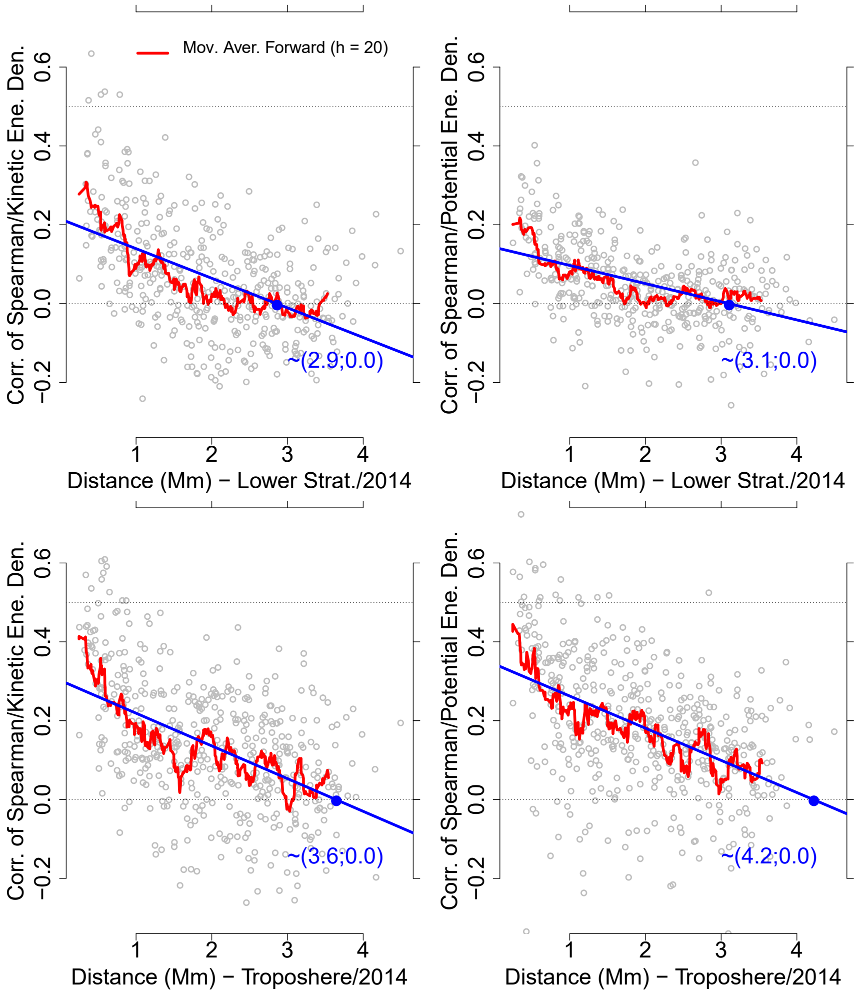

FIGURE 4.8 – Spearman's correlation coefficient between the kinetic energy (left) and potential energy (right) densities from the total pairwise combinations of aerodromes as a function of the pair distance in the troposphere (bottom) and lower stratosphere (top). The red line is the forward moving average with h = 20 and the blue line is the fitted straight line. The x-axis intercept gives an estimate of the decorrelation distance where 1 Mn = 1,000 km (see text) (BRHIAN *et al.*, 2024).

The spatial correlation between the energy densities of each aerodrome was computed from the total pairwise combinations of aerodromes $\binom{32}{2} = 496$. The correlation coefficient (Spearman's coefficient) for each pairwise combination is plotted against their distances in Figure 4.8. From this analysis, it is possible to compute the typical decorrelation distance, i.e., the distance below which GW energy densities are still spatially correlated. Our analysis showed that the decorrelation distance is approximately 3,000 km (central angle $\sim 27°$) in the troposphere and approximately 3,900 km (central angle $\sim 35°$) in the lower stratosphere, as shown in Figure 4.8. Here, the central angle is defined as the arc angle with vertex in the geographic center of the Earth, containing the arc distance. In all cases, the correlation coefficient is typically positive. The hypothesis of constant and null correlation coefficient was tested using the F-test, resulting in a p-values that were virtually zero (large negative power of 10). These results indicate that the loss of correlation between the energies occurs at the same scale as the horizontal wavelength of the GWs shown in Figure 4.15, demonstrating the area of influence of each GW.

These observations may be explained as follows. The strong perturbations in the troposphere/stratosphere that generate GWs locally will disperse following a nonlinear process, producing a wave train. This wave train should extend throughout a volume, so measurements at close aerodromes are more likely to measure similar energy densities. This explains the spatial correlation in the energy densities in the same atmospheric layer, and may be used to infer the sources and sinks of energy from a GW.

We also computed the correlation between the energy densities at different atmospheric layers, comparing pair by pair measurements from all aerodromes, including the same aerodrome (Figure 4.9). If GWs propagating through the troposphere reaches the lower stratosphere, the correlation coefficients are expected to be non-null and positive for nearby aerodromes. What we observed was that the average value of the correlation coefficients was close to zero in all cases. The histogram of Spearman's correlation coefficient of all aerodromes is shown in Figure 4.9.

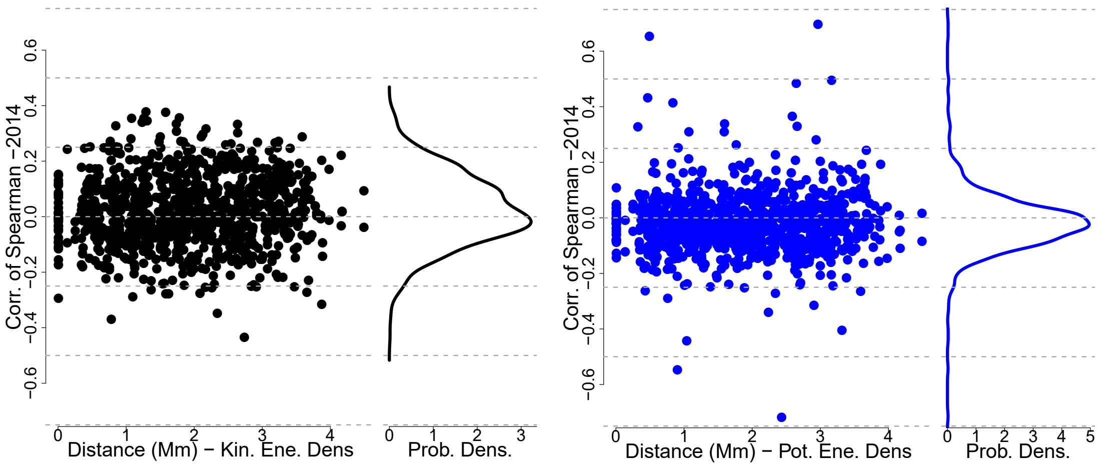

FIGURE 4.9 – Left: Spearman correlation coefficients computed taking the pair of variables kinetic energy density in lower stratosphere (S) and kinetic energy density in troposphere (T) as a function of distance between aerodromes. Right: the same for potential energy density. All the available data in the year of 2014 was considered in the plot. The plots in the right side show the resulting distribution from the plane projection along the distance axis (BRHIAN *et al.*, 2024).

The absence of correlation between measurements at different atmospheric layers may indicate that typically GWs propagating through the troposphere below 12 km are not the cause of GWs propagating through the lower stratosphere (ALLEN; VINCENT, 1995; GELLER; GONG, 2010). However, sporadic events should not be ruled out, such as tropospheric deep cloud convection, because it can directly reach and perturb the lower stratosphere (SIVAKANDAN *et al.*, 2019; TAKAHASHI *et al.*, 2020), or any other strong and large scale perturbation having its origin in the troposphere, which may not be detected by radiosondes due to the filtering effect (see the Caveats subsection 4.1.6).

In other geographic locations, characterized by mountainous relief with high peaks, GWs perturbations can propagate to the lower stratosphere under certain circumstances (HEALE *et al.*, 2020), but such topographical profiles are simply absent in the Brazilian territory. The mountain formations in the Brazilian southeast rarely exceeds 2 km, so the GWs generated by orographic forcing is less likely to extend into the lower stratosphere. The higher energy densities observed in the dry seasons suggest that effects related to winds only, such as shear instabilities, frontal systems and geostrophic adjustment, play a more important role on generating GWs in the troposphere. We do not rule out deep convection, especially in the wet season. However, usually, balloons are not launched in bad weather conditions associated with deep convection, so our data may have a selection bias for this type of phenomenon.

We should also consider another hypothesis for not observing correlation in energy densities in different layers. GWs group velocities have a slightly upward tilt, so wave packets generated at low altitudes may reach the lower stratosphere much later and hundreds or thousands kilometers way (horizontally) from the region it was generated within the troposphere. This hypothesis seems to be consistent with the results found by Yoo et al. (2018), who made an extensive study of GWs using radiosonde data from Jang Bogo Station in Antarctica (74°37'S, 164°13'E). On their first paper (YOO *et al.*, 2018), the authors present the GWs parameters they determined using 3-year radiosonde data, while on their second paper the authors use backward ray tracing calculations to find the sources of GWs observed in the lower stratosphere (YOO *et al.*, 2020). The authors found many sources presumably at the troposphere, but usually hundreds or thousands kilometers away from the observation point. The authors also suggested that the characteristics of GWs could be significantly altered while propagating vertically in a region where the background wind changes substantially, which may be an explanation for why no correlation was observed in our results.

This alternative hypothesis should not be discarded in face of the current knowledge and the results presented here. However, we shall favor the uncoupling hypothesis based on the observation of spatial correlation. If the radius of spatial correlation was around 3×10^3 km in the troposphere and the power spectrum density of the GWs did not change radically while moving from one layer to another as expected by the linear theory, it should have been observed some correlation between measurements at the troposphere and the lower stratosphere.Therefore, we consider it more likely that GWs in troposphere and lower stratosphere are uncoupled or weakly coupled.

Assuming that the weak coupling hypothesis is correct, we may speculate that GWs propagating in the troposphere below 12 km most probably do not reach the lower stratosphere. GWs can break, get absorbed or reflected before reaching the lower stratosphere (NAPPO, 2013), or interact destructively with strong wind streams in the transition region. GWs observed in the lower stratosphere are probably created in the tropopause where winds are subject to more intense shear.

Our conclusion has some support in some findings by other authors (GELLER; GONG, 2010; GONG; GELLER, 2010). Based on radiosonde measurements over the American (US) sector, these authors concluded that there was no indication of any signature of energy maxima in the stratosphere due to convectively forced gravity waves in the summer. Geller and Gong concluded that most likely convectively forced gravity waves in the summer do not propagate up to the lower stratosphere (GELLER; GONG, 2010; GONG; GELLER, 2010). On the other hand, Ayorinde et. al. 2023 found evidence that GWs in the lower stratosphere happens likely due to convective activities. Also, they found little or no evidence of GWs activities in the summer at mid-latitude. Our findings goes beyond that by pointing to the conclusion that GWs observed in the troposphere and the lower stratosphere by radiosonde in the Brazilian region are most likely uncoupled, independently of the season.

In theoretical and experimental fluid dynamics there are many examples of waves being "blocked" by very strong convective flows, such as hydraulic breakwaters (PEREGRINE, 1976). This is a nonlinear process, distinct from the well-known problem of wave absorption in the critical layer caused by winds that make the intrinsic frequency null (VADAS *et al.*, 2003; NAPPO, 2013; TOMIKAWA, 2015). It is likely to assume that besides the critical layer, GWs are stopped by nonlinear process of interaction with strong and turbulent convective flows in the tropopause. But even in the case where only the hypotheses of wave blocking by the critical layer is considered, the probability of GWs being blocked is high due to the strong winds in the higher troposphere and tropopause.

4.1.3 Monochromatic GWs

When counting monochromatic GWs, it must be taken into account the fact that the number of radiosonde launches were not uniform in time. Some months had a larger number of launches than others, as shown in the hot tables in Figures 4.10 and 4.11, where each line is ordered by geographic latitude (the tables only shown aerodromes with more than 2 GWs identified in 2014).

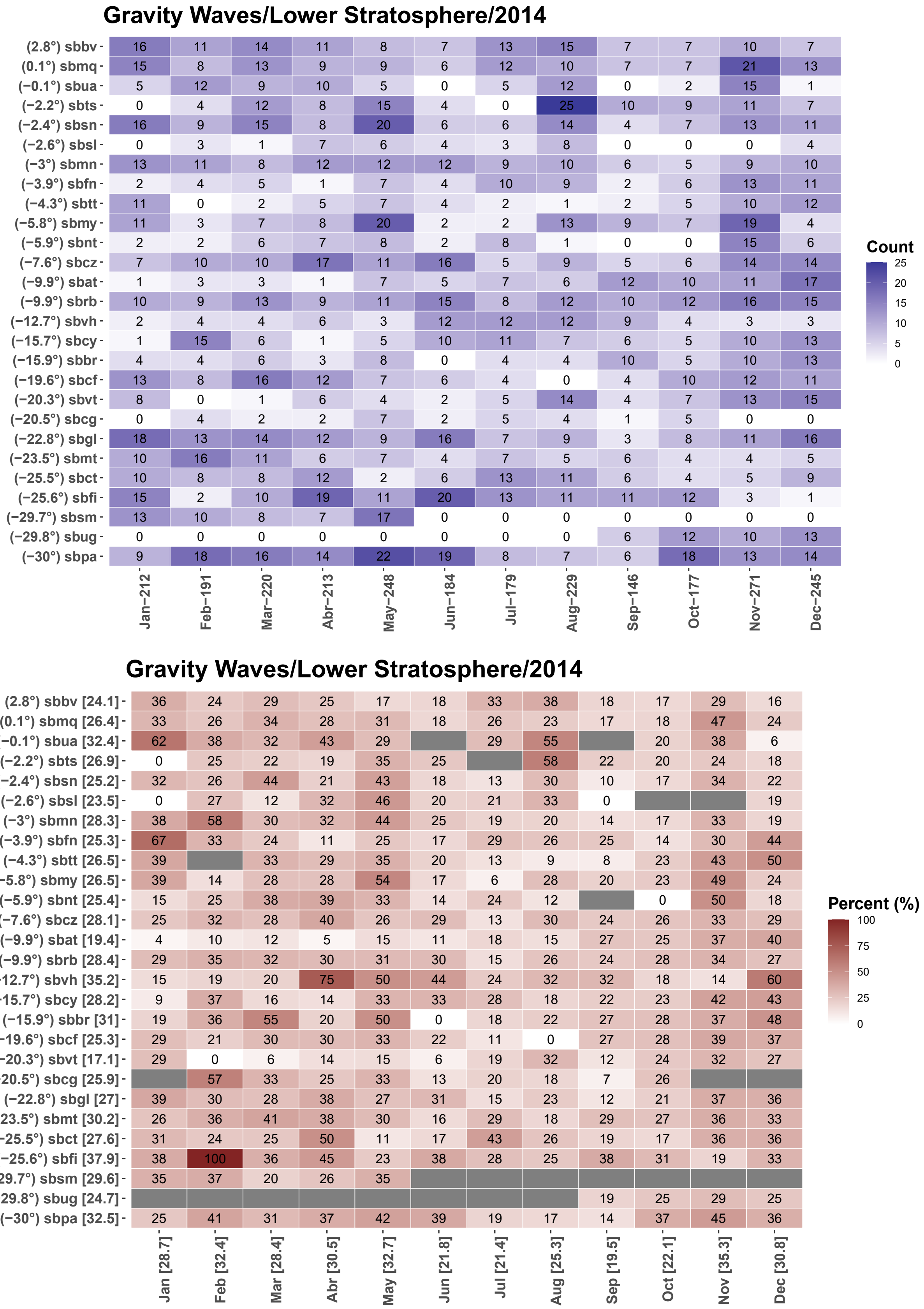

Gravity Waves/Lower Stratosphere/2014

	Jan−212	Feb−191	Mar−220	Abr−213	May−248	Jun−184	Jul−179	Aug−229	Sep−146	Oct−177	Nov−271	Dec−245
(2.8°) sbbv	16	11	14	11	8	7	13	15	7	7	10	7
(0.1°) sbmq	15	8	13	9	9	6	12	10	7	7	21	13
(−0.1°) sbua	5	12	9	10	5	0	5	12	0	2	15	1
(−2.2°) sbts	0	4	12	8	15	4	0	25	10	9	11	7
(−2.4°) sbsn	16	9	15	8	20	6	6	14	4	7	13	11
(−2.6°) sbsl	0	3	1	7	6	4	3	8	0	0	0	4
(−3°) sbmn	13	11	8	12	12	12	9	10	6	5	9	10
(−3.9°) sbfn	2	4	5	1	7	4	10	9	2	6	13	11
(−4.3°) sbtt	11	0	2	5	7	4	2	1	2	5	10	12
(−5.8°) sbmy	11	3	7	8	20	2	2	13	9	7	19	4
(−5.9°) sbnt	2	2	6	7	8	2	8	1	0	0	15	6
(−7.6°) sbcz	7	10	10	17	11	16	5	9	5	6	14	14
(−9.9°) sbat	1	3	3	1	7	5	7	6	12	10	11	17
(−9.9°) sbrb	10	9	13	9	11	15	8	12	10	12	16	15
(−12.7°) sbvh	2	4	4	6	3	12	12	12	9	4	3	3
(−15.7°) sbcy	1	15	6	1	5	10	11	7	6	5	10	13
(−15.9°) sbbr	4	4	6	3	8	0	4	4	10	5	10	13
(−19.6°) sbcf	13	8	16	12	7	6	4	0	4	10	12	11
(−20.3°) sbvt	8	0	1	6	4	2	5	14	4	7	13	15
(−20.5°) sbcg	0	4	2	2	7	2	5	4	1	5	0	0
(−22.8°) sbgl	18	13	14	12	9	16	7	9	3	8	11	16
(−23.5°) sbmt	10	16	11	6	7	4	7	5	6	4	4	5
(−25.5°) sbct	10	8	8	12	2	6	13	11	6	4	5	9
(−25.6°) sbfi	15	2	10	19	11	20	13	11	11	12	3	1
(−29.7°) sbsm	13	10	8	7	17	0	0	0	0	0	0	0
(−29.8°) sbug	0	0	0	0	0	0	0	0	6	12	10	13
(−30°) sbpa	9	18	16	14	22	19	8	7	6	18	13	14

Gravity Waves/Lower Stratosphere/2014

	Jan [28.7]	Feb [32.4]	Mar [28.4]	Abr [30.5]	May [32.7]	Jun [21.8]	Jul [21.4]	Aug [25.3]	Sep [19.5]	Oct [22.1]	Nov [35.3]	Dec [30.8]
(2.8°) sbbv [24.1]	36	24	29	25	17	18	33	38	18	17	29	16
(0.1°) sbmq [26.4]	33	26	34	28	31	18	26	23	17	18	47	24
(−0.1°) sbua [32.4]	62	38	32	43	29		29	55		20	38	6
(−2.2°) sbts [26.9]	0	25	22	19	35	25		58	22	20	24	18
(−2.4°) sbsn [25.2]	32	26	44	21	43	18	13	30	10	17	34	22
(−2.6°) sbsl [23.5]	0	27	12	32	46	20	21	33	0			19
(−3°) sbmn [28.3]	38	58	30	32	44	25	19	20	14	17	33	19
(−3.9°) sbfn [25.3]	67	33	24	11	25	17	29	26	25	14	30	44
(−4.3°) sbtt [26.5]	39		33	29	35	20	13	9	8	23	43	50
(−5.8°) sbmy [26.5]	39	14	28	28	54	17	6	28	20	23	49	24
(−5.9°) sbnt [25.4]	15	25	38	39	33	14	24	12		0	50	18
(−7.6°) sbcz [28.1]	25	32	28	40	26	29	13	30	24	26	33	29
(−9.9°) sbat [19.4]	4	10	12	5	15	11	18	15	27	25	37	40
(−9.9°) sbrb [28.4]	29	35	32	30	31	30	15	26	24	28	34	27
(−12.7°) sbvh [35.2]	15	19	20	75	50	44	24	32	32	18	14	60
(−15.7°) sbcy [28.2]	9	37	16	14	33	33	28	18	22	23	42	43
(−15.9°) sbbr [31]	19	36	55	20	50	0	18	22	27	28	37	48
(−19.6°) sbcf [25.3]	29	21	30	30	33	22	11	0	27	28	39	37
(−20.3°) sbvt [17.1]	29	0	6	14	15	6	19	32	12	24	32	27
(−20.5°) sbcg [25.9]		57	33	25	33	13	20	18	7	26		
(−22.8°) sbgl [27]	39	30	28	38	27	31	15	23	12	21	37	36
(−23.5°) sbmt [30.2]	26	36	41	38	30	16	29	18	29	27	36	33
(−25.5°) sbct [27.6]	31	24	25	50	11	17	43	26	19	17	36	36
(−25.6°) sbfi [37.9]	38	100	36	45	23	38	28	25	38	31	19	33
(−29.7°) sbsm [29.6]	35	37	20	26	35							
(−29.8°) sbug [24.7]									19	25	29	25
(−30°) sbpa [32.5]	25	41	31	37	42	39	19	17	14	37	45	36

FIGURE 4.10 – Monthly counts of GWs (top) in the lower stratosphere in 2014 and ratio between the counts and the number of radiosonde launches (bottom). The rows correspond to aerodromes ordered by geographic latitude. Values between [ ] mean average values by line and column (BRHIAN *et al.*, 2024).

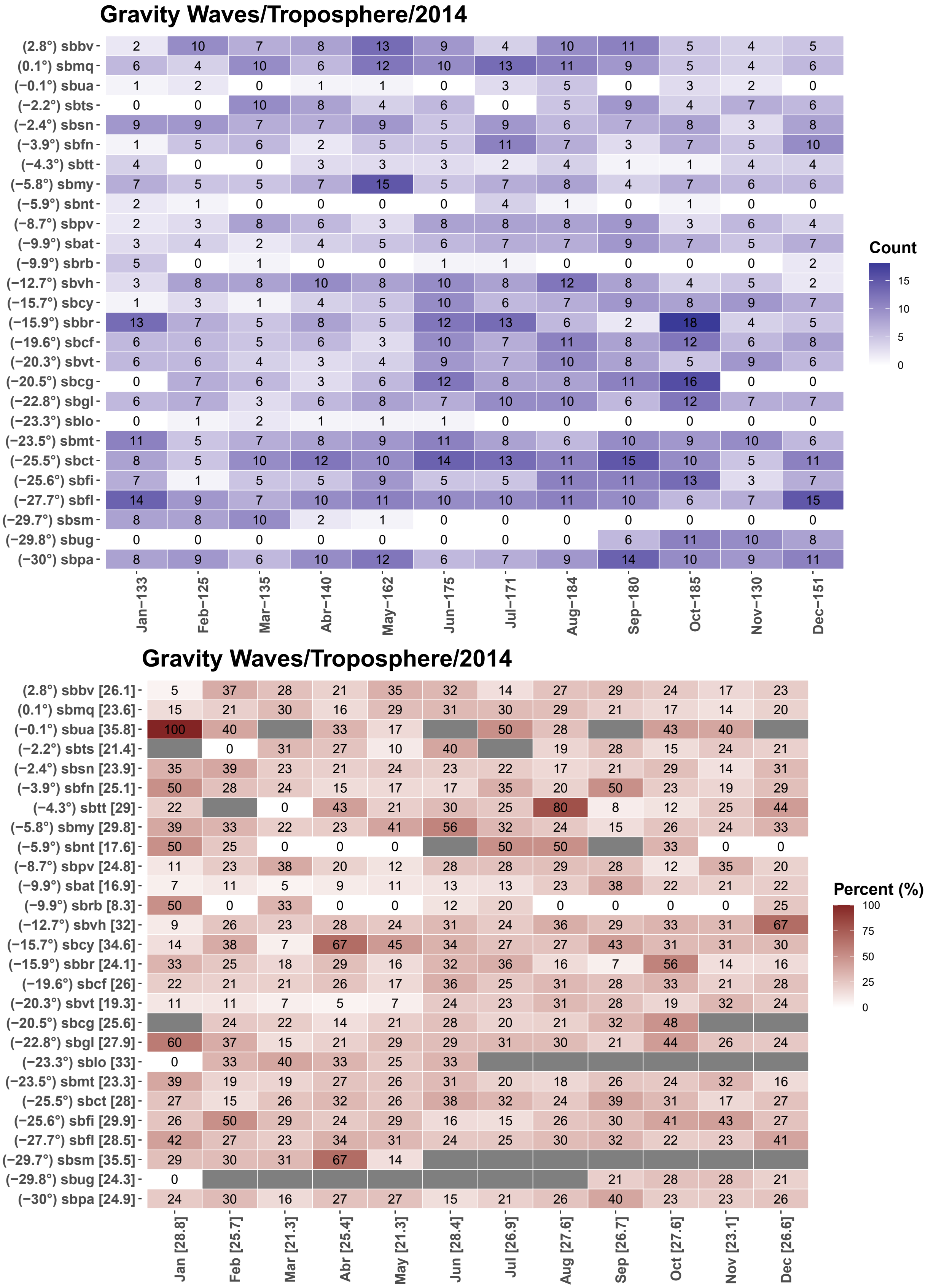

Gravity Waves/Troposphere/2014

	Jan−133	Feb−125	Mar−135	Abr−140	May−162	Jun−175	Jul−171	Aug−184	Sep−180	Oct−185	Nov−130	Dec−151
(2.8°) sbbv	2	10	7	8	13	9	4	10	11	5	4	5
(0.1°) sbmq	6	4	10	6	12	10	13	11	9	5	4	6
(−0.1°) sbua	1	2	0	1	1	0	3	5	0	3	2	0
(−2.2°) sbts	0	0	10	8	4	6	0	5	9	4	7	6
(−2.4°) sbsn	9	9	7	7	9	5	9	6	7	8	3	8
(−3.9°) sbfn	1	5	6	2	5	5	11	7	3	7	5	10
(−4.3°) sbtt	4	0	0	3	3	3	2	4	1	1	4	4
(−5.8°) sbmy	7	5	5	7	15	5	7	8	4	7	6	6
(−5.9°) sbnt	2	1	0	0	0	0	4	1	0	1	0	0
(−8.7°) sbpv	2	3	8	6	3	8	8	8	9	3	6	4
(−9.9°) sbat	3	4	2	4	5	6	7	7	9	7	5	7
(−9.9°) sbrb	5	0	1	0	0	1	1	0	0	0	0	2
(−12.7°) sbvh	3	8	8	10	8	10	8	12	8	4	5	2
(−15.7°) sbcy	1	3	1	4	5	10	6	7	9	8	9	7
(−15.9°) sbbr	13	7	5	8	5	12	13	6	2	18	4	5
(−19.6°) sbcf	6	6	5	6	3	10	7	11	8	12	6	8
(−20.3°) sbvt	6	6	4	3	4	9	7	10	8	5	9	6
(−20.5°) sbcg	0	7	6	3	6	12	8	8	11	16	0	0
(−22.8°) sbgl	6	7	3	6	8	7	10	10	6	12	7	7
(−23.3°) sblo	0	1	2	1	1	1	0	0	0	0	0	0
(−23.5°) sbmt	11	5	7	8	9	11	8	6	10	9	10	6
(−25.5°) sbct	8	5	10	12	10	14	13	11	15	10	5	11
(−25.6°) sbfi	7	1	5	5	9	5	5	11	11	13	3	7
(−27.7°) sbfl	14	9	7	10	11	10	10	11	10	6	7	15
(−29.7°) sbsm	8	8	10	2	1	0	0	0	0	0	0	0
(−29.8°) sbug	0	0	0	0	0	0	0	0	6	11	10	8
(−30°) sbpa	8	9	6	10	12	6	7	9	14	10	9	11

Gravity Waves/Troposphere/2014

	Jan [28.8]	Feb [25.7]	Mar [21.3]	Abr [25.4]	May [21.3]	Jun [28.4]	Jul [26.9]	Aug [27.6]	Sep [26.7]	Oct [27.6]	Nov [23.1]	Dec [26.6]
(2.8°) sbbv [26.1]	5	37	28	21	35	32	14	27	29	24	17	23
(0.1°) sbmq [23.6]	15	21	30	16	29	31	30	29	21	17	14	20
(−0.1°) sbua [35.8]	100	40		33	17		50	28		43	40	
(−2.2°) sbts [21.4]		0	31	27	10	40		19	28	15	24	21
(−2.4°) sbsn [23.9]	35	39	23	21	24	23	22	17	21	29	14	31
(−3.9°) sbfn [25.1]	50	28	24	15	17	17	35	20	50	23	19	29
(−4.3°) sbtt [29]	22		0	43	21	30	25	80	8	12	25	44
(−5.8°) sbmy [29.8]	39	33	22	23	41	56	32	24	15	26	24	33
(−5.9°) sbnt [17.6]	50	25	0	0	0		50	50		33	0	0
(−8.7°) sbpv [24.8]	11	23	38	20	12	28	28	29	28	12	35	20
(−9.9°) sbat [16.9]	7	11	5	9	11	13	13	23	38	22	21	22
(−9.9°) sbrb [8.3]	50	0	33	0	0	12	20	0	0	0	0	25
(−12.7°) sbvh [32]	9	26	23	28	24	31	24	36	29	33	31	67
(−15.7°) sbcy [34.6]	14	38	7	67	45	34	27	27	43	31	31	30
(−15.9°) sbbr [24.1]	33	25	18	29	16	32	36	16	7	56	14	16
(−19.6°) sbcf [26]	22	21	21	26	17	36	25	31	28	33	21	28
(−20.3°) sbvt [19.3]	11	11	7	5	7	24	23	31	28	19	32	24
(−20.5°) sbcg [25.6]		24	22	14	21	28	20	21	32	48		
(−22.8°) sbgl [27.9]	60	37	15	21	29	29	31	30	21	44	26	24
(−23.3°) sblo [33]	0	33	40	33	25	33						
(−23.5°) sbmt [23.3]	39	19	19	27	26	31	20	18	26	24	32	16
(−25.5°) sbct [28]	27	15	26	32	26	38	32	24	39	31	17	27
(−25.6°) sbfi [29.9]	26	50	29	24	29	16	15	26	30	41	43	27
(−27.7°) sbfl [28.5]	42	27	23	34	31	24	25	30	32	22	23	41
(−29.7°) sbsm [35.5]	29	30	31	67	14							
(−29.8°) sbug [24.3]	0								21	28	28	21
(−30°) sbpa [24.9]	24	30	16	27	27	15	21	26	40	23	23	26

FIGURE 4.11 – Monthly counts of GWs (top) in the troposphere in 2014 and ratio between the counts and the number of radiosonde launches (bottom). The rows correspond to aerodromes ordered by geographic latitude. Values between [ ] mean average values by line and column (BRHIAN *et al.*, 2024).

Figure 4.12 shows that in the troposphere and lower stratosphere the monthly count rates of monochromatic waves are more likely constant. Also, the count rates were mostly less than 35 % in both cases. The hypothesis of constant count rate is more likely in the troposphere, where the p-value of the Cochran-Armitage test (ARMITAGE, 1955; CHOCHRAN, 1954) was 0.91%, while in the lower stratosphere case the p-value value was 8.98%. The Cochran–Armitage is a statistical test for trend which is applied here to test if the GWs count rate probability is independent of the month (null hypothesis). The p-values of this test show that the existence of a lower count rate in the winter should not be discarded in the lower stratosphere case. The sample of GWs in the lower stratosphere indicates that the amount of monochromatic GWs in the dry season tends to be smaller.

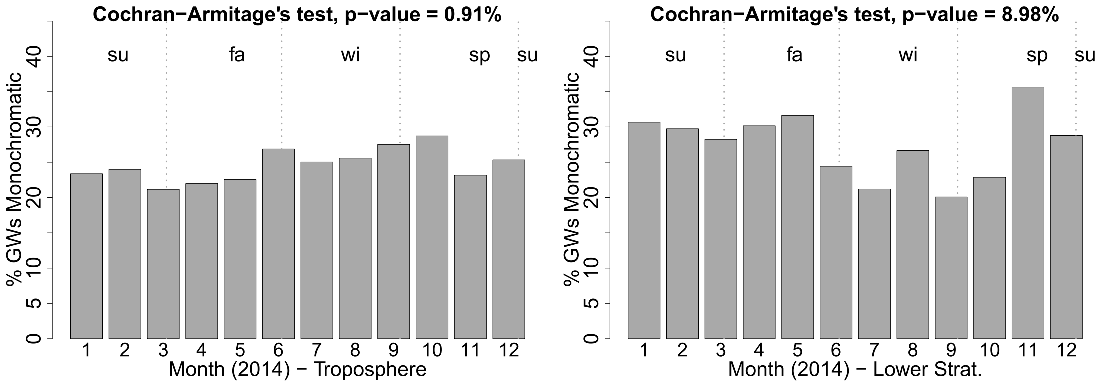

FIGURE 4.12 – Count of GWs in the troposphere (left) and lower stratosphere (right) (BRHIAN *et al.*, 2024).

The vertical wavelengths computed for each atmospheric layer and grouped according to day period (dusk/dawn) are shown in Figure 4.14 as function of time. The wavelength distribution is symmetric, independently of whether it is dawn or dusk, or whether it is the wet or dry season, see Figure 4.13. The wavelength distribution is also independent of the location of the aerodromes (geographic latitude). Considering all the measurements of monochromatic waves in 2014 in the troposphere, the calculated mean values ± standard deviation for the vertical wavelength was (6.07 ± 0.90) km for dawn time and (6.06 ± 0.87) km for dusk time. For the lower stratosphere, the mean values ± standard deviation for the vertical wavelength was (2.87 ± 0.73) km for dawn time and (3.15 ± 0.72) km for dusk time, very similar to the values found by Vincent and Alexander (2000), where they analyzed radiosonde data from September 1992 to June 1998 over the Indian Ocean (12°S,97°E) and found vertical wavelengths in the interval 2-3 km after applying the same methodology of this work. The study of Allen & Vincent (1995), already mentioned in this paper, found average vertical wavelengths close to 2.5 km for both layers.

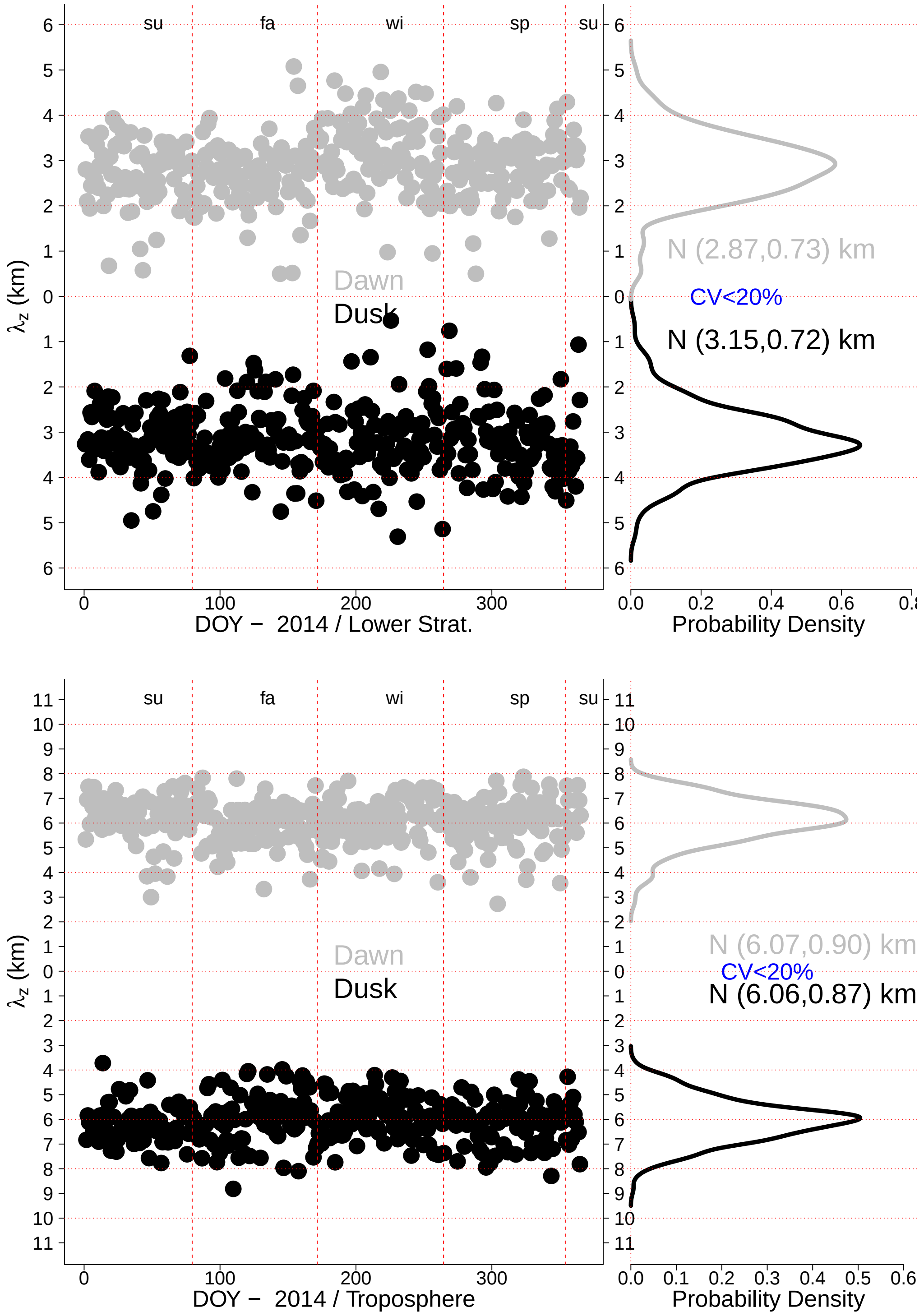

FIGURE 4.13 – Left: daily variation of the GWs vertical wavelengths with coefficient of variation less than 20 % (between zonal wind, meridional wind and temperature) in the troposphere (bottom) and lower stratosphere (top) in 2014 besides their time (dawn or dusk). Right: vertical wavelength probability density discriminated by time of launch of radiosonde. The parameters of mean and standard deviation from one normal distribution was estimated and show in the middle of each graphic - note that both direction of ordinate axis axis has only positive values to the vertical wavelength.

Hence, the mean vertical wavelength in the lower stratosphere was shorter than the mean vertical wavelength in the troposphere. These average values for the vertical wavelengths, in both layers, agree well with the values reported by Vincent et. al. (1997), who studied GWs using data acquired by radiosondes launched twice a day from 1993 to 1994 in Macquarie Island (55°S,159°E) and analyzed it using third-order cubic spline wind profile interpolation at 50 m intervals. Vertical wavelengths around 3 km in the lower stratosphere was also found by Zhang and Yi (2005) in Wuhan (30°N,114°E), who studied GWs using data from radiosondes launched from 2000 to 2002 and based their analysis on a methodology similar to the one used in this work. There seems to be no latitudinal difference in the vertical wavelength averages measured using radiosondes when comparing our results at low latitudes with the results at middle latitudes of these studies, showing that vertical wavelength from GWs is independent of Coriolis force influence.

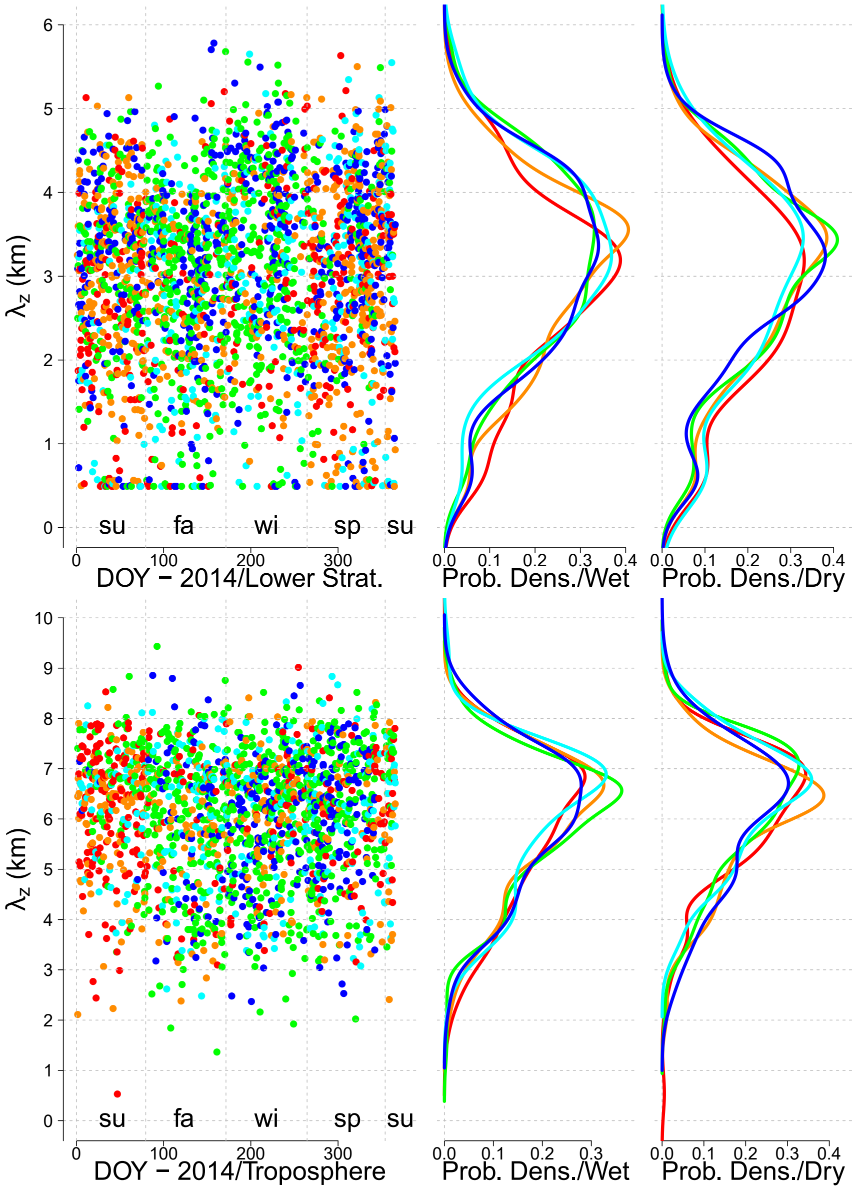

FIGURE 4.14 – Left: daily variation of the GWs vertical wavelengths with coefficient of variation less than 20 % (between zonal wind, meridional wind and temperature) in the troposphere (bottom) and lower stratosphere (top) in 2014. Right: vertical wavelength probability density discriminated by the cluster to which the measurements belong and season (dry/wet). The colors correspond to the clusters defined previously in Figure 4.3 (BRHIAN *et al.*, 2024).

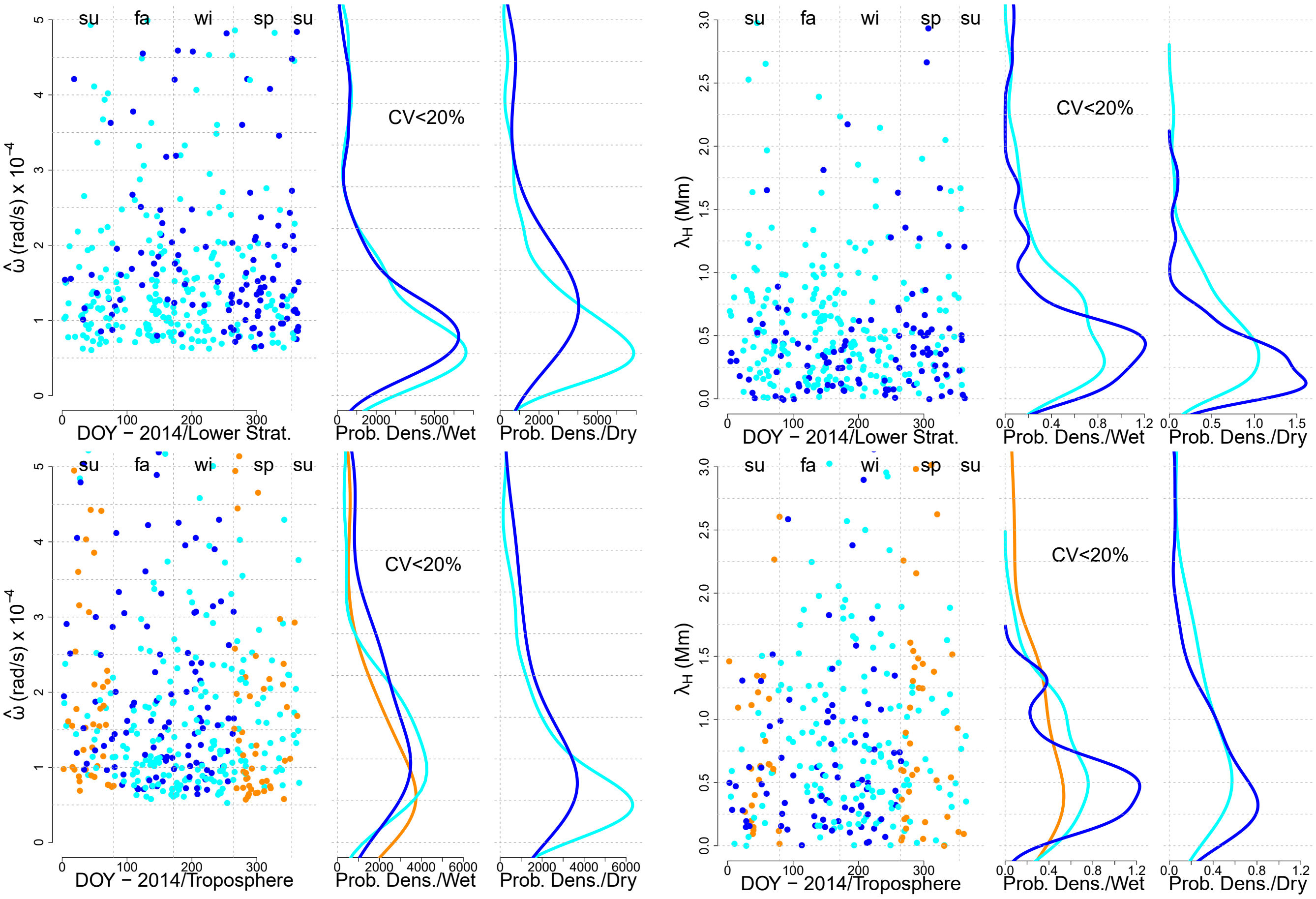

FIGURE 4.15 – Left: intrinsic angular frequency $\hat{\omega}$ of the GWs in the troposphere and lower stratosphere in 2014 as a function of time for aerodromes located at latitudes greater than 20° (southernmost aerodromes) and their probability density of the intrinsic angular frequency discriminated by the cluster to which the measurements belong and season (dry/wet). The fewer colors in the plot is a consequence of the 20° cut (see text). Right: The same description of left, but refer to horizontal wavelength. Top: Refer to lower stratosphere layer. Bottom: Refer to troposphere layer. The colors correspond to the clusters defined previously in Figure 4.3 (BRHIAN *et al.*, 2024).

The values of the ratio $\hat{\omega}/f$ were computed dividing the major axis by the minor axis of the GW hodograph ellipsis (TSUDA *et al.*, 1990; VINCENT *et al.*, 1997; VINCENT; ALEXANDER, 2000). This method is based in the theory of internal wave propagation in the atmosphere, and it was used to determine the intrinsic wave angular frequency $\hat{\omega}$ by multiplying that ratio by the Coriolis factor f as explained in section 2.4. The computed values are shown in Figure 4.15. The period varied between 6 h to 17 h ($f_{\hat{\omega}} = 1.0 \times 10^{-4}/2\pi$ Hz to $f_{\hat{\omega}} = 3.0 \times 10^{-4}/2\pi$ Hz, where the frequency ($f_{\hat{\omega}} = \hat{\omega}/2\pi$) correspond to the first and third quartiles) for latitude greater than 20° in Brazilian territory for both layers. In addition, the value of $\hat{\omega}$ increased monotonically with latitude and, conversely, the period of GWs decreased monotonically with latitude. Considering the most likely values of intrinsic frequencies and the average values of the vertical wavelength, the vertical velocities of the monochromatic GWs in both layers varied typically from 1.0×10^{-1} m/s to 2.9×10^{-1} m/s (troposphere) and 5.0×10^{-2} m/s to 1.2×10^{-1} m/s (lower stratosphere). These results show that the vertical velocities of GWs in the troposphere were usually greater than the vertical velocities in the lower stratosphere (VINCENT; ALEXANDER, 2000). Observations of GWs in the mesosphere above Shiraki, Japan (35°N, 136°E) on October 13-31, 1986 using Middle and Upper Atmosphere Radar, showed that vertical wavelengths were in the range from 5 to 15 km and that the intrinsic period was about 8.6 h (TSUDA *et al.*, 1990). This could have more than one explanation: one is the filtering effect (ALEXANDER, 1998), that will be discussed later, and the other is the natural blocking of waves that have relatively small vertical wavelengths (FRITTS; ALEXANDER, 2003). Because of the filtering effect, the radiosonde method can only measure waves within a given frequency interval, favoring low frequency waves which are also in the low wavelength part of the GW spectrum. This could explain why the mean vertical wavelength measured by radiosonde was smaller than the one measured using radar. It is also possible that this difference is a manifestation of the natural blocking and absorption of low frequency inertia-gravity waves (FRITTS; ALEXANDER, 2003).

The horizontal wavelength of quasi-monochromatic GWs propagating in the troposphere for aerodromes with latitudes greater than 20° had a median value of 582 km in the wet season and 690 km in the dry season (see Figure 4.15), very similar for founded by Moffat-Griffin et. al. (2011, 2020). In the lower stratosphere, the median values for the horizontal wavelength was 495 km in the wet season and 379 km in the dry season. We did not find any significant difference between the horizontal wavelength from locations at different latitudes in both layers. Using the computed horizontal wavelengths and the wave frequencies $\hat{\omega}$, we computed the wave horizontal velocity. In the troposphere the horizontal velocity was in the range between $4.6 \times 10^0 - 5.7 \times 10^0$ m/s. In the lower stratosphere, the horizontal velocity was in the range between $3.5 \times 10^0 - 3.0 \times 10^1$ m/s.

Finally, we have taken the values of amplitude, vertical wavelength and phase of the monochromatic GWs and computed the correlation coefficients between the lower stratosphere values and the troposphere values for each aerodrome (figure not shown). Here again all the average correlation coefficients were close to zero, which is consistent with the hypothesis of weak coupling between GWs from different atmospheric layers.

4.1.4 Sources of Mesospheric GWs

The sources of mesospheric GWs studied in previous works used measurements from all-sky imagers combined with a reverse ray tracing method, showed that the most probable location of excitation of the wave in lower altitudes (DARE-IDOWU *et al.*, 2020; NYASSOR *et al.*, 2022). These works identified regions of excitation corresponding to locations where deep convection is expected, such as the ITCZ. Other studies, in other locations, showed that deep convection was not the major source of the sampled GWs (GIONGO *et al.*, 2020; SIVAKANDAN *et al.*, 2019). A study using reverse ray tracing based on a large sample of

OH airglow radiometer images observed in Davis Station Antarctica found that only 15% of the GWs ray paths originated in the troposphere (ROURKE *et al.*, 2017).

The ray tracing method has some caveats, but in our view, it provides a valid estimate of the approximate location of GWs sources. However, since previous studies using this method have identified deep convection regions as the origin of GWs, it becomes challenging to reconcile these findings with the main conclusion of our research, which found no significant correlation between tropospheric and lower stratospheric GWs.

As far as we are aware, these works rely on few recordings of propagating GWs observed by all sky imagers, so one cannot be sure of its statistical significance. Few samples are not enough to provide conclusive results. In the radiosonde case, on the other hand, the sample is much larger, but it can be biased due to the suppression of launches in bad weather conditions, many of which may be associated with deep convection. Having said that, there are good physical reasons to expect that deep convection is an authentic source of mesospheric GWs, among others. However, the atmospheric perturbation that originates GWs at mesospheric heights would not be observed as a linear wavefront if some measurement device was placed in the location of its birth. This point gives what we believe is the key to the correct interpretation of our results: the linear wavefronts of GWs that manifest in the troposphere are usually blocked on the tropopause (conclusion from observation), but large and non-linear perturbations produced in the troposphere, eventually extending into the lower stratosphere, could generate GWs at mesospheric heights.

4.1.5 Implications to the Seeding Problem

Here we shall drop some comments on the seeding problem. This work was partially motivated by the speculation that the information from GWs measured by radiosondes could be used to estimate the variability of the initial perturbations at the bottom side of the equatorial ionosphere. In a future work, we shall investigate the correlation between radiosonde measurements and the ROTI index, but the present results may provide us some insights. The main point here is that inertia-gravity waves detected by radiosondes at the lower atmosphere are more likely to be blocked at higher layers. For this reason, radiossonde measurements of GWs do not seem to be the best methodology to tackle the question of whether or not the lower atmosphere conditions explain the higher atmosphere perturbations that seeds the instabilities. Even if such perturbations are partially explained by lower atmosphere activity, this information may be useless if perturbations are ubiquitous. A recent work by Hyssel and his collaborators showed that plasma bubbles can be predicted accurately by current models if the ambient electric field and zonal winds are known accurately (HYSELL *et al.*, 2022). These models only need a background

Gaussian noise to trigger a bubble event whenever the required ambient conditions are present. This suggests that detailed information about the initial seed perturbation may not be necessary to achieve the desired predictability of plasma bubbles and scintillation.

4.1.6 Caveats

The radiosonde measurements have some limitations that must be mentioned for a critical review of our work. The main limitation is the filtering effect (ALEXANDER, 1998). The wind amplitudes of GWs are measured while the balloon is in motion, so it can only probe reliably waves that move slower than the balloon or change its phase only slightly during the radiosonde transit. Because of that, high-frequency waves tend to be filtered out. Another problem, that manifest in the lower stratosphere, is the limitation of the height interval of probing. If GWs having vertical wavelengths greater than this interval occur, they would not be identified using radiosonde measurements - this is not a limitation of the radiosonde technique in general, but of the weather balloons used to launch the radiosondes in this study. Finally, there is a methodological limitation related to the detrending analysis. We assumed that the wind and temperature profiles had parabolic shapes. By running some numerical simulations we verified that the detrending technique works properly if the underlying hypothesis of parabolic shape is true. However, if the hypothesis of parabolic shape fails, it would not be possible to guarantee that the detrending analysis resulted in a correct oscillating profile.

One worth mentioning consequence of this filtering effect is that GWs with longer vertical wavelengths – which also happen to have higher vertical group and phase velocities – are not detected by radiosonde measurement (ALEXANDER, 1998). These GWs are more likely to reach the stratosphere and mesosphere without being filtered. Such GWs can originate in the troposphere, but their vertical wavelengths are so large that in the scale length of the troposphere they would not be seen as a linear wavefront, but as local perturbation, propagating non linearly, which will later disperse and form the wave fronts observed in the stratosphere and mesosphere.

4.2 Ionosphere

4.2.1 Station

The data analyzed in this study were acquired from GPS receivers located in Brasília, Brazil, with geographic coordinates of (15° 56’ 50.91123”S, 47° 52’ 40.32834”W) at an altitude of 1106.02 m and epoch 2000.4, according to SIRGAS2000 (BRASIL, 2023; BRASIL, 2024). The data span approximately twelve years of solar cycle 24. This station, hereafter referred to as "*braz*", is indicated on the map in Figure 4.16. Within the study timeframe, the following GNSS receivers were used: TRIMBLE NETR8, TRIMBLE NETRS, LEICA GR25 and TRIMBLE NETR9 (BRASIL, 2023). The magnetic coordinates of the station were (6.96°S, 23.84°W) in 2014 (IAGA, 2024), with additional magnetic variables shown in Table 4.2.

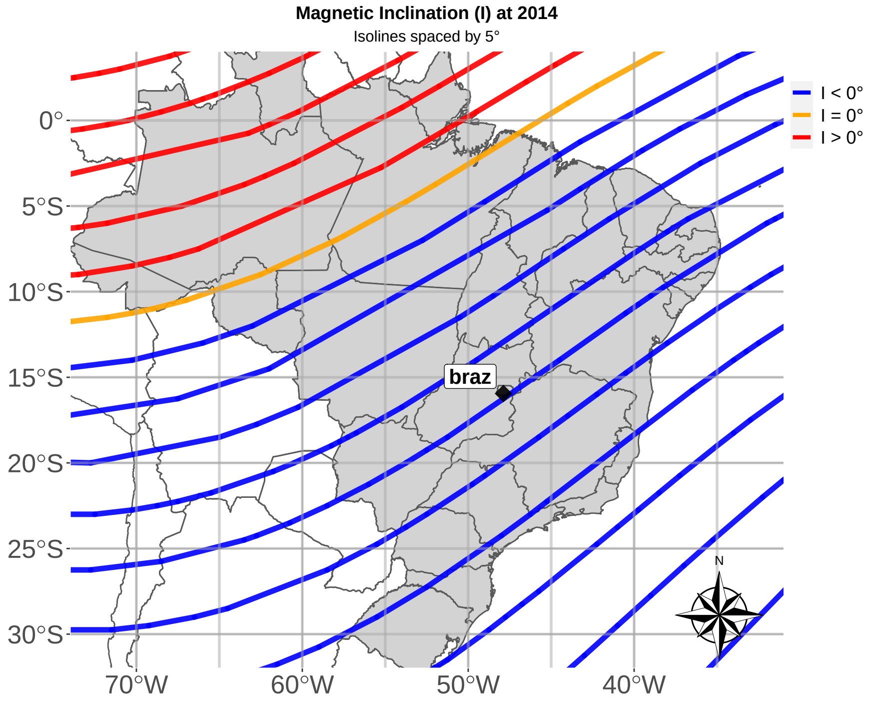

FIGURE 4.16 – Geographic location of *braz* station and magnetic inclination (I) contour lines at altitude 350 km in 2024.

TABLE 4.2 – Magnetic variables and geomagnetic coordinates at 2010 and 2022 in 350 km in *braz* station. These values were computed using the IGRF-13 model (IAGA, 2024).

	2010	2022
Magnetic Inclination (I)	-23.03°	-27.64°
Magnetic Declination (D)	-18.98°	-19.93°
Magnetic Component (B)	20,247.0 nT	20,131.1 nT

4.2.2 Variables

Figure 4.17 illustrates that the variations in TLS and EAS over the course of a year are quite similar. The minimum values occur during the winter season, while the maximum values are observed in the summer. In this geographic location, the duration of daylight is approximately 11.05 hours in winter and around 12.95 hours in summer. The minimum EAS is 50.63° in winter and the maximum EAS reaches 86.66° in summer.

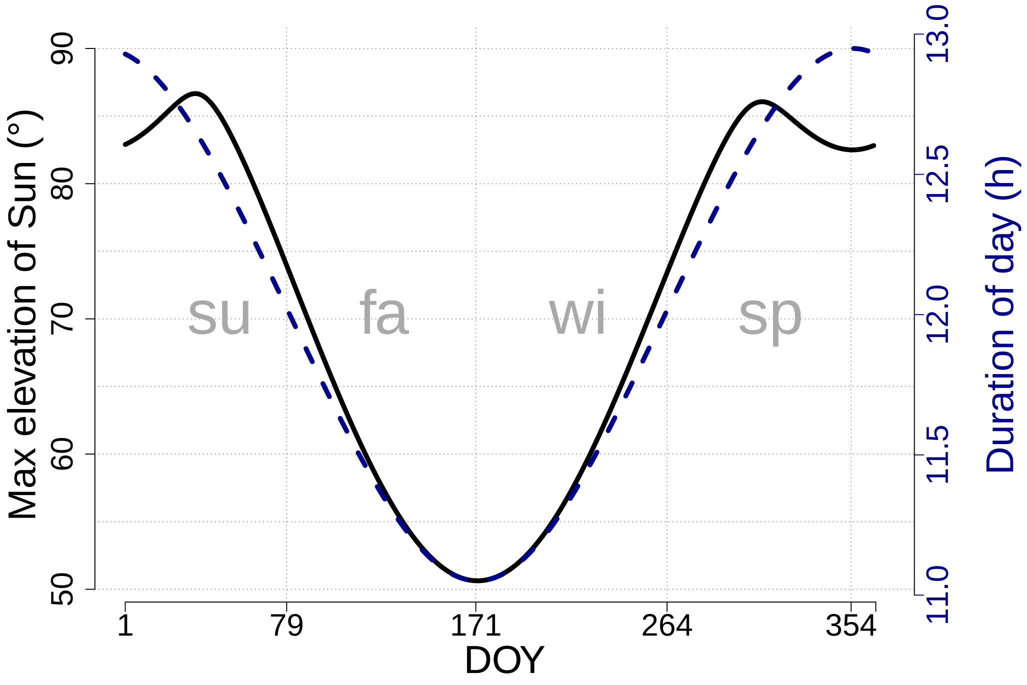

FIGURE 4.17 – Day duration and daily maximum elevation angle of the Sun (EAS) as a function of DOY for the *braz* station (su = summer, fa = fall, wi = winter and sp = spring).

The daily values of the $F_{10.7}$ index, expressed in solar flux units (sfu), where 1 sfu = 10^{-22} W/(m^{2}Hz), are shown in Figure 4.18 for the duration of this study. In this figure, red points indicate nights when the ionosphere was classified as *irregular*, that is, with $ROTI > 0.5$, while green points represent nights classified as *regular*, contrary case. The variation in $F_{10.7}$ correlates with fluctuations in solar activity; specifically, during solar maximum, the occurrence of irregular ionosphere nights is higher compared to solar minimum.

Figure 4.19 shows the histogram of the K_p index for two different conditions: the histogram in strong colors considers only the condition where the ionosphere was regular, while the histogram in weak colors considers only the condition when the ionosphere was irregular. The cumulative distributions are also shown. The three different colors of the vertical bars indicate the category of the magnetospheric state, defined earlier as *Quiet* (green), *Active* (yellow), and *Storm* (red). The *Active* and *Storm* states of the magnetosphere amounted to less than 10% of the data. Quiet magnetospheric states were slightly more frequent for the regular ionosphere, while Active magnetospheric states were slightly more frequent for the irregular ionosphere. A similar pattern was found by Secan et al. (1995), who analyzed ionospheric scintillation in Huancayo (12.04°S, 75.32°W, dip: -2.58° at 1982), Manila (14.60°N, 120.98°E, dip: 4.5° at 1982), and Ascension Island (7.95°S, 14.37°W, dip: -57.32° at 1982). These differences do not appear to be statistically

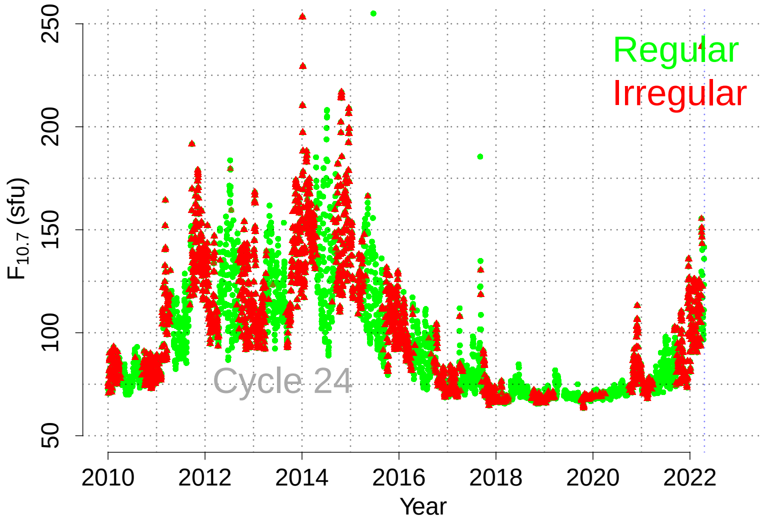

FIGURE 4.18 – Temporal series of $F_{10.7}$ within the time frame of this study. Points in red indicate nights when the ionosphere was *irregular*, while points in green indicate the nights when the ionosphere was *regular* during all the night.

significant, as the frequency distributions for regular and irregular ionospheric states were considered equal at a 5% significance level according to the χ^2 and Kolmogorov-Smirnov tests.

The ROTI values, depicted in Figure 4.20, vary with year and local time. Notably, ionospheric irregularities were more frequent and intense during the peak periods of solar cycle 24. At this station, these irregularities were more likely to occur between October and March. During solar maximum periods, they typically began around 19:00 LT and persisted until approximately 03:00 LT. In contrast, during solar minimum periods, these irregularities started later and ended earlier. Furthermore, ionospheric irregularities occurring in winter or around sunrise are often associated with geomagnetic storms and substorms (CARMO *et al.*, 2022).

4.2.3 Application of the GLMs

This paper utilized eight models, as shown in Table 4.5, comprising two combinations of independent variables and four different link functions. Figure 4.21 illustrates the relationship between the independent and dependent variables.

Once calibrated with the training data, each model computed the *estimated probabilities* $\hat{p}$. To illustrate the fitting parameters for a specific model, consider one where K_p has two levels (or factors), the link function is *logit* and all interactions among the independent variables are included. The model parameters are:

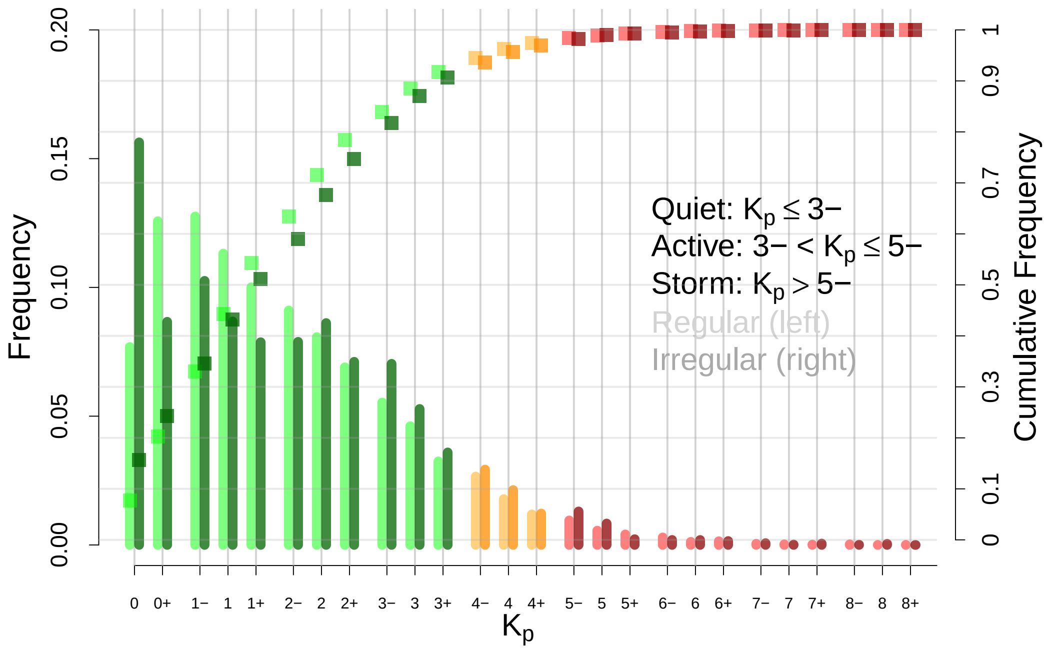

FIGURE 4.19 – Histograms of K_p index during solar cycle 24 for the *regular* and *irregular* ionospheric states above *braz* station. The classification of magnetosphere states in K_p intervals follows the definitions proposed by BGS and NOAA.

$$\begin{aligned}\boldsymbol{\beta} = [&\beta_0, \beta_{K_{p.AS}}, \beta_{F_{10.7}r}, \beta_{EASr}, \beta_{TLSr},\\ &\beta_{K_{p.AS}:F_{10.7}r}, \beta_{K_{p.AS}:EASr}, \beta_{K_{p.AS}:TLSr}, \beta_{EASr:TLSr}, \beta_{EASr:F_{10.7}r}, \beta_{TLSr:F_{10.7}r},\\ &\beta_{K_{p.AS}:F_{10.7}r:EASr}, \beta_{K_{p.AS}:F_{10.7}r:TLSr}, \beta_{K_{p.AS}:EASr:TLSr}, \beta_{F_{10.7}r:EASr:TLSr},\\ &\beta_{K_{p.AS}:F_{10.7}r:EASr:TLSr}], \qquad (4.1)\end{aligned}$$

where β_0 is the intercept; $\beta_{K_{p.AS}}$ is the coefficient associated with $X_{K_{p.AS}}$, which is equal to 1 when the magnetospheric state is *active-storm* and 0 when it is *quiet*; $\beta_{F_{10.7}r}$ is the coefficient for $X_{F_{10.7}r}$; $\beta_{K_{p.AS}:F_{10.7}r}$ is the coefficient for the interaction term $X_{K_{p.AS}} \times X_{F_{10.7}r}$; and so on.

The variables derived from GWs, such as kinetic and potential energy densities, were included as parameters in the model to investigate their influence on predicting ionospheric irregularities. Previous studies suggest that these variables effectively represent the energy transport of GWs and their potential contribution as seeding mechanisms for Rayleigh-Taylor instabilities (FRITTS; ALEXANDER, 2003; YIGIT, 2015). However, preliminary results pointed to a limited contribution, with greater relevance from variables related to time, day of year, solar cycle and geomagnetic state.

Figure 4.22 presents a histogram of the $\hat{p}$ values for this model. The low probabilities observed in this model may be due to the dominance of data points where ionospheric irregularities do not occur, which can skew the model's predictions. The histogram has a

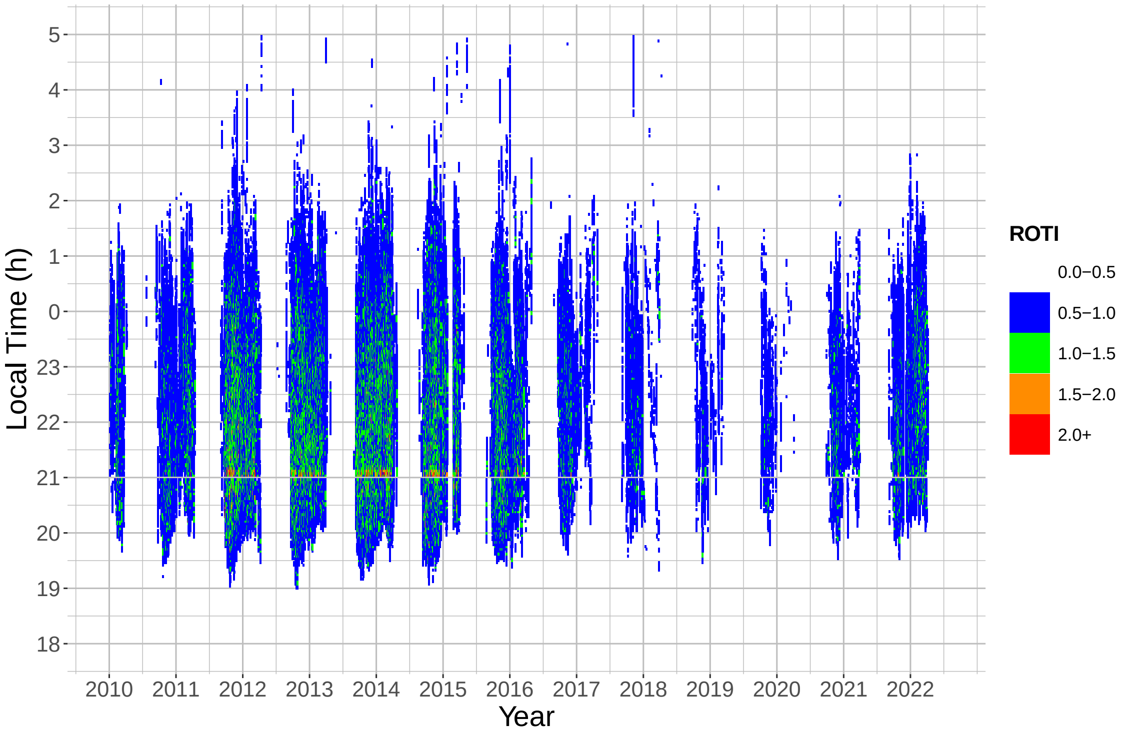

FIGURE 4.20 – The 3^{rd} quartile of ROTI as a function of year and local time in the *braz* station. The distribution of staring hour of occurrence appears to be asymetrical: starting hour for november is earlier than february. The ending hour does not show such a clear pattern.

multimodal shape, reflecting the categorical nature of the K_p variable and its interactions. It also shows the deciles of $\hat{p}$, which can serve as thresholds to classify the state of the ionosphere. The estimated $\boldsymbol{\beta}$ parameters are listed in Table 4.3, which presents the adjusted coefficients (Estimated), standard errors (Std. Error), z values, p-values from the z-test (P-value (> |z|)), and the odds, discussed later. According to the z-test, the parameters associated with the independent variables $EASr : F_{10.7}r$ and $K_{p.AS} : F_{10.7}r : EASr$ are not statistically significant at the 5% significance level. The last column in Table 4.3 shows the value of $e^{\beta_{(\cdot)} \times X_n}$ for $X_n = 1$, which can be interpreted as the contribution to the odds of observing an *irregular* ionospheric state for the given parameter at the maximum values of the associated variables. This value indicates the impact of the variables on $\hat{p}$, relevant for *logit* models only.

For the *quiet* magnetosphere condition, the variables that increased the odds of observing irregularities were $EASr : TLSr(8.02) < F_{10.7}r(8.6) < EASr(9.10) < TLSr : F_{10.7}r(12.67)$. Conversely, the variables that decreased the odds were $F_{10.7}r : EASr : TLSr$(-16.31) $< TLSr$(-8.81). In the *Active-Storm* case, the variables that increased the odds of observing irregularities were $K_{p.AS}(1.51)$[-8.82] $< TLSr(2.86)$[-5.95] $< F_{10.7}r : EASr : TLSr(6.72)$[-9.59], where the value in brackets is the effective parameter value that multiplies the variable. The variables that decreased the odds were $F_{10.7}r : TLSr$(-

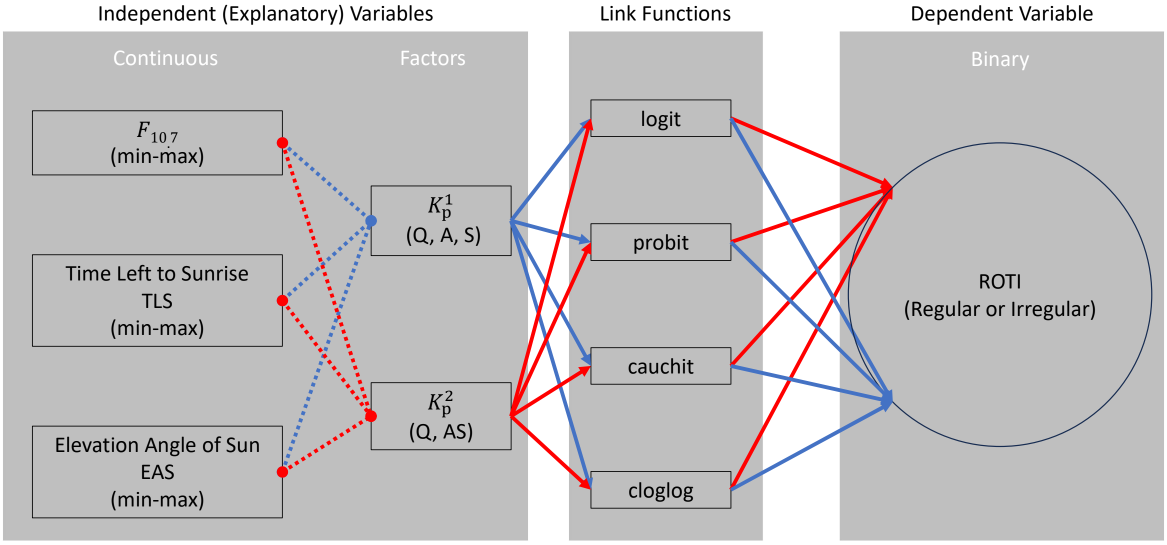

FIGURE 4.21 – Diagram of the eight models used in this study. In some models, the K_p index was categorized as *quiet* (Q), *active* (A), or *storm* (S). In the other models, K_p was categorized as either *quiet* (Q) or *active-storm* (AS). The normalization was made by interpolation method with minimum and maximum values (min-max).

5.29)[7.38] $< F_{10.7}r$(-4.8)[3.8] $< EASr : TLSr$(-2.83)[5.19] $< EASr$(-1.25)[7.85].

The Analysis of Variance (ANOVA) was evaluated to test the statistical relevance of the parameters, comparing whether or not the adding or removing one parameter is statistically significant. The test results demonstrated that only two parameters, associated to $K_{p.AS} : EASr$ and $K_{p.AS} : EASr : TLSr$, were statistically irrelevant at a 5% significance level.

After estimating $\hat{p}$ and their corresponding coefficients, thresholds were selected to classify the ionosphere state. These thresholds were defined based on quantile values of $\hat{p}$ (see histogram in Fig. 4.22) and, for each one, the FNR, the FPR and the AUC-ROC were calculated. Figure 4.23 illustrates the FNR, FPR and AUC-ROC as functions of the quantile values, where this figure will help to choose the best threshold value. The confusion matrix statistics derived from the training data closely matched those from the test data. Additionally, the FNR and FPR curves intersected near the 76^{th} quantile at approximately 17.5%. According to AUC-ROC, the optimal threshold occurred around the 68^{th} quantile of $\hat{p}$, at 84.2%.

FNR, FPR and AUC-ROC were also calculated for the other models, with the results presented in Table 4.5, using the median of $\hat{p}$ as the classification threshold. All models demonstrated a good fit, as the differences between the figures of merit calculated from the training data (in the columns ended with .tr) and those from the test data (in the

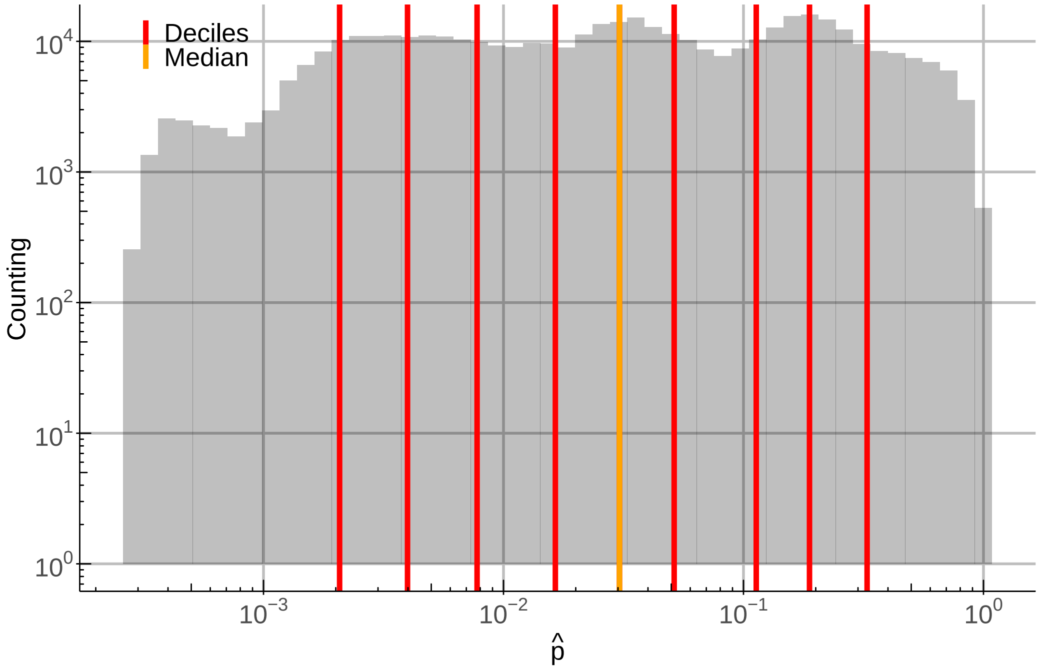

FIGURE 4.22 – Histogram of the predicted probabilities $\hat{p}$ for the model with parameters defined by Equation 4.1.

columns ended with .te) were minimal in every case. Models 3 and 4 achieved the optimal values, as highlighted in the table. However, based on the principle of parsimony, Model 4 should be preferred as the optimal model over Model 3.

It is important to note that there is flexibility in selecting an optimal threshold, with the best choice depending on the relative importance assigned to each figure of merit, which is application dependent. If we choose the threshold as the quantile value at the crossing point between the FNR and FNR curves, the model's sensitivity (1 - FNR) and specificity (1 - FPR) are, by definition, equal and reach a value of (82.5 ± 0.76)% (threshold set at the 76^{th} quantile) for model 2. This means the model has an equal probability of correctly predicting both regular and irregular ionospheric conditions, with an accuracy of (82.5 ± 0.76)%. In other words, out of 100 predictions, the model is expected to be correct 82 times, regardless of whether the ionosphere is regular or irregular. When considering the best model presented in Table 4.5, the sensitivity and specificity increase slightly to (82.83 ± 0.53)%, still at the 76^{th} percentile.

4.2.4 Explanatory Variables

This is a section where the results from explanatory variables in this thesis will be compared with results from the literature. Besides, the model results fitting by GLMs will be compared with other works that tried to model ionospheric irregularities with other

TABLE 4.3 – Estimated coefficients for a model that employs the *logit* link function and the two factor K_p model (Equation 4.1). The symbol * indicates parameters that fail the z-test.

	Estimate	Std. Error	z value	P-value(>|z|)	odds = $e^{\beta_{(\cdot)}\times 1}$
β_0	-10.33	0.20	-49.62	0.00	3.25×10^{-05}
$\beta_{K_{p.AS}}$	1.51	0.56	2.68	0.00	$4.56 \times 10^{+00}$
$\beta_{F_{10.7}r}$	8.60	0.47	18.11	0.00	$5.47 \times 10^{+03}$
β_{EASr}	9.10	0.22	41.23	0.00	$8.98 \times 10^{+03}$
β_{TLSr}	-8.81	0.44	-19.75	0.00	1.48×10^{-04}
$\beta_{K_{p.AS}:F_{10.7}r}$	-4.80	1.15	-4.17	0.00	8.21×10^{-03}
$\beta_{K_{p.AS}:EASr}$	-1.25	0.61	-2.05	0.04	2.83×10^{-01}
$^*\beta_{EASr:F_{10.7}r}$	-0.57	0.51	-1.10	0.26	5.64×10^{-01}
$\beta_{K_{p.AS}:TLSr}$	2.86	1.13	2.52	0.01	$1.75 \times 10^{+01}$
$\beta_{TLSr:F_{10.7}r}$	12.67	0.96	13.07	0.00	$3.19 \times 10^{+05}$
$\beta_{EASr:TLSr}$	8.02	0.47	16.99	0.00	$3.06 \times 10^{+03}$
$^*\beta_{K_{p.AS}:F_{10.7}r:EASr}$	2.41	1.32	1.82	0.06	$1.12 \times 10^{+01}$
$\beta_{K_{p.AS}:F_{10.7}r:TLSr}$	-5.29	1.96	-2.69	0.00	5.02×10^{-03}
$\beta_{K_{p.AS}:EASr:TLSr}$	-2.83	1.22	-2.31	0.02	5.87×10^{-02}
$\beta_{F_{10.7}r:EASr:TLSr}$	-16.31	1.04	-15.66	0.00	8.18×10^{-08}
$\beta_{K_{p.AS}:F_{10.7}r:EASr:TLSr}$	6.72	2.21	3.04	0.00	$8.34 \times 10^{+02}$

methodologies.

The $F_{10.7}$ data in Figures 4.18 and 4.20 demonstrates that during the solar maximum, ionospheric irregularities were both longer-lasting and more intense compared to the solar minimum. This is because the upper ionosphere generates more plasma during periods of intense EUV and X-ray radiation from the Sun, which are stronger during the solar maximum (KIRCHHOFF, 1991; SEEBER, 2003; KELLEY, 2008; SCHUNK; NAGY, 2009; REZENDE *et al.*, 2010; SUBIRANA *et al.*, 2013; CHERNIAK *et al.*, 2014). Farley et al (1970) showed that ionospheric irregularities were more frequent during solar maximum and largely absent during solar minimum, based on data from a VHF incoherent scatter radar in Jicamarca (dip = 2°N), Peru in the 1960s. Similarly, Secan et al. (1995) found that the percentage of ionospheric scintillation increases with the sunspot number, peaking during the solar maximum. A well-known study by Pi et al. (1997) confirmed that strong ionospheric irregularities are more prevalent near the solar maximum.

Figure 4.20 shows that while ionospheric irregularities occur throughout the solar cycle, their duration and intensity vary. This is supported by research from Abdu et al. (2003) and Rezende et al. (2010), which used ionosonde data to demonstrate that ionospheric irregularities tend to begin 1-2 hours earlier during solar maximum compared to solar minimum. Das et al. (2003) observed that the occurrence of scintillations in the L and VHF bands was controlled by solar activity. Later, a study by Li et al. (2020) using data from nine GNSS receivers in Hong Kong (geomagnetic latitude ∼12.5°N) between 2013 and 2019, confirmed that plasma bubbles are more frequent during the solar maxi-

TABLE 4.4 – Estimated coefficients for a model that employs the *probit* link function and the two factor K_p model (Equation 4.1). The symbol * indicates parameters that fail the z-test.

	Estimate	Std. Error	z value	P-value(>|z|)
β_0	-3.34	0.04	-92.47	0.00
$\beta_{K_{p.AS}}$	0.23	0.10	2.17	0.03
$\beta_{F_{10.7}r}$	1.49	0.12	12.65	0.00
β_{EASr}	2.64	0.04	63.53	0.00
β_{TLSr}	-0.28	0.06	-4.90	0.00
$\beta_{K_{p.AS}:F_{10.7}r}$	-1.03	0.34	-3.03	0.00
$^*\beta_{K_{p.AS}:EASr}$	-0.19	0.13	-1.52	0.13
$\beta_{EASr:F_{10.7}r}$	2.36	0.14	17.05	0.00
$\beta_{K_{p.AS}:TLSr}$	0.32	0.14	2.27	0.02
$\beta_{TLSr:F_{10.7}r}$	0.42	0.17	2.46	0.01
$\beta_{EASr:TLSr}$	-0.47	0.07	-7.09	0.00
$^*\beta_{K_{p.AS}:F_{10.7}r:EASr}$	0.50	0.42	1.17	0.24
$^*\beta_{K_{p.AS}:F_{10.7}r:TLSr}$	-0.09	0.42	-0.21	0.83
$^*\beta_{K_{p.AS}:EASr:TLSr}$	-0.23	0.17	-1.31	0.19
$\beta_{F_{10.7}r:EASr:TLSr}$	-1.91	0.20	-9.65	0.00
$^*\beta_{K_{p.AS}:F_{10.7}r:EASr:TLSr}$	0.40	0.52	0.76	0.45

TABLE 4.5 – FNR, FPR and AUC-ROC for all models, using the median of $\hat{p}$ as the classification threshold. The statistics were calculated for both test data (.te) and training data (.tr). The optimal values are highlighted in bold.

	Models	Link Function	FNR.tr (%)	FNR.te (%)	FPR.tr (%)	FPR.te (%)	AUC-ROC.tr (%)	AUC-ROC.te (%)
1	$K_p^1 * F_{10.7}r * EASr * TLSr$	lo	0.53	0.58	43.92	43.91	77.77	77.75
2	$K_p^2 * F_{10.7}r * EASr * TLSr$	lo	0.59	0.63	43.93	43.92	77.74	77.72
3	$K_p^1 * F_{10.7}r * EASr * TLSr$	pr	**0.36**	**0.31**	**43.90**	**43.88**	**77.87**	**77.90**
4	$K_p^2 * F_{10.7}r * EASr * TLSr$	pr	**0.36**	0.32	**43.90**	**43.88**	**77.87**	77.89
5	$K_p^1 * F_{10.7}r * EASr * TLSr$	ca	1.86	1.68	44.08	44.05	77.02	77.13
6	$K_p^2 * F_{10.7}r * EASr * TLSr$	ca	1.85	1.68	44.08	44.05	77.03	77.13
7	$K_p^1 * F_{10.7}r * EASr * TLSr$	cl	0.79	0.80	43.95	43.94	77.62	77.62
8	$K_p^2 * F_{10.7}r * EASr * TLSr$	cl	0.82	0.87	43.95	43.95	77.61	77.58

mum. These findings align with those of Mendillo et al. (2000), who reported maximum occurrences of ESF in the Brazilian sector from September to March, another indicator of ionospheric irregularities at low latitudes (KIL, 2015). A broad study by Gentile et al. (2006) based on Defense Meteorological Satellite Program (DMSP) data from 1989–2004 corroborated these results. In summary, these studies consistently show that ionospheric irregularities are more frequent in low latitudes during the solar maximum, with $F_{10.7}$ serving as a useful predictor variable.

Figure 4.20 also shows a clear dependence of high ROTI values on local time. Local time – and, by extension, the *TLS* – has been correlated with ionospheric irregularities, as first demonstrated by Farley et al. (1970) in their study of (*ESF*). Pi et al. (1997) also observed these irregularities by analyzing the ROTI from GPS receivers in Kourou (5.3°N, 307.2°E, dip = 11.9°N), French Guiana on January 31, 1993, and in Are-

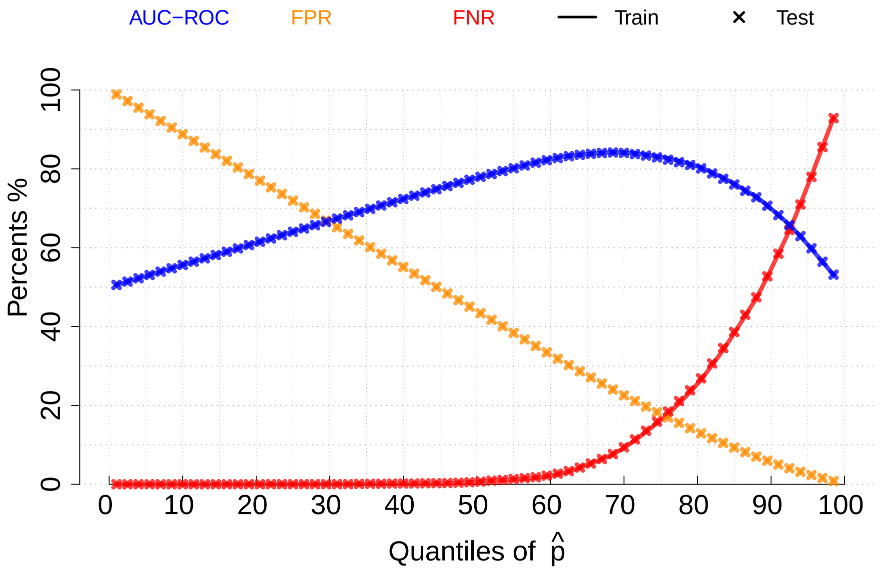

FIGURE 4.23 – FNR, FPR and AUC-ROC evaluated using test (x) and training (-) data as functions of the quantile values for the model described in Equation 4.1. Note that the results for both the training and test data overlap, indicating a good fit for this model. Additionally, when using quantiles of $\hat{p}$ below 76^{th} as a threshold, the FPR exceeds the FNR. Conversely, for quantiles above 76^{th}, the behavior is reversed. This indicates that, in the first scenario (quantiles of $\hat{p}$ below 76^{th}), all irregular ionospheric conditions are correctly predicted; however, the number of false positives is significantly high. In the second scenario (quantiles of $\hat{p}$ above 76^{th}), the number of false positives decreases, but the model's ability to predict irregular ionospheric conditions is compromised.

quipa (16.5°S, 288.5°E, dip = 3.35°S), Peru on September 17, 1995. They noted that ionospheric irregularities occurred at the onset of nighttime, indicating strong phase fluctuations or deep spatial gradients in TEC along the line of sight (AOL *et al.*, 2020). Later, Abdu (2001) highlighted that ESF and plasma bubbles tend to develop around 19:00 LT. Similarly, a 2003 study showed that in the Indian sector (10-30°N, 75-80°E, dip = 5-30°N) during February 1980, plasma bubbles formed around 19:00-20:00 LT (DABAS *et al.*, 2003). Given that Cachoeira Paulista (inclination of -28°) has a similar inclination to Brasília (inclination of approximately -25°), it was expected that irregularities would begin around 19:00 LT during solar maximum (ABDU *et al.*, 2003), which aligns with the behavior observed in Figure 4.20. Das et al. (2010) found that ionospheric scintillation tends to begin around 21:00 LT and diminish near midnight. Several authors (HARGREAVES, 1995; MENDILLO *et al.*, 2000; SEEBER, 2003; KELLEY, 2008; SCHUNK; NAGY, 2009) have demonstrated that plasma bubbles form at the beginning of the nighttime and persist past midnight (PEREIRA; CAMARGO, 2013). Therefore, *TLS* can be considered a predictor of ionospheric irregularities at low latitudes, providing an explanation for the well-known nighttime variability. However, as will be discussed, the relationship between the probability of irregularity occurrence and *TLS* may exhibit non-linearity.

The seasonal variation in ROTI values is clearly shown in Figure 4.20, where values fluctuate throughout the year, with higher values occurring between the equinoxes, including summer, and lower values in winter. The seasonality of ionospheric irregularities was highlighted by Farley et al. (1970) and Hargreaves (1995). The study by Secan et al. (1995), which enhanced the WBMOD model, also demonstrated that ionospheric scintillation is more likely to occur near the equinoxes in the Brazilian sector. Abdu (2001) noted that in Jicamarca, Peru (during 1968–1992), the strongest ionospheric irregularities observed using VHF incoherent scatter radar occurred from September to April. Further work by Abdu et al. (2003) showed that ionospheric irregularities tend to occur approximately from August to April during the solar minimum and from July to March during the solar maximum in Fortaleza, Brazil. The same was reported for Cachoeira Paulista, Brazil. Das et al. (2010) found that ionospheric scintillation is more prevalent during the equinoxes, with solstitial behavior depending on longitude. They also noted that scintillation is more frequent during the February–April equinox, a phenomenon known as equinoctial asymmetry, likely due to the Sun's higher elevation during that period (as shown in Figure 4.17). Pereira and Camargo (2013) observed that the TEC peak primarily occurred in May, April, September and October. Similarly, Li et al. (2020) reported that plasma bubbles were most frequent during the equinox season in their study, and Aol et. al. (2020) added the period of December solstice. The increased occurrence of ionospheric irregularities near the equinoxes is attributed to the alignment between the site's declination and the solar terminator, which enhances the likelihood of these irregularities (ABDU *et al.*, 1992). The clear seasonal dependence suggests that the variable EAS is a relevant predictor of ionospheric irregularities (WOOD *et al.*, 2024) in low-latitude regions.

4.2.5 Model Results

Table 4.3 shows that during periods of *Quiet* magnetosphere, certain variables either increase or decrease the probability of observing ionospheric irregularities. Note in the last column of Table 4.3 the signal of the exponents of 10, where positive exponents indicate an increase in the odds of irregular ionospheric conditions, while negative exponents signify a decrease in the odds. These coefficients quantify the influence of each independent variable on the likelihood of irregularities, providing insights into their respective contributions to the model's predictions. This differentiation is critical for understanding the dynamics of the ionosphere and refining the predictive accuracy of the model. It is important to consider that the variables were normalized, which influences the interpretation of the parameter values. The results indicate that the odds of observing irregular ionospheric conditions increase with season ($EASr$) and solar activity ($F_{10.7}r$), with the former having a greater impact than the latter. Additionally, some interaction terms, such as solar cycle and hour of night ($TLSr : F_{10.7}r$) and season and hour of night ($EASr : TLSr$), also increase the odds, with the former being more significant. Conversely, other parameters reduce the odds. In the case of non-interaction terms, the odds decrease for $TLSr$, while for interaction terms, the odds decrease for season and solar cycle ($EASr : F_{10.7}r$), as well as for hour of night, solar cycle and season $F_{10.7}r : EASr : TLSr$. Notably, the parameter associated with $TLSr$ alone reduces the odds, contrary to what was initially expected. This is due to the non-linear relationship between $TLSr$ and the probability of observing high ROTI values, where low ROTI values occur at the beginning and end of the night and higher values occur between 20:00 and 00:00 LT, as shown in Figure 4.20. Physically, this behavior can be explained by the fact that the ionospheric irregularities associated with the EPB originate at magnetic latitudes near the magnetic equator and take time to propagate to Brazília's station, located within the Appleton Anomaly region. Consequently, these irregularities are generated shortly after sunset but typically appear over Brasília approximately two hours later.

During periods of an *Active-Storm* magnetosphere, variables may either increase or decrease the odds of observing ionospheric irregularities. Table 4.3 shows that the odds of observing such irregularities increase for the single variable $TLSr$ and for the interaction terms $EASr : F_{10.7}$ and $F_{10.7}r : EASr : TLSr$. Conversely, the odds decrease for the single variables $F_{10.7}r$ and $EASr$, as well as for the interaction terms $EASr : TLSr$ and $TLSr : F_{10.7}r$. The reduction in odds for $F_{10.7}r$ and $EASr$ can be attributed to a slight relaxation in the criteria for high solar activity or summer season needed for the occurrence of irregularities.

Analyzing the intercept, we observe that the odds were higher during *Active-Storm* magnetosphere periods ($-8.82 > -10.33$), consistent with the expectation that irregularities are more likely during magnetic storms. The odds of irregularity occurrence at the start of the nighttime also increased under *Active-Storm* conditions ($-5.95 > -8.81$). However, the odds associated with the solar cycle ($8.6 > 3.8$) and season ($9.10 > 7.85$) decreased, as mentioned previously. These results indicate that, during *Active-Storm* periods, the development of ionospheric irregularities is significantly influenced by geomagnetic storms or substorms, as expected.

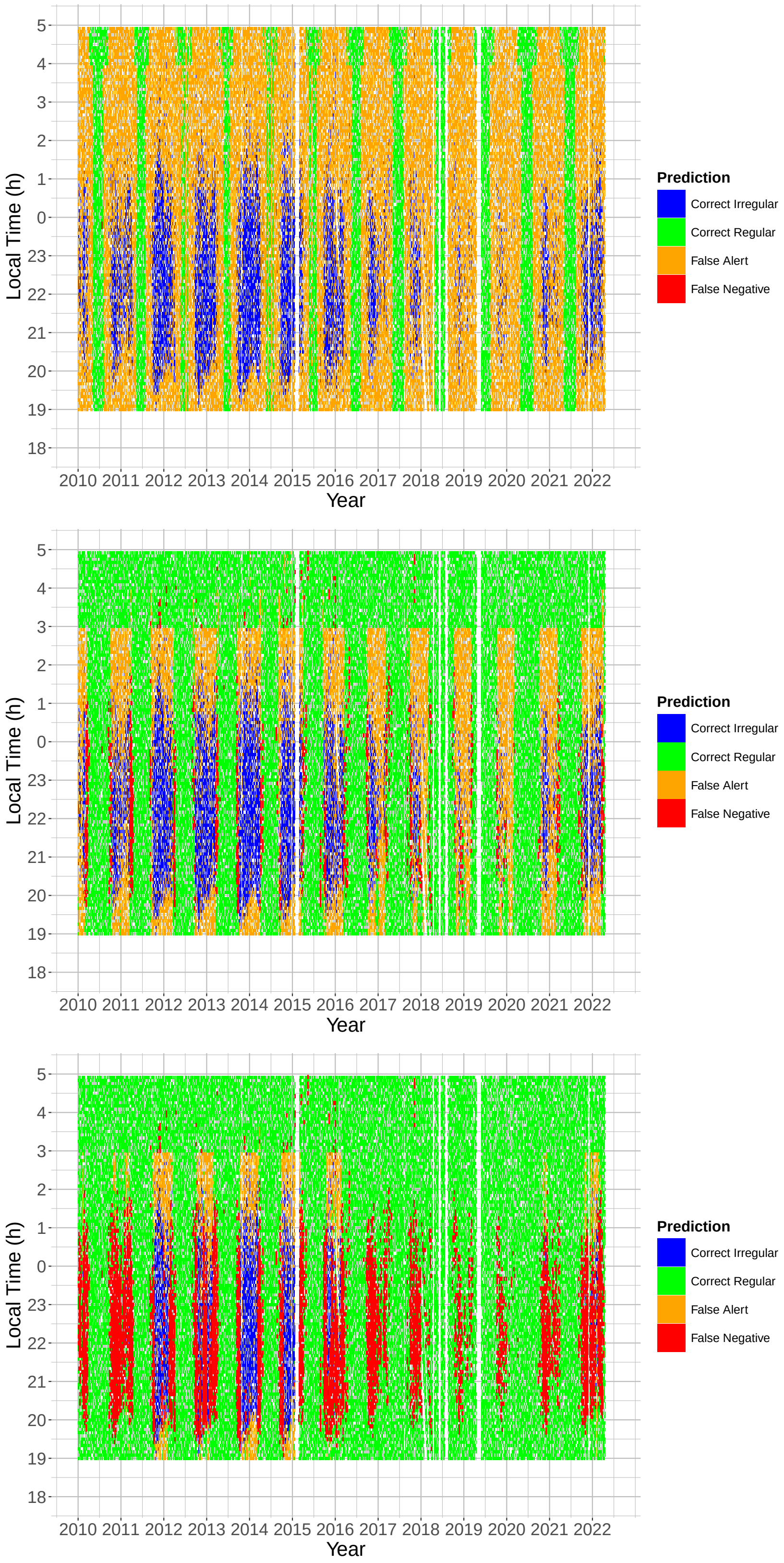

FIGURE 4.24 – Prediction of the ionospheric state in the testing data (that are the 30% - random sample from the all data) by model 4 (Table 4.5), with different thresholds: 25^{th} (top), 70^{th} (center) and 90^{th} (bottom) quantiles of $\hat{p}$.

The overall performance of Model 4 is summarized in Table 4.5 and illustrated in Figure 4.24. The figure highlights the trade-off between sensitivity and specificity and provides insights into the specific conditions where the model fails. In general, model 4 tends to perform better when the solar cycle is near its peak, during summer and winter, and in the hours close to midnight (Figure 4.20). As the selection threshold is increased from the 25^{th} to the 90^{th} percentile, there is a noticeable rise in false negatives, since models with a higher threshold becomes more stringent in classifying the ionosphere as irregular. A pattern emerges where misclassification of true positives first appears during the transition between the equinoxes and winter. This suggests a possible shift between the period of maximum probability and maximum EAS, likely influenced by Earth's magnetic field declination. False positives also show a clear pattern, with most erroneous predictions occurring at the beginning of the night and between 00:00 LT and 03:00 LT. This reinforces the previously noted non-linearity in the relationship between the probability of observing ionospheric irregularities and the TLS variable. These error patterns suggest potential areas for model improvement.

Next, the present work is placed in perspective relative to other works. In a study by Abdu et al. (2003), cubic B-splines were used to model the probability of spread F occurrence. While the model showed good agreement with empirical data, it did not include data from disturbed magnetospheric conditions and the coefficients from the methodology were not used for interpreting the results. Another study by Rezende et al. (REZENDE *et al.*, 2010) achieved a 95.5% correct classification rate. The decision tree methodology they employed is effective for interpreting parameters with the data, though this aspect was not explored in the study. Moreover, their model only considered data from quiet periods. During the same period, Das et al. (2010) used a neural network to model the probability of ionospheric scintillation. Despite their results aligning with empirical data, the neural network required 250 neurons in the first layer and 31,000 iterations, which compromised the interpretability of the weights. Another study by Atabati et al. (2021), conducted in Guam (13.53°E, 144.86°N) across several seasons in 2015, 2017 and 2020, used variables such as F_2 layer height, vertical drift, solar flux ($F_{10.7}$), sunspot numbers and K_p to filter quiet periods. Neural networks and genetic algorithms were applied to predict ROTI and S_4, achieving 80% accuracy. The data was split into 80% for training and 20% for testing. However, their study lacked model interpretability and did not account for data during magnetospheric disturbances.

5 Conclusion

5.1 Gravity Waves

In this thesis, a variety of statistical methods were applied to study GWs in the TLS in the Brazilian sector, using a large database of radiosonde measurements. Some of these techniques were applied for the first time in this context, such as cluster analysis, spatial correlation analysis, gamma distribution fitting, least squares fitting with simultaneous harmonic and parabolic detrending, non-parametric moving central estimators to smooth temporal series and Spearman's correlation.

The wind cluster analysis showed how the prevailing winds at the standard times of radiosonde launches behave in the Brazilian territory as a function of latitude. To our knowledge, this is the first comprehensive study of GWs carried out in the Brazilian sector using radiosondes during one year in 32 aerodromes. The analysis of GWs showed how their average energy densities vary during the year. Monochromatic waves were identified, counted and characterized covering a large territorial area. The parameters of the monochromatic waves found in this work reproduced much of the results of the literature using the same methodology for other regions of the world. The most interesting result of this work, in our opinion, was the finding that there seems to be no or very weak correlation between GWs measured by radiosonde in the troposphere and the lower stratosphere. We also highlight the finding that the GWs quantities such as the kinetic and potential energy densities measured at a given location correlate with the same quantities measured in nearby locations within a radius of 3,000 km (troposphere) and 3,900 km (lower stratosphere). Also, based on this work, we discussed some limitations of the application of radiosonde measurements to the problem of the origin of GWs observed in the mesosphere, where of the spectrum of GWs are totally different. Finally, we discussed the question of whether or not radiosonde measurements could provide useful information that relates to the initial perturbations in the higher atmosphere that trigger EPBs.

The dataset used in this study and the code that implements the gravity wave output is available in GitHub's repository (BRHIAN, 2023). The data from other years are available upon request by *Instituto de Controle do Espaço Aéreo (ICEA)* or in the site `https:`

`//www.icea.decea.mil.br/`.

5.2 Ionophere

Beyond the exploration of GWs, this work extended its scope to address a separate yet critical topic: forecasting the ionospheric state using advanced statistical modeling. This study successfully developed a model that provides accurate forecasts of the ionospheric state at a single station using four key variables. By employing quantiles as thresholds, the performance of the model was generalized across different ranges of the prediction distribution of $\hat{p}$. The best-performing model, chosen by using the median of $\hat{p}$ as the threshold value, was model 4 (Table 4.3), which takes into account all the key predictor variables with a *probit* link function and a binary factor variable to account for storm conditions – the values of its coefficients are shown in the Table 4.4. Both sensitivity and specificity reached approximately 82% when the threshold was set at the 76^{th} quantile, as shown in Figure 4.23. Below this quantile, sensitivity was higher than specificity; beyond this point, specificity became the dominant metric. Alternatively, the optimal threshold may be defined as the optimal AUC-ROC value. Using this criterion, the threshold was found near the 69^{th} quantile, where the sensitivity was 91% and the specificity 78%. These findings underscore the need for careful interpretation of model predictions, especially by operators who will use the model for practical purposes.

A similar model, but using a *logit* link function, displayed performance comparable to the probit model but offered greater interpretability by quantifying how each variable influenced the odds of ionospheric irregularities. The analysis revealed that the odds of observing irregular ionospheric conditions increased with the maximum elevation angle of the Sun and solar activity ($F_{10.7}$), the former exerting a stronger effect. Interestingly, the TLS parameter alone was found to reduce the odds, contrary to initial expectations. This outcome is explained by the non-linear relationship between TLS and the probability of observing high ROTI values. Lower ROTI values are found at both the beginning and the end of the night, whereas higher values are observed between 20:00 and 00:00 LT, as illustrated in Figure 4.20. During Active-Storm periods, variables like $F_{10.7}$ and EAS may either increase or decrease the odds of irregularities, as discussed earlier. The reduction in odds during these periods reflects an increased probability of observing irregularities outside the typical conditions associated with solar activity or season. As expected, the intercept of the model, combined with the effect of TLS during Active-Storm conditions, highlights the strong influence of geomagnetic storms or substorms on the development of ionospheric irregularities.

These linear models, incorporating interactions between solar cycles, time of the day, seasons and magnetospheric conditions, offer valuable insights into ionospheric behavior. Future improvements could focus on better modeling the non-linear relationship between the TLS variable and ROTI values, where high ROTI increases sharply until 21:00 LT and decreases gradually after midnight (see Figure 4.20). Furthermore, inspired by the work of Goncharenko et al. (2021) and Wood et al. (WOOD *et al.*, 2024), the current model could be enhanced by modulating time variables with harmonic functions, selecting alternative explanatory variables to model the solar cycle and geomagnetic storms, and incorporating delayed variables. Similarly, the EAS variable could be refined, as its non-linear relationship with ROTI peaks near the September equinox and gradually diminishes until the March equinox – according to Figure 4.20.

The model presented here serves as an effective alert system for ionospheric conditions at the *braz* station, helping users anticipate potential disruptions to GNSS devices and motivating the use in other stations. It is the first model to use 12 years of data from a Brazilian station and to incorporate the magnetospheric state, represented by the K_p index, as a predictor of equatorial ionospheric irregularities. Future research could expand this approach to create a global model by applying it across multiple stations with similar data sets and including other inputs related to magnetospheric behavior such as Aurora Eletrojet Index (AE), plasma density (n), solar wind velocity, and magnetic field component (B_z), for example.

Bibliography

AA, E. *et al.* Significant midlatitude bubble-like ionospheric super-depletion structure (BLISS) and dynamic variation of storm-enhanced density plume during the 23 april 2023 geomagnetic storm. **Space Weather**, v. 22, n. e2023SW003704, p. 1 – 18, 2024. Disponível em: https://doi.org/10.1029/2023SW003704.

ABDU, M. Outstanding problems in the equatorial ionosphere–thermosphere electrodynamics relevant to spread F. **Journal of Atmospheric and Solar-Terrestrial Physics**, v. 63, n. 9, p. 869–884, 2001. Disponível em: https://doi.org/10.1016/S1364-6826(00)00201-7.

ABDU, M. Equatorial f region irregularities. *In*: **The Dynamical Ionosphere**. Elsevier, 2020. p. 169–178. Disponível em: https://doi.org/10.1016/B978-0-12-814782-5.00012-1.

ABDU, M.; BATISTA, I.; SOBRAL, J. A new aspect of magnetic declination control of equatorial spread F and F region dynamo. **Jornal of Geophysical Research: Space Physics**, v. 97, n. A10, p. 14897–14904, 1992. Disponível em: https://doi.org/10.1029/92JA00826.

ABDU, M.; SOUZA, J.; BATISTA I. SOBRAL, J. Equatorial spread F statistics and empirical representation for IRI: A regional model for the Brazilian longitude sector. **Advances in Space Research**, v. 31, n. 3, p. 703–716, 2003. Disponível em: https://doi.org/10.1016/S0273-1177(03)00031-0.

ABREU, A.; CORREIA, E.; JESUS, R.; VENKATESH, K.; MACHO, E.; ROBERTO, M.; FAGUNDES, P.; GENDE, M. Statistical analysis on the ionospheric response over south american midand near high-latitudes during 70 intense geomagnetic storms occurred in the period of two decades. **Journal of Atmospheric and Solar-Terrestrial Physics**, v. 245, p. 1–13, 2023. Disponível em: https://doi.org/10.1016/j.jastp.2023.106060.

ABREU, A.; SAHAI, Y.; FAGUNDES, P.; BEKER-GUEDES, F.; JESUS, R.; GUARNIEI, F.; PILLAT, V. Response of the ionospheric F-region in the Brazilian sector during the super geomagnetic storm in April 2000 observed by GPS. **Advances in Space Research**, v. 45, n. 11, p. 1322–1329, 2010. Disponível em: https://doi.org/10.1016/j.asr.2010.02.003.

AHRENS, C.; HENSON, R. **Meteorology today, An Introduction to Weather, climate, and the environment**. 12th. ed. [*S.l.*]: Cengage, 2018.

ALEXANDER, M. Interpretations of observed climatological patterns in stratospheric gravity wave variance. **Journal of Geophysical Research: Atmospheres**, Wiley Online Library, v. 103, n. D8, p. 8627–8640, 1998.

ALEXANDER, M.; GELLER, M.; MCLANDRESS, C.; POLAVARAPU, S.; PREUSSE, P.; SASSI, F.; SATO, K.; ECKERMANN, S.; ERN, M.; HERTZOG, A.; KAWATANI, Y.; PULIDO, M.; SHAW, T. A.; SIGMOND, M.; VINCENT, R.; WATANABE, S. Recent developments in gravity-wave effects in climate models and the global distribution of gravity-wave momentum flux from observations and models. **Royal Meteorological Society**, v. 136, n. 650, p. 1103–1124, 2010. Disponível em: https://doi.org/10.1002/qj.637.

ALLEN, S.; VINCENT, R. Gravity wave activity in the low atmosphere: seasonal and latitudinal variations. **Jornal of Geophysical Research**, v. 100, p. 1327–1350, 1995. Disponível em: https://doi.org/10.1029/94JD02688.

AMORIM, D.; PIMENTA, A.; ALMEIDA, A. Characterization of medium-scale traveling ionospheric disturbances in the brazilian low latitude sector - statistical analysis of all-sky images of oi 630 nm airglow emission. **Brazilian Journal of Geophysics**, v. 30, n. 2, p. 129–136, 2012. Disponível em: https://doi.org/10.22564/rbgf.v30i2.86.

AMORIM, D.; PIMENTA, A.; BITTENCOURT, J.; FAGUNDES, P. Long-term study of medium-scale traveling ionospheric disturbances using oi 630 nm all-sky imaging and ionosonde over brazilian low latitudes. **Jornal of Geophysical Research**, v. 116, n. A06312, 2011. Disponível em: https://doi.org/10.1029/2010JA016090.

AOL, S.; BUCHERT, S.; JURUA, E. Traits of sub-kilometre F-region irregularities as seen with the Swarm satellites. **Annales Geophysicae**, v. 38, p. 243–261, 2020. Disponível em: https://doi.org/10.3390/rs14010010.

ARCE, G. **Nonlinear signal processing: A statistical approach**. 1st. ed. [*S.l.*]: Wiley, 2005.

ARCHER, C.; CALDEIRA, K. Historical trends in the jet streams. **Geophysical Research Letters**, v. 35, n. 8, 2008. Disponível em: https://doi.org/10.1029/2008gl033614.

ARMITAGE, P. Tests for linear trends in proportions and frequencies. **Biometrics**, JSTOR, v. 11, n. 3, p. 375–386, 1955.

ASTAFYEVA, E. Ionospheric detection of natural hazards. **Reviews of Geophysics**, v. 57, p. 1256–1288, 2019. Disponível em: https://doi.org/10.1029/2019RG000668.

ATABATI, A.; ALIZADEH, M.; SCHUH, H.; TSAI, L. Ionospheric scintillation prediction on S4 and ROTI parameters using Artificial Neural Network and Genetic Algorithm. **Remote Sensing**, v. 2092, n. 13, p. 1–18, 2021. Disponível em: https://doi.org/10.3390/rs13112092.

AYORINDE, T.; WRASSE, C.; TAKAHASHI, H.; BARROS, D.; FIGUEIREDO, C.; LOMOTEY, S.; ESSIEN, P.; BILIBIO, A. Stratospheric gravity wave potential energy and tropospheric parameters relationships over South America: a study using

COSMIC-2 and METOP radio occultation measurements. **Earth, Planets and Space**, v. 75, n. 136, p. 1–19, 2023. Disponível em: https://doi.org/10.1186/s40623-023-01891-8.

AYORINDE, T.; WRASSE, C.; TAKAHASHI, H.; BARROS, D.; FIGUEIREDO, C.; SILVA, L.; BILIBIO, A. Investigation of the long-term variation of gravity waves over South America using empirical orthogonal function analysis. **Earth, Planets and Space**, v. 76, n. 105, p. 1–19, 2024. Disponível em: https://doi.org/10.1186/s40623-024-02045-0.

AZEEM, I.; YUE, J.; HOFFMANN, L.; MILLER, S.; STRAKA III, W.; CROWLEY, G. Multisensor profiling of a concentric gravity wave event propagating from the troposphere to the ionosphere. **Geophysical Research Letters**, v. 42, p. 7874–7880, 2015. Disponível em: https://doi.org/10.1002/2015GL065903.

AZPILICUETA, F.; NAVA, B. Studying the winter anomaly with altimeter-derived tec data. **Advances in Space Research**, v. 68, n. 8, 2021. Disponível em: https://doi.org/10.1016/j.asr.2021.06.008.

BAGDONAVICIUS, V.; KRUOPIS, J.; NIKULIN, M. **Non-parametric Test for Complete Data**. 1st. ed. [*S.l.*]: Wiley, 2011.

BALAN, N.; BAILEY, G.; ABDU, M.; OYAMA, K.; RICHARD, P.; MACDOUGALL, J.; BATISTA, I. Equatorial plasma fountain and its effects over three locations: Evidence for an additional layer, the F3 layer. **Space Physics**, v. 102, n. A2, p. 2047–2056, 1997. Disponível em: https://doi.org/10.1029/95JA02639.

BATISTA, I.; ABDU, M.; SILVA, A.; SOUZA, J. Ionospheric f_3 layer: Implications for the IRI model. **Advances in Space Research**, Elsevier, v. 31, n. 3, p. 607–611, 2003.

BAUER, S. A possible troposphere-ionosphere relationship. **Jornal of Geophysical Research**, v. 62, n. 3, p. 425–430, 1957. Disponível em: https://doi.org/10.1590/1806-9126-RBEF-2016-0027.

BERKNER, L.; WELLS, H. F-region ionosphere-investigations at low latitudes. **Terrestrial Magnetism and Atmospheric Electricity**, Wiley Online Library, v. 39, n. 3, p. 215–230, 1934.

BISHARA, A.; HITTNER, J. Testing the significance of a correlation with nonnormal data: Comparison of Pearson, Spearman, transformation, and resampling approaches. **Psychological Methods**, v. 17, n. 3, 2012. Disponível em: https://doi.org/10.1037/a0028087.

BRASIL. **Ministério da Defesa. Comando da Aeronáutica. Departamento de Controle de Espaço e Controle Aéreo. Procedimentos operacionais referentes ao lançamento de balão meteorológico. CIRCEA 63-3**. [*S.l.*], 2013.

BRASIL. **Coordenação MET/ATS referente ao lançamento de balão meteorológico**. [*S.l.*], 2017.

BRASIL. **Manual de Meteorologia e Oceanografia de Defesa**. [*S.l.*], 2020.

BRASIL. **Manual de Estações Meteorológicas de Altitude**. [*S.l.*], 2022. Accessed at `https://publicacoes.decea.mil.br/api/storage/uploads/files/1646240383-mca-105-9-em-vigor-2-de-marco.pdf`.

BRASIL. **Relatório de Informação de Estação - BRAZ**. [*S.l.*], 2023.

BRASIL. **Relatório de Estação Geodésica - BRAZ**. [*S.l.*], 2024.

BRHIAN, A. **a-brhian/GW_article: DOI**. [Software] with [Dataset]. Zenodo, 2023. Disponível em: https://doi.org/10.5281/ZENODO.8349770.

BRHIAN, A.; RIDENTI, M.; ROBERTO, M.; ABREU, A.; GUEDE, J.; CAMPOS, E. A survey on gravity waves in the brazilian sector based on radiosonde measurements from 32 aerodromes. **Jornal of Geophysical Research: Atmospheres**, v. 129, n. 7, p. e2023JD039811, 2024. Disponível em: https://doi.org/10.1029/2023JD039811.

BRITISH GEOLOGICAL SURVEY. **Geomagnetic Activity Levels**. 2024. Accessed: 2024-07-30. Disponível em: https://geomag.bgs.ac.uk/education/activitylevels.html.

BRUMMELEN, G. **Heavenly Mathematics: The forgotten art of spherical trigonometry**. 1st. ed. [*S.l.*]: Princeton University Press, 2013.

CAMPBELL, W. **Introduction to Geomagnetic Fields**. 2nd. ed. [*S.l.*]: Cambridge, 2003.

CARMO, C.; DENARDINI, C.; FIGUEIREDO, C.; RESENDE, L.; PICANÇO, G.; BARBOSA NETO, P. Evaluation of different methods for calculating the ROTI index over the Brazilian sector. **Radio Science**, v. 56, p. 1–12, 2021. Disponível em: https://doi.org/10.1029/2020RS007140.

CARMO, C.; PI, X.; DENARDINI, C. M.; FIGUEIREDO, C. A. O. B.; VERKHOGLYADOVA, O. P.; PICANçO, G. A. S. Equatorial plasma bubbles observed at dawn and after sunrise over South America during the 2015 St. Patrick's Day storm. **Journal of Geophysical Research: Space Physics**, v. 127, p. e2021JA029934, 2022. Disponível em: https://doi.org/10.1029/2021JA029934.

CHERNIAK, I.; KRANKOWSKI; ZAKHARENKOVA, I. Observation of the ionospheric irregularities over the northern hemisphere: Methodology and service. **Radio Scieince**, v. 49, p. 653–662, 2014. Disponível em: https://doi.org/10.1002/2014RS005433.

CHERNIAK, I.; ZAKHARENKOVA, I.; REDMON, R. Dynamics of the high-latitude ionospheric irregularities during the 17 march 2015 st. patrick's day storm: Ground-based gps measurements. **Space Weather**, v. 13, p. 585–597, 2015. Disponível em: https://doi.org/10.1002/2015SW001237.

CHIAN, A.; ABALDE, J.; MIRANDA, R.; BOROTTO, F.; HYSELL, D.; REMPEL, E.; RUFFOLO, D. Multi-spectral optical imaging of the spatiotemporal dynamics of ionosphere intermittent turbulence. **Scientific Reports**, v. 8, n. 10568, p. 1–15, 2018. Disponível em: https://doi.org/10.1038/s41598-018-28780-5.

CHOCHRAN, W. Some methods for strengthening the common chi-squared tests. **Biometrics**, v. 10, n. 4, p. 417–451, 1954.

COWPERTWAIT, P.; METCALFE, A. **Introductory Time Series with R**. 1st. ed. [*S.l.*]: Springer, 2009.

DABAS, R.; SINGH, L.; LAKSHMI, D.; SUBRAMANYAM, P.; CHOPRA, P.; GARG, S. Evolution and dynamics of equatorial plasma bubbles: Relationships to ExB drift, postsunset total electron content enhancements, and equatorial electrojet strength. **Radio Science**, v. 38, n. 4, p. 1–11, 2003. Disponível em: https://doi.org/10.1029/2001RS002586.

DABBERDT, W. F.; TURTIAINEN, H. Radiosondes. *In*: NORTH, G. R.; PYLE, J.; ZHANG, F. (Ed.). **Encyclopedia of Atmospheric Sciences (Second Edition)**. Second edition. Oxford: Academic Press, 2015. v. 4, p. 273–284. ISBN 978-0-12-382225-3. Disponível em: https://doi.org/10.1016/B978-0-12-382225-3.00344-3.

DARDARI, D.; FALLETI, E.; LUISE, M. (Ed.). **Satellite and Terrestrial Radio Positioning Techniques**. 1st. ed. [*S.l.*]: Elsevier, 2012. ISBN 978-0-12-382084-6.

DARE-IDOWU, O.; PAULINO, I.; FIGUEIREDO, C. A.; MEDEIROS, A. F.; BURITI, R. A.; PAULINO, A. R.; WRASSE, C. M. Investigation of sources of gravity waves observed in the brazilian equatorial region on 8 april 2005. *In*: COPERNICUS PUBLICATIONS GÖTTINGEN, GERMANY. **Annales Geophysicae. Proceedings** [...]. [*S.l.: s.n.*], 2020. v. 38, n. 2, p. 507–516.

DAS, A.; GUPTA, A. D.; RAY, S. Characteristics of L-band (1.5 ghz) and VHF (244 mhz) amplitude scintillations recorded at Kolkata during 1996–2006 and development of models for the occurrence probability of scintillations using neural network. **Journal of Atmospheric and Solar-Terrestrial Physics**, v. 72, n. 9-10, p. 685–704, 2010. Disponível em: https://doi.org/10.1016/j.jastp.2010.03.010.

DATTA-BARUA, S.; ALTSHULER, E.; WALTER, T.; PULLEN, S. ionospheric scintillation effects on satellite navigation. *In*: HUANG, C.; LU, G. (Ed.). **Space Physics and Aeronomy Collection Volume 3: Ionosphere Dynamics and Applications**. Jonh Wiley & Sons, 2021. p. 493–510. Disponível em: https://doi.org/10.1002/9781119815617.ch20.

DEVORE, J. **Probability and statistics: for engineering and the sciences**. 9th. ed. [*S.l.*]: Cengage, 2016.

DOBSON, A.; BARNETT, A. **An introduction to Generalized Linear Models**. 4th. ed. [*S.l.*]: CRC Press, 2018.

DUNGEY, J. Convective diffusion in the equatorial f region. **Journal of Atmospheric and Terrestrial Solar**, v. 9, 1956. Disponível em: https://doi.org/10.1016/0021-9169(56)90148-9.

EMMERT J.AND RICHMOND, A.; DROB, D. A computationally compact representation of magnetic-apex and quasi-dipole coordinates with smooth base vectors. **Jornal of Geophysical Research**, v. 115, p. A08322, 2010. Disponível em: https://doi.org/10.1029/2010JA015326.

FAGUNDES, P.; ABALDE, J.; BITTENCOURT J. SAHAI, Y.; FRANCISCO, R.; PILLAT, V.; LIMA, W. F layer postsunset height rise due to electric field prereversal enhancement: 2. traveling planetary wave ionospheric disturbances and their role on the generation of equatorial spread f. **Jornal of Geophysical Research**, v. 114, n. A12322, 2009. Disponível em: https://doi.org/10.1029/2009JA014482.

FAGUNDES, P.; BITTENCOURT, J.; ABALDE, J.; SAHAI, Y.; BOLZAN, M.; PILLAT, V.; LIMA, W. F layer postsunset height rise due to electric field prereversal enhancement: 1. traveling planetary wave ionospheric disturbance effects. **Jornal of Geophysical Research**, v. 114, n. A12321, 2009. Disponível em: https://doi.org/10.1029/2009JA014390.

FAGUNDES, P.; MUELLA, M.; BITTENCOURT, J.; SAHAI, Y.; LIMA, W.; GUARNIERI, F.; BECKER-GUEDES, F.; PILLAT, V.; FERREIRA, A.; LIMA, N. Nighttime ionosphere-thermosphere coupling observed during an intense geomagnetic storm. **Advances in Spapce Research**, v. 41, p. 539–547, 2008. Disponível em: https://doi.org/10.1016/j.asr.2007.11.005.

FARAWAY, J. **Extending the Linear Model with R: Generalized Linear, Mixed Effects and Nonparametric Regression Models**. [*S.l.*]: CRC, 2006.

FARLEY, D.; BASLEY, B.; WOODMAN, R.; MCCURE, J. Equatorial Spread F: Implications of VHF radar observation. **Space Physics**, v. 75, n. 34, p. 7199–7216, 1970. Disponível em: https://doi.org/10.1029/JA075i034p07199.

FORBES, J. Tidal and planetary waves. **Reviews of Geophysics and Space Physics**, v. 17, p. 1951–1981, 1979. Disponível em: https://doi.org/10.1029/RG017i008p01951.

FORBES, J.; GARRET, H. Theoretical studies of atmosphereric tides. **Reviews of Geophysics and Space Physics**, v. 17, p. 1951–1981, 1979. Disponível em: https://doi.org/10.1029/RG017i008p01951.

FRITTS, D. Gravity wave saturation in the middle atmosphere: A review of theory and observation. **Reviews of Geophysics and Space Physics**, v. 22, p. 275–308, 1984. Disponível em: https://doi.org/10.1029/RG022i003p00275.

FRITTS, D.; ALEXANDER, M. Gravity wave dynamics and effects in the middle atmosphere. **Reviews of Geophysics**, v. 41, p. 1–64, 2003. Disponível em: https://doi.org/10.1029/2001RG000106.

GELLER, M.; GONG, J. Gravity wave kinetic, potential, and vertical fluctuation energies as indicators of different frequency gravity waves. **Journal of Geophysical Research**, v. 115, n. D11111, 2010. Disponível em: https://doi.org/10.1029/2009JD012266.

GENTILE, L.; BURKE, W.; RICH, F. A climatology of equatorial plasma bubbles from DMSP 1989–2004. **Radio Science**, AGU, v. 41, n. 05, p. 1–7, 2006.

GIBBONS, J.; CHAKRABORTI, S. **Nonparametric Statistical Inference**. 5th. ed. [*S.l.*]: CRC Press, 2011.

GILL, A. **Atmosphere-Ocean Dynamics**. 1st. ed. [*S.l.*]: Academic Press, 1982.

GIONGO, G.; BAGESTON, J.; FIGUEIREDO C. WRASSE, C.; KAM, H.; KIM, Y.; SCHUCH, N. Gravity wave investigations over comandante ferraz antarctic station in 2017: General characteristics, wind filtering and case study. **MDPI: Atmosphere**, v. 11, n. 880, 2020. Disponível em: https://doi.org/10.3390/atmos11080880.

GONCHARENKO, L.; TAMBURRI, C.; TOBISKA, W.; SCHONFELD, S.; CHAMBERLIN, P.; WOODS, T.; DIDKOVSKY, L.; COSTER, A.; ZHANG, S. A new model for ionospheric total electron content: The impact of solar flux proxies and indices. **Journal of Geophysical Research: Space Physics**, v. 126, p. e2020JA028466, 2021. Disponível em: https://doi.org/10.1029/2020JA028466.

GONG, J.; GELLER, M. A. Vertical fluctuation energy in united states high vertical resolution radiosonde data as an indicator of convective gravity wave sources. **Journal of Geophysical Research: Atmospheres**, Wiley Online Library, v. 115, n. D11, 2010.

GONZáLEZ, G. Storm-time variability of ionospheric irregularities over south america. **Journal of Atmospheric and Solar–Terrestrial Physics**, v. 241, n. 105980, p. 1–18, 2022. Disponível em: https://doi.org/10.1016/j.jastp.2022.105980.

GOSSARD, E.; HOOKE, W. **Waves in the atmosphere**. 1st. ed. [*S.l.*]: Elsevier, 1975.

HAIR, J.; BLACK, W.; BABIN, B.; ANDERSON, R.; TATHAN, R. **Multivariate data analysis**. 6th. ed. [*S.l.*]: Pearson, 2006.

HANLEY, J.; MCNEIL, B. The meaning and use of the Area Under a Receiver Operating Characteristic (ROC) Curve. **Radiology**, v. 143, p. 29–36, 1982.

HARGREAVES, J. **The solar-terrestrial environment**. 1st. ed. [*S.l.*]: Cambridge, 1995.

HARSHA, P.; RATNAM, D.; NAGASRI, M.; SRIDHAR, M.; RAJU, K. Kriging-based ionospheric tec, roti and aplitude scintillation index (s_4) maps for india. **IET Radar Sonar Navig.**, v. 14, n. 11, p. 1827–1836, 2020. Disponível em: https://doi.org/10.1049/iet-rsn.2020.0202.

HEALE, C.; BOSSERT, K.; VADAS, S.; HOFFMANN, L.; DöRNBRACK, A.; STOBER, G.; SNIVELY, J.; JACOBI, A. Secondary gravity waves generated by breaking mountain waves over europe. **JGR: Atmosphere**, v. 125, n. 5, 2020. Disponível em: https://doi.org/10.1029/2019JD031662.

HERRERA, E.; MORETT, S. On the direction of coriolis force and the angular momentum conservation. **RBEF**, v. 38, n. 3, p. 1–7, 2016. Disponível em: https://doi.org/10.1590/1806-9126-RBEF-2016-0027.

HINES, C. Internal atmospheric gravity waves at ionospheric heights. **Can. J. Phy.**, v. 38, p. 1441–1481, 1960. Disponível em: https://doi.org/10.1139/p60-150.

HINES, C. Gravity waves in the atmosphere. **Nature**, v. 239, 1972. Disponível em: https://doi.org/10.1038/239073a0.

HOFMANN-WELLENHOF, B.; LICHTENEGGER, H.; WASLE, E. **Systems: GPS, GLONASS, Galileu, and more**. 1st. ed. [*S.l.*]: Springer, 2008.

HOLTON, J. **The dynamic meteorology of the stratosphere and mesosphere**. [*S.l.*]: American Meteorological Society, 1975.

HOLTON, J. **An introduction to dynamic meteorology**. 4. ed. [*S.l.*]: Elsevier, 2004.

HOSKINS, B. J.; YANG, G.-Y. A global perspective on the upper branch of the Hadley cell. **Journal of Climate**, American Meteorological Society, Boston MA, USA, v. 36, n. 19, p. 6749 – 6762, 2023. Disponível em: https://doi.org/10.1175/JCLI-D-22-0537.1.

HUANG, C.; HELMBOLDT, J.; PARK, J.; PEDERSEN, T.; WILLERMANN, R. Ionospheric detection of explosive events. **Reviews of Geophysics**, v. 57, p. 78–105, 2019. Disponível em: https://doi.org/10.1029/2017RG000594.

HUBA, J. Theory and modeling of equatorial spread f. *In*: HUANG, C.; LU, G. (Ed.). **Space Physics and Aeronomy Collection Volume 3: Ionosphere Dynamics and Applications**. Jonh Wiley & Sons, 2021. p. 185–200. Disponível em: https://doi.org/10.1002/9781119815617.ch10.

HYSELL, D.; FANG, T.; FULLER-ROWELL, T. Modeling equatorial F-region ionospheric instability using a regional ionospheric irregularity model and WAM-IPE. **JGR Space Physics**, v. 127, n. 9, p. 1–16, 2022. Disponível em: https://doi.org/10.1029/2022JA030513.

IAGA. **Model field at a point by IGRF 13**. [*S.l.*], 2024.

IGS. **RINEX**. [*S.l.*], 2024.

INSTITUTO BRASILEIRO DE GEOGRAFIA E ESTATÍSTICA. **RBMC - Rede Brasileira de Monitoramento Contínuo dos Sistemas GNSS**. [*S.l.*], 2024.

JOHNSON, N.; KOTZ, S.; BALAKRISHNAN, N. **Continuous Univariate Distributions**. 2nd. ed. [*S.l.*]: John Wiley & Sons, Inc, 1995.

JOSHI, K.; ADHIKARI, G.; BHATTARAI, D.; ADHIKARI, A.; LAMICHANNE, S. Forest fire vulnerability in Nepal's Chure region: Investigating the influencing factors using generalized linear model. **Heliyon**, v. 10, p. e28525, 2024. Disponível em: https://doi.org/10.1016/j.heliyon.2024.e28525.

KANG, S. M.; LU, J. Expansion of the hadley cell under global warming: Winter versus summer. **Journal of Climate**, American Meteorological Society, Boston MA, USA, v. 25, n. 24, p. 8387 – 8393, 2012. Disponível em: https://doi.org/10.1175/JCLI-D-12-00323.1.

KANJI, G. **100 Statistical Tests**. 3rd. ed. [*S.l.*]: Sage Publication, 2006.

KARAN, D. K.; DANIELL, R. E.; ENGLAND, S. L.; MARTINIS, C. R.; EASTES, R. W.; BURNS, A. G.; MCCLINTOCK, W. E. First zonal drift velocity measurement of equatorial plasma bubbles (epbs) from a geostationary orbit using gold data. **Journal of Geophysical Research: Space Physics**, Wiley Online Library, v. 125, n. 9, p. e2020JA028173, 2020.

KATO, S. **Dynamics of the upper atmosphere**. [*S.l.*]: Center of Academic Publications Japan, 1980.

KAUFMAN, L.; ROUSSEEUW, P. **Finding groups in data: An introduction to cluster analysis**. 1st. ed. [*S.l.*]: Wiley, 2005.

KELLEY, M. **The Earth's Ionosphere: Plasma Physics and Electrodynamics**. 2nd. ed. [*S.l.*]: Elsevier, 2008.

KHERANI, E.; ABDU, M.; PAULA, E.; FRITTS, D.; SOBRAL, J.; JR, F. M. The impact of gravity waves rising from convection in the lower atmosphere on the generation and nonlinear evolution of equatorial bublble. **Annales Geophisicae**, v. 27, p. 1657–1668, 2009. Disponível em: https://doi.org/10.5194/angeo-27-1657-2009.

KIL, H. The morphology of equatorial plasma bubbles – a review. **JASS**, v. 32, n. 1, p. 12–19, 2015. Disponível em: https://doi.org/10.5140/JASS.2015.32.1.13.

KIRCHHOFF, V. **Introdução a geofísica espacial**. 1st. ed. [*S.l.*]: Edusp, 1991.

KLIPP, T.; PETRY, A.; SOUZA, J.; FALCãO, G.; VELHO, H.; PAULA, E.; ANTREICH, F.; HOQUE, M.; KRIEGEL, M.; BERDERMANN, J.; JAKOWSKI, N.; FERNANDEZ-GOMEZ, I.; BORRIES, C.; SATO, H.; WILKEN, V. Evaluation of ionospheric models for Central and South Americas. **Advances in Space Research**, v. 64, p. 2125–2136, 2019. Disponível em: https://doi.org/10.1016/j.asr.2019.09.005.

LANDAU, L.; LIFSHITZ, E. (Ed.). **Fluid Mechanics**. 2nd. ed. [*S.l.*]: Pergamon Press, 1987. ISBN 0-08-033933-6.

LARANJA, S.; FEJER, B.; RIDENTI, M.; SWENSON, C. Ion density climatology based on FPMU measurements on board the International Space Station. **Jornal of Geophysical Research: Space Physics**, v. 128, n. e2023JA031980, 2023. Disponível em: https://doi.org/10.1029/2023JA031980.

LARNER, A. **The 2x2 Matrix: Contigency, Confusion, and the Metrics os Binary Classification**. [*S.l.*]: springer, 2021.

LI, Q.; ZHU, Y.; FANG, K.; FANG, J. Statistical study of the seasonal variations in tec depletion and the roti during 2013-2019 over hong kong. **Sensors**, v. 20, n. 6200, p. 1–17, 2020. Disponível em: https://doi.org/10.3390/s20216200.

LU, J.; VECCHI, G. Tropical meteorology & climate | Hadley circulation. *In*: NORTH, G. R.; PYLE, J.; ZHANG, F. (Ed.). **Encyclopedia of Atmospheric Sciences (Second Edition)**. Second edition. Oxford: Academic Press, 2015. p. 113–120. ISBN 978-0-12-382225-3. Disponível em: https://doi.org/10.1016/B978-0-12-382225-3.00161-4.

LUO, X.; DU, J.; MONICO, J. G.; XIONG, C.; LIU, J.; LIANG, X. ROTI-based stochastic model to improve GNSS precise point positioning under severe geomagnetic storm activity. **Space Weather**, v. 20, n. e2022SW003114, p. 1 – 14, 2022. Disponível em: https://doi.org/10.1029/2022SW003114.

MA, G.; MARUYAMA, T. A super bubble detected by dense GPS network at east Asian longitudes. **Geophysical Research Letters**, v. 33, p. L21103, 2006. Disponível em: https://doi.org/10.1029/2006GL027512.

MACHADO, W.; AGUIAR, C. Impacto da densificação da RBMC entre 2012 e 2014 sobre a capacidade de monitoramento do TEC. **Revista Brasileira de Cartografia**, v. 68, n. 1, 2016. Disponível em: https://doi.org/10.14393/rbcv68n1-44481.

MAKELA, J.; MILLER, E. Influences on the development of equatorial plasma bubbles: Insight from a long-term optical dataset. *In*: ABDU, M.; PANCHEVA, D. (Ed.). **Aeronomy of the Earth's Atmosphere and Ionosphere**. Springer, 2011. p. 239–249. Disponível em: https://doi.org/10.1007/978-94-007-0326-1_17.

MAKELA, J.; OTSUKA, Y. Overview of nighttime ionospheric instabilities at low- and mid-latitudes: Coupling aspects resulting in structuring at the mesoescale. **Space Science Review**, v. 168, p. 419–440, 2012. Disponível em: https://doi.org/10.1007/s11214-011-9816-6.

MARTINSON, D. **Quantitative Methods of Data Analysis for the Physical Science and Engineering**. 1st. ed. [*S.l.*]: Cambridge University Press, 2018.

MARUYAMA, N. Storms and substorms-the new whole system approach and future challenges. *In*: MATERASSI, M.; FORTE, B.; COSTER, A.; SKONE, S. (Ed.). **The dynamical ionosphere**. Elsevier, 2020. p. 87–119. Disponível em: https://doi.org/10.1016/B978-0-12-814782-5.00010-8.

MASTRANTONIO, G.; EINAUDI, F.; FUA, D.; LALAS, D. Generation of gravity waves by jet streams in the atmosphere. **Journal of Atmospheric Sciences**, v. 33, n. 9, 1976. Disponível em: https://doi.org/10.1175/1520-0469(1976)033<1730:GOGWBJ>2.0.CO;2.

MCCULLOCH, C.; SEARLE, S. **Generalized, Linear and Mixed Models**. 1st. ed. [*S.l.*]: John Wiley & Sons, Inc, 2001.

MCDONALD, K. The modernization of gps: Plans, new capabilities and the future relationship to galileo. **Journal of Global Positioning Systems**, v. 1, n. 1, 2002. Disponível em: https://doi.org/10.5081/jgps.1.1.1.

MEEUS, J. **Astronomical Algorithms**. 2nd. ed. [*S.l.*]: Willmann-Bell Inc., 1998.

MENDILLO, M.; LIN, B.; AARONS, J. The application of GPS observations to equatorial aeronomy. **Radio Science**, v. 35, p. 885–904, 2000. Disponível em: https://doi.org/10.1029/1999RS002208.

MOFFAT-GRIFFIN, T.; COLWEEL, S.; WRIGHT, C.; HINDLEY, N.; MITCHELL, N. Radiosonde observations of a wintertime meridional convergence of gravity waves around 60°s in the lower stratosphere. **Geophysical Research Letters**, v. 47, p. e2020GL089740, 2020. Disponível em: https://doi.org/10.1029/2020GL089740.

MOFFAT-GRIFFIN, T.; HIBBINS, R.; M., J.; COLWELL, S. Seasonal variations of gravity wave activity in the lower stratosphere over an antarctic peninsula station. **Jornal of Geophysical Research**, v. 116, p. D14111, 2011. Disponível em: https://doi.org/10.1029/2010JD015349.

MUKHERJEE, M.; SARKAR, S.; PUROHIT, P.; GWAL, A. Seasonal variation of total electron content at crest of equatorial anomaly station during low solar activity conditions. **Advances in Space Research**, v. 46, p. 291–295, 2010. Disponível em: https://doi.org/10.1016/j.asr.2010.03.024.

MYERS, R.; MONTGOMERY, D.; VINING, G.; ROBINSON, T. **Generalized Linear Models**. 2nd. ed. [*S.l.*]: John Wiley & Sons, Inc, 2010.

NAPPO, C. **An introduction to atmospheric gravity waves**. 2nd. ed. [*S.l.*]: Elsevier: Academic press, 2013.

NASA. **OMNIWeb PLUS**: Greenbelt, MD: Nasa Goddard Space Flight Center. [*S.l.*], 2024.

NGUYEN, C.; OLUWADARE, S.; LE, N.; ALIZADEH, M.; WICKERT, J.; SCHUCH, H. Spatial and temporal distributions of ionospheric irregularities derived from regional and global ROTI maps. **Remote Sensing**, v. 14, n. 10, p. 1 – 25, 2022. Disponível em: https://doi.org/10.3390/rs14010010.

NOAA. **Scales Explanation**. 2024. Accessed: 2024-07-30. Disponível em: https://www.swpc.noaa.gov/noaa-scales-explanation.

NYASSOR, P.; WRASSE, C.; PAULINO, I.; GOBBI, D.; YIĞIT, E.; TAKAHASHI, H.; BATISTA, P.; NACCARATO, K.; BURITI, R.; PAULINO, A. *et al.* Investigations on concentric gravity wave sources over the brazilian equatorial region. **Journal of Geophysical Research: Atmospheres**, Wiley Online Library, v. 127, n. 17, p. e2021JD035149, 2022.

OLIVEIRA, A.; CAZUZA, E.; MEDEIROS NETO, J.; SILVA JUNIOR, J.; BARBOSA, A.; BORBA, A.; MENDES, D.; SILVA, M.; ALCâNTARA, M. Ondas de gravidade na estratosfera equatorial brasileira: estudo de caso. **Holos**, v. 8, n. 32, p. 24–35, 2016. Disponível em: https://doi.org/10.15628/holos.2016.4638.

OLIVEIRA, A. L. P. d. **Estudo de ondas de gravidade na estratosfera a partir de sondagens com balões lançados no Centro de Lançamento da Barreira do Inferno**. 102 p. Tese (Doutorado em Ciências Climáticas) — Universidade Federal do Rio Grande do Norte, Natal, 2016.

OLIVEIRA FILHO, K.; SARAIVA, M. **Astronomia e Astrofísica**. 4a. ed. [*S.l.*]: Livraria da Física, 2011.

OLSEN, N.; STOLLE, C. Magnetic signatures of ionospheric and magnetospheric current systems during geomagnetic quiet conditions—an overview. **Space Science Reviews**, p. 1 – 21, 2017. Disponível em: https://doi.org/10.1007/s11214-016-0279-7.

PALMÉN, E.; NEWTON, C. W. *et al.* **Atmospheric circulation systems: their structure and physical interpretation**. [*S.l.*]: Academic press, 1969.

PANDOVE, D.; GOEL, S.; RANI, R. General correlation coefficient based agglomerative clustering. **Cluster Computing**, v. 22, p. 553–583, 2018. Disponível em: https://doi.org/10.1007/s10586-018-2863-y.

PAULINO, I.; TAKAHASHI, H.; MEDEIROS, A.; WRASSE, C.; BURITI, R.; SOBRAL, J.; GOBBI, D. Mesospheric gravity waves and ionospheric plasma bubbles observed during the copex campaign. **Journal of Atmospheric and Solar-Terrestrial Physics**, v. 73, n. 11, p. 1575–1580, 2011. ISSN 1364-6826. Disponível em: https://doi.org/10.1016/j.jastp.2010.12.004.

PEREGRINE, D. H. Interaction of water waves and currents. **Advances in applied mechanics**, Elsevier, v. 16, p. 9–117, 1976.

PEREIRA, V.; CAMARGO, P. Estimativas e análises de índice de irregularidades da ionosfera utilizando dados de gps de redes ativas. **Boletim de Ciências Geodésicas**, v. 19, n. 3, p. 374–390, 2013. Disponível em: https://doi.org/10.1590/S1982-21702013000300002.

PEñA, D.; TSAY, R. **Statistical Learning for Big Dependent Data**. 1st. ed. [*S.l.*]: Wiley, 2021.

PI, X.; MANNUCCI, J.; LINDQWISTER, U.; HO, C. Monitoring of global ionospheric irregularities using the worldwise gps network. **Geophysical Research Letters**, v. 24, n. 18, p. 2283–2286, 1997. Disponível em: https://doi.org/10.1029/97GL02273.

PIMENTA, A. Propagation of nighttime medium-scale traveling ionospheric disturbances (mstids) during high and low solar-activity conditions. **URSI Radio Science Letters**, v. 2, 2020. Disponível em: https://doi.org/10.46620/20-0015.

PIMENTA, A.; AMORIN, D.; CANDIDO, C. Thermospheric dark band structures at low latitudes in the southern hemisphere under different solar activity conditions: A study using oi 630 nm emission all-sky images. **Geophysical Research Letters**, v. 35, n. L16103, 2008. Disponível em: https://doi.org/10.1029/2008GL034904.

PRESS, W.; TEUKOLSKY, S.; VETTERLING, W.; FLANNERY, B. **Numerical Recipes: The art of Scientific Computing**. 3rd. ed. [*S.l.*]: Cambridge, 2007.

R Core Team. **R: A Language and Environment for Statistical Computing**. Vienna, Austria, 2020. Disponível em: https://www.R-project.org/.

REZENDE, L.; PAULA, E.; STEPHANY, S.; KANTOR, I.; MUELLA, M.; SIQUEIRA, P.; CORREA, K. Survey and prediction of the ionospheric scintillation using data mining techniques. **Space Weather**, v. 8, n. 6, p. 1–10, 2010. Disponível em: https://doi.org/10.1029/2009SW000532.

RICHARDS, J. **Radio Wave Propagation: An Introduction for the Non-Specialist**. 1st. ed. [*S.l.*]: Springer, 2008.

RISHBETH, H.; GARRIOT, O. **Introduction to Ionospheric Physics**. [*S.l.*]: Elsevier, 1969.

ROSSBY, C.; WILLET, H. The circulation of the upper troposphere and lower stratosphere. **Science**, v. 108, n. 2815, 1948. Disponível em: https://doi.org/10.1126/science.108.2815.643.

ROSTOKER, G. Geomagnetic indices. **Reviews of Geophysics and Space Physics**, v. 10, n. 4, p. 935–950, 1972.

ROURKE, S.; MULLIGAN, F.; FRENCH, W.; MURPHY, D. A climatological study of short-period gravity waves and ripples at Davis station, Antarctica (68°S, 78°E), during the (austral winter February–October) period 1999–2013. **Journal of Geophysical Research: Atmospheres**, Wiley Online Library, v. 122, n. 21, p. 11–388, 2017.

SAHAI, Y.; FAGUNDES, P.; BITTENCOURT, J. Transequatorial f-region ionospheric plasma bubbles: solar cycle effects. **Jornal of Atmospheric and Solar-Terrestrial Physics**, v. 62, p. 1377–1383, 2000. Disponível em: https://doi.org/10.1016/S1364-6826(00)00179-6.

SALBY, M. **Physics of the atmosphere and climate**. 1. ed. [*S.l.*]: Cambridge, 2012.

SCHUNK, R.; NAGY, A. **Ionophere: Physics, Plasma Physics, and Chemistry**. 2nd. ed. [*S.l.*]: Cambridge university press, 2009.

SECAN, J.; BUSSEY, R.; FREMOUW, E.; BASU, S. An improved model of equatorial scintillation. **Radio Science**, v. 30, n. 3, p. 607–617, 1995. Disponível em: https://doi.org/10.1029/94RS03172.

SEEBER, G. **Satellite Geodesy**. 2nd. ed. [*S.l.*]: WdeG, 2003.

SEEMALA, G. Estimation of ionospheric total electron content (TEC) from GNSS observations. *In*: **Atmospheric Remote Sensing: Principles and Applications**. [*S.l.*]: Elsevier, 2023. cap. 4, p. 63–84.

SEEMALA, G. **GPR-TEC analysis program Ver 2.95**. [Software], 2024. Accessed: 2024-07-30. Disponível em: https://seemala.blogspot.com/.

SEEMALA, G.; VALLADARES, C. Statistics of total electron content depletions observed over the South American continent for the year 2008. **Radio Science**, v. 46, n. RS5019, p. 1–14, 2011. Disponível em: https://doi.org/10.1029/2011RS004722.

SHARMAN, R.; TRIER, S. Influences of gravity waves on convectively induced turbulence (cit): A review. **Pure and Applied Geophysics**, v. 176, n. 11–13, p. 1923–1958, 2018. Disponível em: https://doi.org/10.1007/s00024-018-1849-2.

SIVAKANDAN, M.; PAULINO, I.; RAMKUMAR, T.; TAORI, A.; PATRA, A.; SRIPATHI, S.; NIRANJAN, K.; BILIBIO, A. Multi-instrument investigation of troposphere-ionosphere coupling and the role of gravity waves in the formation of equatorial plasma bubble. **J. of Atmospheric and Solar-Terrestrial Physics**, v. 189, p. 65–79, 2019. Disponível em: https://doi.org/10.1016/j.jastp.2019.04.006.

SOUZA, J.; JR, W. A.; SANTOS, P.; PETRY, A.; BAILEY, G.; BATISTA, I.; ABDU, M. Longitudinal variation of the equatorial ionosphere: Modeling and experimental results. **Advances in Space Research**, v. 51, p. 654–660, 2012. Disponível em: https://doi.org/10.1016/j.asr.2012.01.023.

STOLLE, C.; LÜHR, H.; ROTHER, M.; BALASIS, G. Magnetic signatures of equatorial spread f as observed by the champ satellite. **Journal of Geophysical Research: Space Physics**, Wiley Online Library, v. 111, n. A2, 2006.

STULL, R. **An introduction to Boundary Layer Meteorology**. 1st. ed. [*S.l.*]: Kluwer, 1988.

SU, S.-Y.; YEH, H.; HEELIS, R. Rocsat 1 ionospheric plasma and electrodynamics instrument observations of equatorial spread f: An early transitional scale result. **Journal of Geophysical Research: Space Physics**, Wiley Online Library, v. 106, n. A12, p. 29153–29159, 2001.

SUBIRANA, J.; ZORNOZA, J.; HERNáNDEZ-PAJARES, M. **GNSS Data processing: fundamentals and algorithms**. [*S.l.*]: Esa Communications, 2013.

TAKAHASHI, H.; WRASSE, C.; FIGUEIREDO, C.; BARROS, D.; PAULINO, I.; ESSIEN, P.; ABDU, M.; OTSUKA, Y.; SHIOKAWA, K. Equatorial plasma bubble occurrence under propagation of MSTID and MLT gravity waves. **Journal of Geophysical Research: Space Physics**, Wiley Online Library, v. 125, n. 9, p. e2019JA027566, 2020.

TAORI, A.; PATRA, A.; JOSHI, L. Gravity wave seeding of equatorial plasma bubbles: An investigation with simultaneous f region, e region, and middle atmospheric measurements. **Journal of Geophysical Research: Space Physics**, Wiley Online Library, v. 116, n. A5, 2011.

TAPPING, K. The 10.7 cm solar radio flux ($F_{10.7}$). **Space Weather**, v. 11, n. 4, p. 394–406, 2013. Disponível em: https://doi.org/10.1002/swe.20064.

TOMIKAWA, Y. Gravity wave transmission diagram. **Annales Geophysicae**, v. 33, n. 12, p. 1479–1484, 2015. Disponível em: https://doi.org/10.5194/angeo-33-1479-2015.

TSUDA, T.; KATO, T.; YOKOI, T.; INOUE, T.; YAMAMOTO, M.; VANZANT, T.; FUKAO, S.; SATO, T. Gravity waves in the mesophere observed with the middle and upper atmosphere radar. **Radio Science**, v. 26, n. 5, p. 1005–1018, 1990. Disponível em: https://doi.org/10.1029/RS025i005p01005.

TSUNODA, R. Observations of Equatorial Spread F: A working hypothesis. *In*: HUANG, C.; LU, G. (Ed.). **Space Physics and Aeronomy Collection Volume 3: Ionosphere Dynamics and Applications**. Jonh Wiley & Sons, 2021. p. 201–280. Disponível em: https://doi.org/10.1002/9781119815617.ch11.

VADAS, S.; FRITTS, D.; ALEXANDER, M. Mechanism for the generation of secondary waves in wave breaking regions. **Jornal of the Atmospheric Science**, v. 60, p. 194–214, 2003. Disponível em: https://doi.org/10.1175/1520-0469(2003)060<0194:MFTGOS>2.0.CO;2.

Van Doninck, J. **solarPos: Solar Position Algorithm for Solar Radiation Applications. [Wien: Institute for Statistics and Mathematics Wirtschaftsuniversität Wien]**. [*S.l.*], 2016. R package version 1.0. Disponível em: https://CRAN.R-project.org/package=solarPos.

VINCENT, R.; ALEXANDER, M. Gravity waves in the tropical lower stratosphere: An observational study of season and interannual variability. **Journal of Geophysical Research**, Wiley Online Library, v. 105, n. D14, p. 17971–17982, 2000. Disponível em: https://doi.org/2000JD900196.

VINCENT, R.; ECKERMANN, S.; ALLEN, S. Gravity-wave parameters in the low stratosphere. *In*: HAMILTON, K. (Ed.). **Gravity Wave Processes: Their Parameterization in Global Climate Models**. Springer, 1997. p. 7–25. Disponível em: https://doi.org/10.1007/978-3-642-60654-0_2.

VOLLAND, H. **Atmospheric Tidal and Planetary Waves**. [*S.l.*]: KLUER, 1988.

WOOD, A.; DONEGAN-LAWLEY, E.; CLAUSEN, L.; SPOGLI, L.; URBář, J.; JIN, Y.; SHAHTAHMASSEBI, G.; ALFONSI, L.; RAWLINGS, J.; CICONE, A.; KOTOVA, D.; CESARONI, C.; HøEG, P.; DORRIAN, G.; WOJTKIEWICZ, P.; MILOCH, W. Statistical models of the variability of plasma in the topside ionosphere: 1. development and optimisation. **Journal of Space Weather and Space Climate**, v. 14, n. 7, p. 1–19, 2024. Disponível em: https://doi.org/10.1051/swsc/2024002.

WORLD METEROLOGICAL ORGANIZATION. **Guide to instruments and methods of observation**. [*S.l.*]: WMO, 2018.

YASYUKEVICH, Y.; YASYUKEVICH, A.; RATOVSKY, K.; KLIMENKO, M.; KLIMENKO, V.; CHIRIK, N. Winter anomaly in NmF2 and TEC: when and where it can occur. **Journal Space Weather and Space Climate**, v. 8, n. A45, 2018. Disponível em: https://doi.org/10.1051/swsc/2018036.

YIGIT, E. **Atmospheric and Space Science: Neutral Atmospheres**. 1st. ed. [*S.l.*]: Springer, 2015.

YIGIT, E.; MEDVEDEV, A. Internal wave coupling process in earth's atmosphere. **Advances in Space Research**, v. 55, p. 983–1003, 2015. Disponível em: https://doi.org/10.1016/j.asr.2014.11.020.

YOO, J.-H.; CHOI, T.; CHUN, H.-Y.; KIM, Y.-H.; SONG, I.-S.; SONG, B.-G. Inertia-gravity waves revealed in radiosonde data at Jang Bogo Station, Antarctica (74° 37' S, 164° 13' E): 1. Characteristics, energy, and momentum flux. **Journal of Geophysical Research: Atmospheres**, Wiley Online Library, v. 123, n. 23, p. 13–305, 2018.

YOO, J.-H.; SONG, I.-S.; CHUN, H.-Y.; SONG, B.-G. Inertia-gravity waves revealed in radiosonde data at Jang Bogo Station, Antarctica (74° 37' S, 164° 13' E): 2. Potential sources and their relation to inertia-gravity waves. **Journal of Geophysical Research: Atmospheres**, Wiley Online Library, v. 125, n. 7, p. e2019JD032260, 2020.

YOSHIKI, M.; SATO, K. A statistical study of gravity waves in the polar regions based on operational radiosonde data. **Journal of Geophysical Research: Atmospheres**, Wiley Online Library, v. 105, n. D14, p. 17995–18011, 2000. Disponível em: https://doi.org/10.1029/2000JD900204.

ZHANG, S.; YI, F. A statistical study of gravity waves from radiosonde observation at Wuhan (30°N, 114°E) China. **Annales Geophisicae**, v. 23, p. 665–673, 2005. Disponível em: https://doi.org/10.5194/angeo-23-665-2005.

ZHANG, W.; D, Z.; XIAO, Z. The influence of geomagnetic storms on the estimation of GPS instrumental biases. **Annales Geophysicae**, v. 27, p. 1613–1623, 2009. Disponível em: https://doi.org/10.5194/angeo-27-1613-2009.

ZHANG, Y.; XIONG, J.; LIU, L.; WAN, W. A global morphology of gravity wave activity in the stratosphere revealed by the 8-year saber/timed data. **Journal of Geophysical Research: Atmospheres**, Wiley Online Library, v. 117, n. D21, 2012. Disponível em: https://doi.org/10.1029/2012JD017676.

ZINK, F.; VINCENT, R. Wavelet analysis of stratospheric gravity wave packets over Macquarine Island. **J. Geophysical Research**, v. 106, n. D10, p. 10275–10288, 2001. Disponível em: https://doi.org/10.1029/2000JD900846.

Appendix A - Statistics of Energy Density from the Brazilian Lower Atmosphere

A.1 Kinetic and Potential energy at troposphere in 2014

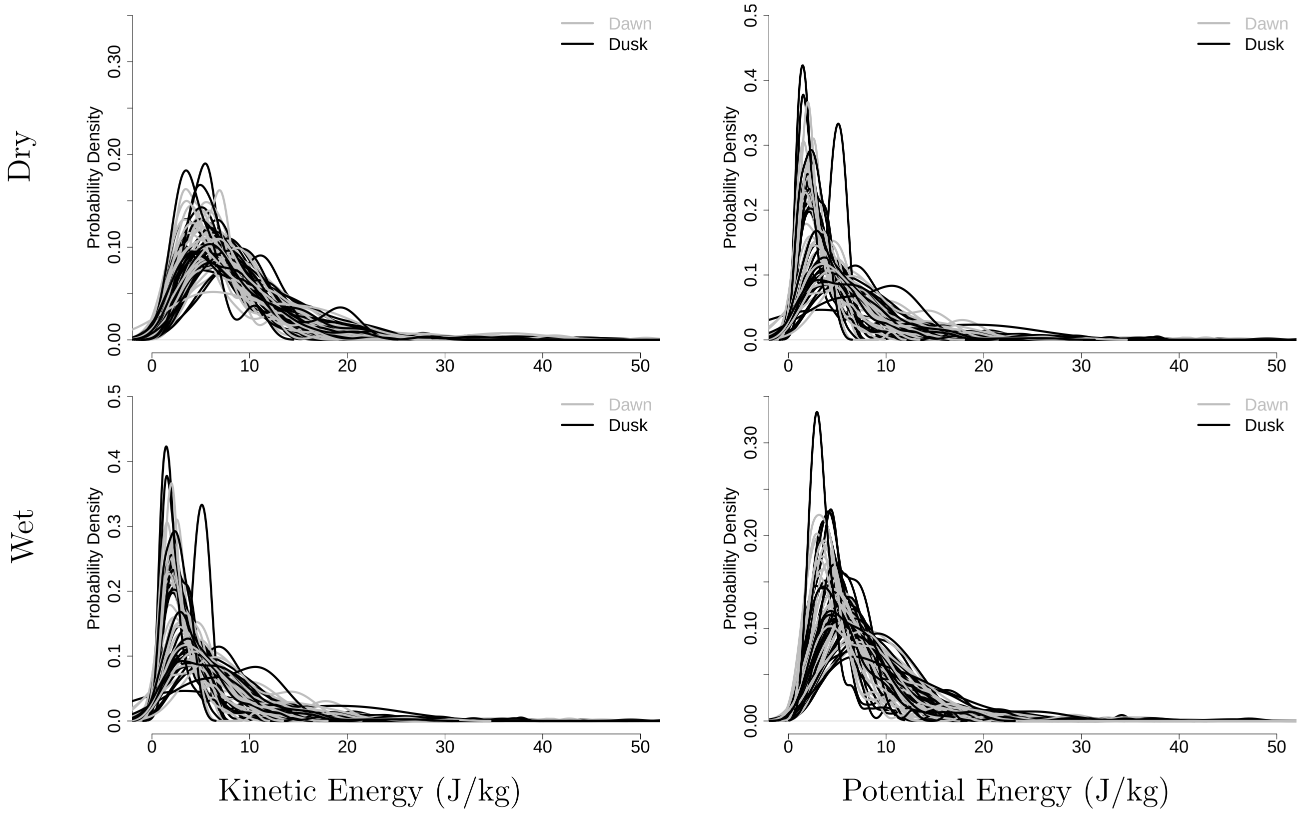

FIGURE A.1 – Kernel density estimator of the probability distribution function (PDF) for kinetic energy (left) and potential energy (right) during the dry season (top) and wet season (bottom) of 2014 in the troposphere. Each curve represents the probability distribution of kinetic and potential energy for an aerodrome, where the gray lines correspond to measurements taken near sunrise (12:00 UTC), and the black lines correspond to measurements taken near sunset (00:00 UTC).

TABLE A.1 – Statistics of kinetic energy from troposphere during the dry season in 2014.

Aerodromes	Min.	1st Qu.	Median	Mean	3rd Qu.	Max.	NA (Not Available in a Year)	St. Des.	CV(%)	Gamma (Shape)	Gamma (Scale)	Kolmogorov-Smirnov (p-value)
sbat	0.80	4.25	6.89	7.73	9.99	24.64	455	4.66	60.23	2.68	2.88	0.58
sbbr	1.77	4.63	6.95	8.19	9.28	39.56	475	5.55	67.79	3.16	2.59	0.02
sbbv	1.45	3.71	5.40	5.86	7.05	16.72	434	2.81	48.07	4.69	1.25	0.35
sbcf	2.31	5.06	6.90	7.72	9.25	37.95	516	4.14	53.63	4.76	1.62	0.12
sbcg	1.44	5.85	7.96	10.39	10.99	322.52	467	20.04	192.85	2.15	4.85	0.00
sbcr	0.25	7.19	9.89	10.85	12.45	91.64	537	7.74	71.31	3.22	3.37	0.09
sbct	1.58	5.40	7.83	8.84	11.28	28.90	416	4.78	54.09	3.77	2.34	0.44
sbcy	2.14	6.15	8.84	10.58	11.35	247.53	546	17.90	169.13	2.47	4.28	0.00
sbcz	1.39	3.48	5.47	6.36	7.94	35.80	533	4.25	66.94	2.90	2.19	0.82
sbfi	2.27	6.61	9.50	11.45	14.20	46.91	452	6.96	60.77	3.47	3.30	0.09
sbfl	2.12	6.02	8.96	10.23	13.12	37.72	419	5.84	57.10	3.50	2.92	0.26
sbfn	1.49	4.38	7.89	8.92	12.14	25.63	512	5.11	57.24	2.95	3.03	0.22
sbgl	1.73	5.35	7.21	8.00	10.15	24.74	497	3.76	47.01	4.91	1.63	0.65
sblo	2.36	5.45	7.60	8.64	10.71	27.81	584	4.57	52.87	4.43	1.95	0.41
sbmn	1.23	3.69	5.49	6.15	7.81	20.85	440	3.36	54.69	3.68	1.67	0.65
sbmq	0.85	4.31	6.55	7.60	9.28	87.54	413	6.16	80.97	2.92	2.60	0.20
sbmt	1.93	5.14	7.46	8.83	10.88	90.05	462	6.61	74.82	3.44	2.56	0.24
sbmy	1.15	3.07	5.59	6.21	8.38	17.79	517	3.54	57.02	3.04	2.04	0.14
sbnt	1.83	4.87	6.97	8.57	11.68	29.93	571	5.04	58.87	3.13	2.73	0.13
sbpa	1.81	5.27	8.10	10.67	13.55	44.59	420	7.79	73.00	2.52	4.23	0.00
sbpv	1.00	3.71	6.18	6.95	8.57	83.15	485	6.15	88.52	2.62	2.66	0.23
sbrb	2.21	4.63	6.43	6.72	8.32	15.99	676	3.01	44.80	5.42	1.24	0.97
sbsl	1.70	5.12	7.71	9.12	12.01	25.69	445	5.12	56.14	3.34	2.73	0.25
sbsm	1.70	4.34	7.76	8.59	10.84	41.22	629	5.69	66.22	2.96	2.90	0.64
sbsn	1.30	4.03	6.36	7.11	9.62	26.04	446	3.99	56.18	3.32	2.14	0.40
sbts	0.54	4.29	5.99	6.64	7.94	60.35	521	4.83	72.73	3.59	1.85	0.25
sbtt	0.39	3.72	5.58	8.05	7.77	193.12	644	19.87	246.94	1.35	5.95	0.01
sbua	1.28	3.16	4.04	5.31	6.31	15.27	692	3.36	63.28	3.00	1.77	0.43
sbug	2.83	5.95	8.00	10.86	14.29	36.23	710	7.47	68.75	2.72	3.99	0.76
sbul	0.47	3.92	6.16	8.70	9.44	320.65	442	19.38	222.80	1.53	5.70	0.00
sbvh	1.33	4.04	6.52	7.51	10.07	29.15	466	4.57	60.82	2.87	2.62	0.50
sbvt	0.19	4.78	7.06	8.14	10.40	60.66	417	5.61	68.97	2.72	2.99	0.33
Mean	1.46	4.74	7.04	8.30	10.22	68.95	507.47	6.87	80.45	3.23	2.83	0.32
Sd	0.66	1.01	1.29	1.63	2.06	82.83	85.37	4.96	51.00	0.89	1.17	0.27
CV(%)	45.24	21.32	18.34	19.61	20.11	120.13	16.82	72.23	63.39	27.72	41.19	83.57

TABLE A.2 – Statistics of kinetic energy from troposphere during the wet season in 2014.

Aerodromes	Min.	1st Qu.	Median	Mean	3rd Qu.	Max.	NA (Not Available in a Year)	St. Des.	CV(%)	Gamma (Shape)	Gamma (Scale)	Kolmogorov-Smirnov (p-value)
sbat	0.43	2.76	4.03	4.93	5.70	32.67	484	3.69	74.96	2.73	1.81	0.03
sbbr	1.07	3.30	4.71	5.81	7.13	32.51	494	3.96	68.17	2.99	1.94	0.04
sbbv	1.97	4.78	6.72	8.36	10.53	40.58	519	5.59	66.86	2.99	2.80	0.05
sbcf	0.93	3.88	5.63	7.26	7.87	130.86	500	9.35	128.73	2.29	3.17	0.00
sbcg	1.43	4.09	6.08	7.27	9.22	26.47	615	4.36	59.98	3.18	2.29	0.59
sbcr	1.15	3.93	5.82	7.09	8.54	27.72	535	4.58	64.57	3.03	2.34	0.23
sbct	0.45	4.66	7.03	7.94	9.76	30.72	457	4.71	59.28	3.21	2.47	0.25
sbcy	0.73	3.06	4.61	5.27	6.28	22.86	556	3.45	65.43	3.22	1.64	0.29
sbcz	1.41	3.14	4.28	4.87	5.84	15.97	550	2.60	53.47	4.21	1.16	0.66
sbfi	2.13	5.58	8.38	9.47	11.70	37.23	567	5.64	59.57	3.67	2.58	0.65
sbfl	1.98	5.82	7.77	9.09	11.04	31.01	459	4.96	54.53	3.99	2.28	0.18
sbfn	2.11	6.26	8.72	9.26	11.81	33.71	539	4.59	49.61	4.39	2.11	0.64
sbgl	2.72	4.99	6.86	7.71	9.62	22.69	540	3.76	48.69	4.74	1.63	0.29
sblo	2.20	4.18	5.51	6.30	7.32	18.01	637	3.18	50.57	4.73	1.33	0.76
sbmn	1.38	3.99	6.18	7.09	9.25	27.74	527	4.17	58.79	3.30	2.15	0.76
sbmq	1.30	5.72	8.32	9.61	11.91	66.05	470	6.19	64.43	3.37	2.85	0.60
sbmt	0.87	4.71	6.45	8.25	9.02	183.08	467	11.77	142.69	2.43	3.40	0.00
sbmy	1.48	3.31	5.58	7.71	7.90	121.59	546	13.20	171.29	1.53	5.05	0.00
sbnt	2.12	5.44	7.58	9.17	10.74	153.31	542	11.20	122.13	2.95	3.11	0.03
sbpa	1.73	5.81	7.98	9.24	11.63	38.41	442	5.14	55.63	3.94	2.34	0.46
sbpv	1.19	2.94	4.19	4.73	5.50	34.12	539	3.28	69.47	3.52	1.34	0.14
sbrb	1.35	3.55	4.79	5.48	7.23	14.87	667	2.82	51.47	4.08	1.34	0.86
sbsl	1.84	5.67	8.16	9.08	11.34	24.73	540	4.58	50.43	4.18	2.17	0.84
sbsm	1.73	4.87	6.42	7.86	10.61	34.54	613	4.90	62.37	3.24	2.42	0.13
sbsn	0.69	4.49	6.12	7.27	9.14	37.30	506	4.26	58.64	3.50	2.08	0.29
sbts	1.22	3.97	5.97	6.80	8.66	25.76	551	3.75	55.10	3.77	1.80	0.78
sbtt	1.17	3.94	5.51	6.46	8.16	21.33	641	3.87	59.98	3.27	1.98	0.78
sbua	1.47	4.21	5.39	6.56	8.30	17.04	707	3.69	56.25	3.76	1.74	0.80
sbug	1.64	5.98	8.76	10.32	13.00	45.52	556	6.64	64.39	2.98	3.46	0.56
sbul	0.86	3.07	4.59	5.76	6.97	34.51	446	4.29	74.54	2.64	2.18	0.04
sbvh	1.18	2.61	3.43	4.11	4.70	17.94	566	2.43	59.04	4.23	0.97	0.10
sbvt	1.45	4.04	6.55	7.87	9.09	215.91	463	13.26	168.63	2.22	3.54	0.01
Mean	1.42	4.34	6.19	7.31	8.92	50.52	538.78	5.43	73.43	3.38	2.30	0.37
Sd	0.54	1.05	1.47	1.64	2.14	51.22	65.60	2.98	33.69	0.74	0.84	0.31
CV(%)	37.98	24.23	23.78	22.38	23.97	101.38	12.18	54.82	45.89	21.94	36.41	84.47

TABLE A.3 – Statistics of potential energy from the troposphere during the dry season in 2014.

Aerodromes	Min.	1st Qu.	Median	Mean	3rd Qu.	Max.	NA (Not Available in a Year)	St. Des.	CV(%)	Gamma (Shape)	Gamma (Scale)	Kolmogorov-Smirnov (p-value)
sbat	0.46	2.84	5.17	6.49	8.81	36.63	415	4.99	76.83	1.97	3.29	0.54
sbbr	0.51	3.62	5.95	7.04	9.52	27.19	464	4.70	66.77	2.42	2.92	0.71
sbbv	0.29	1.74	2.90	3.59	4.74	23.25	484	2.65	74.00	2.44	1.47	0.48
sbcf	0.64	3.24	6.04	6.88	9.40	35.02	514	4.66	67.75	2.44	2.82	0.61
sbcg	0.40	3.52	5.74	7.28	9.38	43.82	486	5.75	78.94	2.11	3.45	0.41
sbcr	0.09	3.32	5.07	5.79	7.60	19.59	557	3.53	61.04	2.55	2.27	0.99
sbct	0.33	3.06	4.99	6.77	8.46	30.91	467	5.49	81.12	1.84	3.69	0.14
sbcy	1.05	4.35	7.06	8.43	10.45	35.92	557	6.16	73.04	2.30	3.67	0.47
sbcz	0.47	1.74	3.03	3.96	4.69	42.73	482	3.91	98.83	1.91	2.07	0.10
sbfi	0.74	3.98	5.83	7.48	9.22	53.61	468	6.02	80.38	2.25	3.33	0.25
sbfl	0.57	3.13	5.92	7.31	8.86	29.81	478	5.89	80.54	1.87	3.91	0.32
sbfn	0.31	2.05	2.90	3.27	4.09	11.08	542	1.72	52.61	3.83	0.85	0.54
sbgl	0.57	2.64	4.39	5.78	7.79	22.71	472	4.50	77.74	1.98	2.92	0.10
sblo	1.03	2.19	5.84	7.80	10.28	21.93	723	7.26	93.06	1.30	6.01	0.85
sbmn	0.28	1.68	2.65	3.48	4.52	20.52	506	2.66	76.41	2.21	1.58	0.19
sbmq	0.04	1.50	2.36	4.73	3.79	405.72	470	25.03	528.65	0.86	5.48	0.00
sbmt	0.49	2.99	4.76	6.29	7.53	30.28	466	5.15	81.81	2.00	3.15	0.03
sbmy	0.54	1.71	2.95	3.98	4.96	28.42	527	3.73	93.82	1.84	2.16	0.02
sbnt	0.90	1.72	3.31	3.34	4.75	5.74	710	1.65	49.28	3.57	0.94	0.41
sbpa	0.64	3.26	5.35	7.51	8.70	67.19	467	7.76	103.28	1.68	4.47	0.02
sbpv	0.43	1.81	3.06	3.95	5.04	18.34	489	3.09	78.41	2.06	1.91	0.24
sbrb	0.14	2.03	3.56	5.08	5.37	61.35	517	6.98	137.27	1.46	3.48	0.00
sbsl	0.39	1.79	2.75	3.35	4.40	14.42	484	2.18	64.91	2.53	1.33	0.82
sbsm	1.38	2.98	5.09	6.43	8.59	18.33	714	4.62	71.82	2.15	2.98	0.98
sbsn	0.46	1.68	2.84	4.11	4.66	82.29	498	6.77	164.89	1.47	2.79	0.00
sbts	0.12	1.53	2.09	2.76	3.17	11.31	563	2.04	73.67	2.37	1.17	0.02
sbtt	0.24	1.41	2.06	2.60	3.55	8.11	652	1.64	62.98	2.78	0.93	0.44
sbua	0.13	1.73	2.26	2.57	3.35	10.52	631	1.38	53.80	3.71	0.69	0.97
sbug	0.63	4.91	7.89	8.12	11.07	14.54	717	3.98	49.03	2.95	2.75	0.91
sbul	0.60	3.51	5.32	6.68	8.44	30.68	447	4.82	72.16	2.23	3.00	0.67
sbvh	0.56	2.41	3.82	4.70	6.37	17.50	463	3.21	68.18	2.29	2.05	0.76
sbvt	0.54	3.12	5.54	6.62	8.71	27.11	448	4.91	74.16	2.02	3.28	0.93
Mean	0.50	2.60	4.33	5.44	6.88	40.83	527.44	4.96	92.72	2.23	2.71	0.44
Sd	0.30	0.93	1.58	1.82	2.45	68.85	87.89	4.07	82.86	0.64	1.28	0.34
CV(%)	59.18	35.82	36.59	33.51	35.55	168.64	16.66	81.92	89.37	28.73	47.07	79.12

TABLE A.4 – Statistics of potential energy from the troposphere during the wet season in 2014.

Aerodromes	Min.	1st Qu.	Median	Mean	3rd Qu.	Max.	NA (Not Available in a Year)	St. Des.	CV(%)	Gamma (Shape)	Gamma (Scale)	Kolmogorov-Smirnov (p-value)
sbat	0.58	1.82	2.56	3.13	3.88	12.34	445	1.94	62.15	3.22	0.97	0.05
sbbr	0.50	1.98	2.89	3.93	4.67	18.66	470	3.04	77.46	2.20	1.78	0.01
sbbv	0.49	2.31	3.58	4.40	6.26	20.53	482	2.82	64.04	2.61	1.69	0.28
sbcf	0.49	2.25	3.30	4.16	5.58	17.50	486	2.89	69.43	2.49	1.67	0.12
sbcg	0.05	2.00	3.86	5.32	6.39	22.09	620	4.63	86.90	1.48	3.59	0.79
sbcr	0.62	1.57	2.52	2.92	3.85	10.36	520	1.79	61.16	3.01	0.97	0.44
sbct	0.09	2.27	3.68	5.27	6.11	47.05	489	6.33	120.27	1.52	3.46	0.00
sbcy	0.27	1.95	3.07	3.88	4.68	21.40	554	3.14	80.77	2.12	1.83	0.51
sbcz	0.13	1.51	2.06	2.54	2.95	31.30	508	2.43	96.02	2.44	1.04	0.05
sbfi	0.74	2.53	3.86	5.42	6.49	24.64	585	4.46	82.16	2.10	2.59	0.09
sbfl	0.59	2.91	4.70	6.34	7.37	48.77	493	6.46	101.94	1.85	3.43	0.02
sbfn	0.96	2.16	2.87	3.21	3.89	11.07	551	1.51	47.05	5.30	0.61	0.56
sbgl	0.56	2.17	3.57	4.73	5.30	53.43	485	5.05	106.91	1.91	2.48	0.01
sblo	0.68	2.71	3.83	4.51	5.03	11.84	720	3.02	67.04	2.47	1.83	0.95
sbmn	0.40	1.49	2.58	3.07	3.88	18.63	491	2.27	73.96	2.40	1.28	0.71
sbmq	0.27	1.24	2.03	2.34	2.85	13.32	486	1.59	67.81	2.77	0.84	0.63
sbmt	0.28	2.19	3.30	4.47	5.52	56.83	482	4.80	107.32	1.96	2.28	0.00
sbmy	0.10	1.57	2.31	2.86	3.45	21.06	494	2.16	75.37	2.61	1.10	0.16
sbnt	0.86	2.55	3.08	3.50	4.40	6.63	709	1.56	44.43	5.24	0.67	0.65
sbpa	0.68	2.79	4.08	5.50	6.59	26.99	469	4.34	78.89	2.14	2.57	0.06
sbpv	0.43	1.36	2.07	2.46	3.36	14.69	522	1.64	66.57	2.79	0.88	0.36
sbrb	0.28	1.54	2.25	2.76	3.27	14.40	518	2.18	79.04	2.32	1.19	0.00
sbsl	0.46	1.46	2.12	2.49	3.10	10.10	535	1.50	60.04	3.37	0.74	0.43
sbsm	0.88	2.87	4.59	5.38	6.98	19.45	633	3.53	65.58	2.64	2.04	0.89
sbsn	0.06	1.62	2.41	2.98	3.58	15.03	507	2.02	67.73	2.59	1.15	0.13
sbts	0.48	1.89	2.63	3.27	4.26	10.98	558	1.99	60.77	2.96	1.10	0.23
sbtt	0.12	1.29	2.00	2.44	3.36	7.73	638	1.54	63.36	2.61	0.93	0.87
sbua	0.26	1.65	2.44	2.98	3.42	14.04	580	2.16	72.58	2.64	1.13	0.15
sbug	0.51	2.77	4.88	5.51	6.70	27.52	592	4.15	75.22	2.18	2.53	0.65
sbul	0.12	2.15	3.27	4.30	5.33	20.74	451	3.26	75.82	2.16	1.99	0.03
sbvh	0.13	1.16	1.75	2.73	2.57	78.81	574	6.27	229.98	1.45	1.88	0.00
sbvt	0.68	2.46	4.43	5.39	6.88	22.94	454	3.89	72.19	2.20	2.45	0.27
Mean	0.43	2.01	3.08	3.88	4.75	23.47	534.41	3.14	80.00	2.55	1.71	0.32
Sd	0.26	0.52	0.88	1.17	1.44	16.42	70.77	1.50	32.07	0.85	0.85	0.31
CV(%)	60.39	25.86	28.59	30.27	30.25	69.99	13.24	47.84	40.09	33.18	49.46	98.74

A.2 Kinetic and Potential energy at lower stratosphere in 2014

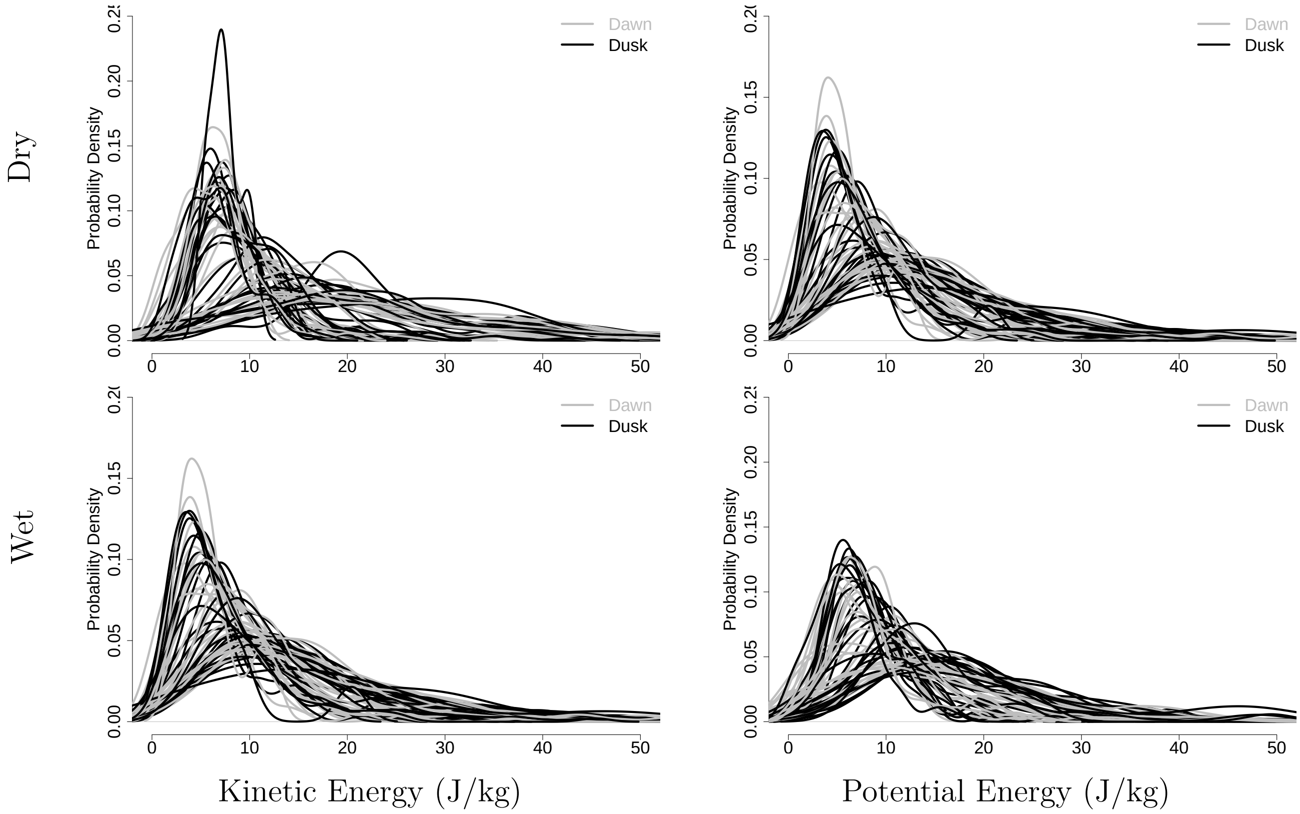

FIGURE A.2 – Kernel density estimator of the probability distribution function (PDF) for kinetic energy (left) and potential energy (right) during the dry season (top) and wet season (bottom) of 2014 in the lower stratosphere. Each curve represents the probability distribution of kinetic and potential energy for an aerodrome, where the gray lines correspond to measurements taken near sunrise (12:00 UTC), and the black lines correspond to measurements taken near sunset (00:00 UTC).

TABLE A.5 – Statistics of kinetic energy from the lower stratosphere during the dry season in 2014.

Aerodromes	Min.	1st Qu.	Median	Mean	3rd Qu.	Max.	NA (Not Available in a Year)	St. Des.	CV(%)	Gamma (Shape)	Gamma (Scale)	Kolmogorov-Smirnov (p-value)
sbat	0.94	8.03	11.59	12.94	16.89	37.38	482	6.86	52.97	3.59	3.60	0.94
sbbr	1.37	5.24	7.63	8.14	10.37	26.61	631	4.02	49.36	4.33	1.88	0.95
sbbv	0.00	10.67	16.25	20.35	26.48	99.00	482	13.78	67.69	2.03	10.02	0.08
sbcf	0.04	5.96	8.32	9.10	11.18	34.64	566	4.63	50.81	3.64	2.50	0.34
sbcg	0.10	6.13	8.75	9.41	11.80	29.03	635	4.58	48.65	3.81	2.47	0.85
sbcr	1.08	6.61	9.15	10.26	12.67	30.99	601	5.54	54.05	3.71	2.77	0.77
sbct	0.01	4.28	6.09	6.65	8.17	25.91	556	4.07	61.21	2.04	3.26	0.00
sbcy	0.05	6.08	8.64	9.56	12.21	29.50	564	4.95	51.82	3.40	2.82	0.35
sbcz	0.06	11.55	15.87	17.85	22.70	52.63	501	9.45	52.92	3.27	5.45	0.26
sbfi	0.16	5.65	7.61	8.28	10.23	21.91	467	3.83	46.27	4.25	1.95	0.62
sbfn	0.27	12.29	20.55	22.24	30.23	68.17	595	12.79	57.54	2.47	9.02	0.91
sbgl	0.48	5.49	7.36	8.02	9.95	22.60	498	3.60	44.81	4.84	1.66	0.65
sbmn	0.04	14.97	22.12	24.20	30.37	91.03	483	13.55	55.97	2.59	9.35	0.13
sbmq	0.00	12.93	20.72	23.24	32.13	71.28	502	13.35	57.46	1.78	13.06	0.02
sbmt	0.61	4.59	6.83	7.44	9.35	20.37	598	3.92	52.71	3.16	2.36	0.52
sbmy	0.05	13.85	19.30	20.21	25.32	53.39	541	10.84	53.63	2.18	9.27	0.00
sbnt	4.09	14.64	19.71	23.09	27.28	107.52	629	15.30	66.24	3.08	7.50	0.44
sbpa	0.00	4.95	7.42	7.55	9.45	25.69	467	3.68	48.66	2.87	2.63	0.00
sbpv	0.56	11.02	15.37	16.90	20.26	58.05	446	8.40	49.72	4.07	4.15	0.20
sbrb	0.00	9.38	12.84	14.05	17.10	42.68	476	7.41	52.75	2.35	5.99	0.00
sbsl	1.67	11.75	15.80	18.31	24.23	45.29	639	9.56	52.22	3.46	5.30	0.94
sbsm	4.02	6.35	7.80	8.69	10.65	28.51	647	3.56	40.95	7.37	1.18	0.52
sbsn	1.53	16.34	24.21	25.67	33.92	84.04	480	12.98	50.58	3.54	7.26	0.67
sbts	0.00	11.51	17.67	19.73	25.48	64.18	534	11.16	56.59	2.24	8.79	0.17
sbtt	0.29	14.92	21.26	22.82	31.89	55.02	633	10.75	47.09	3.40	6.72	0.58
sbua	0.34	10.83	18.24	19.69	25.28	62.87	646	12.40	63.00	1.85	10.62	0.44
sbug	2.66	5.47	6.94	6.91	7.92	10.78	715	2.01	29.10	11.07	0.62	0.93
sbul	0.22	4.20	6.06	6.60	8.36	26.96	576	3.80	57.62	2.84	2.32	0.52
sbvh	0.01	7.25	10.05	10.82	13.56	26.57	579	4.85	44.81	3.95	2.74	0.48
sbvt	0.01	4.32	6.58	7.01	8.50	20.48	511	3.58	51.10	3.29	2.13	0.58
Mean	0.69	8.91	12.89	14.19	18.13	45.77	556.00	7.64	52.28	3.55	4.98	0.46
Sd	1.12	3.86	5.88	6.57	8.85	25.63	71.08	4.09	7.51	1.80	3.37	0.32
CV(%)	161.78	43.35	45.64	46.31	48.80	56.01	12.78	53.58	14.37	50.64	67.77	69.83

TABLE A.6 – Statistics of kinetic energy from the lower stratosphere during the wet season in 2014.

Aerodromes	Min.	1st Qu.	Median	Mean	3rd Qu.	Max.	NA (Not Available in a Year)	St. Des.	CV(%)	Gamma (Shape)	Gamma (Scale)	Kolmogorov-Smirnov (p-value)
sbat	0.24	8.08	10.98	12.29	15.68	39.18	519	6.60	53.68	3.17	3.88	0.27
sbbr	0.11	4.92	7.21	8.22	11.15	22.83	612	4.55	55.35	2.68	3.07	0.30
sbbv	0.00	8.52	13.68	15.11	20.21	64.03	484	8.97	59.40	2.32	6.53	0.23
sbcf	0.15	5.18	7.18	7.90	9.92	37.89	513	4.39	55.63	3.26	2.42	0.20
sbcg	1.22	6.15	8.27	10.09	13.88	39.14	694	6.77	67.13	2.46	4.09	0.94
sbcr	0.10	6.66	9.55	11.20	13.47	52.54	553	7.30	65.12	2.89	3.88	0.37
sbct	0.08	4.55	6.75	7.33	9.26	27.35	572	4.16	56.68	2.73	2.69	0.31
sbcy	0.03	6.09	9.09	10.38	13.02	59.09	565	7.71	74.28	1.69	6.15	0.03
sbcz	0.04	9.37	12.46	14.37	18.66	42.22	529	7.36	51.26	2.75	5.22	0.02
sbfi	0.00	6.20	8.48	9.52	11.55	31.06	564	5.17	54.34	2.84	3.35	0.05
sbfn	3.80	12.71	17.12	19.08	23.93	55.62	587	9.54	49.98	4.46	4.28	0.59
sbgl	0.85	4.92	6.76	7.40	9.16	21.03	492	3.47	46.90	4.81	1.54	0.51
sbmn	0.00	11.64	16.23	17.78	23.15	57.41	542	9.64	54.23	1.80	9.88	0.00
sbmq	0.02	10.96	16.42	17.11	21.57	57.33	485	9.38	54.81	2.12	8.08	0.00
sbmt	0.87	4.75	6.53	7.50	9.49	21.66	584	3.80	50.65	3.78	1.98	0.97
sbmy	0.04	10.91	15.83	17.69	24.43	58.15	566	10.19	57.63	1.98	8.94	0.02
sbnt	1.00	9.50	14.93	16.88	21.64	52.08	637	10.05	59.53	2.85	5.91	0.97
sbpa	0.00	5.94	8.09	8.66	10.90	32.86	489	4.24	48.97	2.68	3.23	0.00
sbpv	0.06	9.12	13.06	14.63	19.24	43.79	510	8.11	55.47	2.20	6.64	0.01
sbrb	0.00	8.32	11.54	12.21	15.57	35.36	491	6.43	52.65	1.67	7.33	0.00
sbsl	0.38	8.52	14.46	15.64	20.58	67.46	693	10.93	69.85	2.14	7.32	0.63
sbsm	0.02	5.60	8.05	8.29	10.11	23.34	644	4.04	48.71	2.63	3.15	0.00
sbsn	0.00	11.55	16.96	18.41	23.82	59.20	485	9.86	53.53	2.43	7.56	0.05
sbts	0.51	6.12	10.77	12.30	16.33	43.81	601	7.75	63.01	2.34	5.26	0.97
sbtt	3.24	12.37	16.19	19.08	23.33	49.45	627	10.52	55.16	3.60	5.29	0.29
sbua	0.02	8.91	13.32	15.49	20.14	74.92	609	11.49	74.19	1.28	12.09	0.00
sbug	0.00	6.23	9.38	10.35	12.95	30.02	588	5.68	54.94	2.42	4.28	0.14
sbul	0.41	5.19	6.99	8.01	9.62	27.15	583	4.58	57.11	3.14	2.55	0.29
sbvh	0.04	7.33	11.11	12.09	14.63	49.37	628	6.95	57.46	2.88	4.19	0.35
sbvt	0.08	4.00	5.99	6.69	8.55	26.12	535	4.09	61.20	2.20	3.04	0.04
Mean	0.44	7.68	11.11	12.39	15.86	43.38	566.03	7.12	57.29	2.67	5.13	0.29
Sd	0.90	2.56	3.68	4.07	5.38	15.17	60.48	2.50	7.01	0.77	2.52	0.33
CV(%)	203.78	33.39	33.08	32.81	33.90	34.98	10.68	35.03	12.24	28.99	49.16	114.13

TABLE A.7 – Statistics of potential energy from the lower stratosphere during the dry season in 2014.

Aerodromes	Min.	1st Qu.	Median	Mean	3rd Qu.	Max.	NA (Not Available in a Year)	St. Des.	CV(%)	Gamma (Shape)	Gamma (Scale)	Kolmogorov-Smirnov (p-value)
sbat	1.41	8.10	11.94	14.66	17.59	70.08	481	9.95	67.85	2.69	5.45	0.19
sbbr	0.99	5.45	9.20	11.28	13.70	57.47	607	9.14	81.05	1.99	5.68	0.39
sbbv	0.04	9.64	14.69	17.07	21.62	67.18	437	11.15	65.33	2.17	7.87	0.30
sbcf	0.04	4.48	7.08	8.78	11.61	38.35	506	6.38	72.67	2.10	4.18	0.42
sbcg	2.45	5.31	7.49	9.59	12.13	37.32	611	6.50	67.76	2.89	3.32	0.19
sbcr	0.34	6.04	9.45	11.08	14.80	40.61	545	6.92	62.51	2.64	4.19	0.95
sbct	0.03	3.50	5.96	7.09	9.22	37.02	523	5.50	77.57	1.61	4.42	0.43
sbcy	0.16	6.65	9.34	11.25	14.06	48.38	497	6.93	61.56	2.79	4.04	0.60
sbcz	0.25	9.83	14.31	17.49	20.51	98.72	459	12.71	72.67	2.42	7.23	0.12
sbfi	0.26	3.90	6.37	7.77	9.81	37.44	421	5.64	72.56	2.29	3.40	0.22
sbfn	0.14	7.58	12.94	14.67	18.91	55.20	575	9.27	63.16	2.31	6.35	0.96
sbgl	0.17	4.19	6.10	7.77	10.21	33.80	422	5.33	68.62	2.43	3.19	0.08
sbmn	0.03	8.60	13.23	15.93	19.92	79.17	455	11.07	69.47	2.19	7.28	0.45
sbmq	0.00	7.28	11.36	15.12	19.09	80.39	468	12.70	83.99	1.39	10.87	0.01
sbmt	0.05	3.35	5.99	7.22	9.43	34.59	559	5.46	75.58	1.88	3.83	0.80
sbmy	0.13	8.94	14.55	16.88	21.86	103.69	506	12.42	73.58	1.90	8.88	0.51
sbnt	1.97	9.42	15.40	19.56	24.70	165.07	595	19.89	101.64	1.95	10.04	0.56
sbpa	0.01	3.02	4.65	5.77	7.58	24.80	423	4.04	70.10	1.83	3.16	0.10
sbpv	1.36	8.78	13.73	16.05	20.64	56.64	380	10.00	62.27	2.84	5.66	0.52
sbrb	0.02	7.94	12.95	15.41	19.77	61.11	422	10.37	67.28	1.92	8.02	0.39
sbsl	1.36	7.09	10.82	13.81	16.95	61.14	627	10.25	74.17	2.40	5.76	0.18
sbsm	1.43	3.74	5.65	6.80	8.57	26.19	607	4.20	61.81	3.17	2.15	0.70
sbsn	0.55	8.14	13.16	16.46	19.45	81.31	425	13.03	79.16	2.22	7.42	0.09
sbts	0.00	8.75	13.73	16.30	19.92	83.77	512	11.72	71.92	1.76	9.27	0.09
sbtt	1.20	9.71	14.20	16.56	19.23	78.99	622	11.48	69.31	2.66	6.22	0.37
sbua	0.15	7.62	13.14	17.10	22.45	98.88	645	14.36	83.97	1.64	10.45	0.64
sbug	1.99	3.18	5.31	5.95	6.43	20.43	711	4.09	68.76	3.08	1.93	0.46
sbul	0.85	4.57	7.72	9.07	11.69	29.89	551	6.18	68.16	2.21	4.10	0.97
sbvh	0.10	6.78	9.77	12.31	13.41	89.30	498	10.60	86.05	2.15	5.72	0.00
sbvt	0.01	4.17	6.47	8.07	10.43	59.25	473	6.54	81.03	2.04	3.95	0.43
Mean	0.58	6.53	10.22	12.43	15.52	61.87	518.77	9.13	72.72	2.25	5.80	0.40
Sd	0.72	2.27	3.49	4.21	5.21	30.96	82.81	3.66	8.80	0.45	2.48	0.28
CV(%)	124.32	34.72	34.10	33.90	33.55	50.03	15.96	40.16	12.10	19.77	42.71	69.71

TABLE A.8 – Statistics of potential energy from the lower stratosphere during the wet season in 2014.

Aerodromes	Min.	1st Qu.	Median	Mean	3rd Qu.	Max.	NA (Not Available in a Year)	St. Des.	CV(%)	Gamma (Shape)	Gamma (Scale)	Kolmogorov-Smirnov (p-value)
sbat	0.20	8.00	12.48	14.92	20.27	47.69	505	9.72	65.18	2.29	6.52	0.96
sbbr	0.09	5.10	7.85	11.72	13.59	122.95	593	13.52	115.38	1.45	8.07	0.20
sbbv	0.00	8.12	12.22	14.11	18.61	47.06	465	8.21	58.18	2.36	5.99	0.02
sbcf	0.13	4.63	7.37	9.82	12.54	65.47	482	8.75	89.07	1.72	5.71	0.18
sbcg	0.57	4.70	8.00	9.70	11.28	35.85	684	7.52	77.55	1.93	5.02	0.26
sbcr	0.31	6.79	10.86	13.03	17.77	61.24	534	9.32	71.56	2.12	6.15	0.86
sbct	0.05	3.09	5.92	7.14	8.87	35.28	541	6.15	86.13	1.44	4.96	0.57
sbcy	0.06	5.23	10.30	12.13	15.68	56.60	542	9.22	76.01	1.43	8.48	0.23
sbcz	0.25	8.05	13.62	15.33	20.10	45.85	482	9.53	62.19	2.27	6.74	0.26
sbfi	0.38	5.08	8.37	11.08	14.25	65.24	584	9.58	86.50	1.83	6.06	0.72
sbfn	0.46	8.03	12.48	14.04	18.08	47.42	564	8.26	58.85	2.87	4.89	0.99
sbgl	0.25	3.98	6.41	8.27	10.39	59.32	447	7.08	85.56	2.07	4.00	0.16
sbmn	0.00	8.71	12.68	14.83	18.65	55.28	510	9.36	63.13	2.14	6.93	0.09
sbmq	0.07	6.97	10.78	13.38	16.25	67.16	452	10.10	75.50	1.87	7.17	0.15
sbmt	0.40	3.96	6.27	9.00	10.25	52.17	567	8.13	90.23	1.70	5.31	0.06
sbmy	0.01	8.72	13.16	15.37	20.02	47.24	533	9.90	64.40	1.65	9.32	0.02
sbnt	0.14	7.63	11.67	14.88	19.51	81.45	579	11.36	76.34	2.21	6.73	0.52
sbpa	0.00	3.38	5.50	6.71	8.42	32.70	438	5.00	74.51	1.71	3.92	0.19
sbpv	0.12	8.23	13.36	15.16	20.31	55.49	456	9.49	62.60	2.06	7.35	0.47
sbrb	0.00	7.47	11.89	13.91	18.08	53.39	440	9.51	68.39	1.56	8.90	0.02
sbsl	0.06	4.91	9.31	9.34	12.42	20.71	684	5.75	61.52	1.64	5.69	0.20
sbsm	0.02	3.47	5.85	7.79	11.18	36.38	619	6.34	81.38	1.40	5.55	0.79
sbsn	0.02	9.23	13.35	15.50	19.22	53.40	442	9.37	60.43	2.65	5.85	0.19
sbts	1.53	7.83	12.97	15.70	20.08	71.48	616	11.82	75.31	2.14	7.35	0.81
sbtt	2.53	9.38	13.37	15.64	19.87	57.38	609	8.86	56.64	3.58	4.37	0.72
sbua	0.05	7.85	10.95	13.99	17.05	49.57	596	9.97	71.28	1.69	8.27	0.15
sbug	0.00	4.17	6.28	8.04	9.87	42.82	548	6.69	83.19	1.70	4.72	0.35
sbul	0.77	4.84	8.50	9.72	13.12	34.12	574	6.26	64.47	2.50	3.89	0.61
sbvh	0.16	7.15	12.46	16.10	20.38	56.09	616	11.91	74.00	1.95	8.24	0.37
sbvt	0.01	3.68	6.09	8.41	10.71	52.42	506	7.73	91.93	1.45	5.79	0.14
Mean	0.29	6.28	10.01	12.16	15.56	53.64	540.27	8.81	74.25	1.98	6.27	0.38
Sd	0.53	2.01	2.85	3.08	4.11	18.28	70.74	1.95	13.05	0.49	1.51	0.30
CV(%)	182.55	32.08	28.49	25.36	26.42	34.08	13.09	22.16	17.58	24.50	24.17	80.45

MINISTÉRIO DA DEFESA
COMANDO DA AERONÁUTICA
INSTITUTO TECNOLÓGICO DE AERONÁUTICA
PRÓ-REITORIA DE PÓS-GRADUAÇÃO

ATA DE EXAME DE TESE IP-PG/Nº189-T/2024

A Banca Examinadora reunida no dia **17 de dezembro de 2024 às 14h,** registra que o aluno **ALYSSON BRHIAN DE SOUZA MUNIZ SILVA,** matriculado no Curso de Doutorado do Programa de Pós-Graduação em **Física** Área **Dinâmica não-linear e Sistemas Complexos,** fez a apresentação de sua Tese sobre o tema**: “STATISTICAL STUDY OF GRAVITY WAVES IN THE LOWER ATMOSPHERE AND PREDICTIVE MODELING OF LOW LATITUDE IONOSPHERIC IRREGULARITIES”** como parte dos requisitos para obtenção do título ***“Doutor em Ciências”***.

A apresentação teve início às _____horas e término às ______horas. A banca, composta pelos membros relacionados abaixo, submeteu o candidato à arguição, que teve início às ______horas e término às ______horas.

Presidente:	Prof.	Érico Luiz Rempel
Orientador:	Prof.	Marco Antonio Ridenti
Coorientadores:	Profa.	Marisa Roberto (in memorian)
	Dr.	Francisco Javier Azpilicueta (UNLP)
Membro Interno:	Prof.	Rodrigo Sávio Pessoa
Membros Externos:	Dr.	Cristiano Max Wrasse (INPE)
	Dr.	Igo Paulino da Silva (UFCG)

O candidato foi submetido à apresentação oral e arguição por todos os membros da Banca Examinadora que consideraram a Tese:

☒ ***Aprovada*** ☐ ***Aprovada condicionalmente*** ☐ ***Reprovada***

Após discussão, a Banca Examinadora recomenda a mudança de título da Tese para o seguinte:

OBSERVAÇÃO: No caso de ***Aprovação Condicional***, preencher a continuidade da ata (Anexo I).

A data limite para entrega da versão final da Tese é: 31/01/2025 (esta data não pode ultrapassar o prazo para conclusão do curso, especificado no requerimento para nomeação da banca).

A Ata foi lavrada por mim, ***Prof.*** Érico Luiz Rempel**,** Presidente da Banca Examinadora, que, lida e aprovada, segue assinada por todos os membros.

Campo Montenegro, 17 de dezembro de 2024.

Prof. Érico Luiz Rempel	Prof. Rodrigo Sávio Pessoa
	Dr. Cristiano Max Wrasse (INPE)
Prof. Marco Antonio Ridenti	
Prof. Marisa Roberto (in memorian)	Dr. Igo Paulino da Silva (UFCG)
	Ciente: ALYSSON BRHIAN DE SOUZA MUNIZ SILVA

D4Sign
by ZUCCHETTI

3 páginas - Datas e horários baseados em Brasília, Brasil
Sincronizado com o NTP.br e Observatório Nacional (ON)
Certificado de assinaturas gerado em 23 de December de 2024, 09:20:53

ntp.br

Ata de Defesa ALYSSON BRHIAN DE SOUZA MUNIZ SILVA Preenchido pdf

Código do documento 4b79f4df-725c-481d-a7e2-a55048640bf8

Assinaturas

✓ Erico Luiz Rempel
Erico_rempel@yahoo.com.br
Assinou

Erico Luiz Rempel

✓ MARCO ANTONIO RIDENTI
aridenti@ita.br
Assinou

MARCO ANTONIO RIDENTI

✓ Francisco Javier Azpilicueta
azpi@fcaglp.unlp.edu.ar
Assinou

✓ Rodrigo Sávio Pessoa
rspessoa@ita.br
Assinou

Rodrigo Sávio Pessoa

✓ Cristiano Max Wrasse
cristiano.wrasse@inpe.br
Assinou

✓ Igo Paulino da Silva
igo.paulino@df.ufcg.edu.br
Assinou

Paulino

✓ Alysson Brhian de Souza Muniz Silva
alysson_brhian@outlook.com
Assinou

Alysson

Eventos do documento

19 Dec 2024, 10:23:07
Documento 4b79f4df-725c-481d-a7e2-a55048640bf8 **criado** por MARIA ELENICE ROCHA SANTANA (9b7590e6-aeb8-4517-86e9-7afc6f902c4c). Email:elenice@ita.br. - DATE_ATOM: 2024-12-19T10:23:07-03:00

19 Dec 2024, 10:26:54
Assinaturas **iniciadas** por MARIA ELENICE ROCHA SANTANA (9b7590e6-aeb8-4517-86e9-7afc6f902c4c). Email: elenice@ita.br. - DATE_ATOM: 2024-12-19T10:26:54-03:00

19 Dec 2024, 10:29:57
IGO PAULINO DA SILVA **Assinou** - Email: igo.paulino@df.ufcg.edu.br - IP: 187.19.131.146 (187-19-131-146-temp-internal.static.brisanet.net.br porta: 34276) - Geolocalização: -7.1941447556197335 -35.86764040840661 -

Documento de identificação informado: 040.429.104-08 - DATE_ATOM: 2024-12-19T10:29:57-03:00

19 Dec 2024, 10:30:29
MARCO ANTONIO RIDENTI **Assinou** - Email: aridenti@ita.br - IP: 161.24.23.100 (intra.ita.br porta: 27188) - Documento de identificação informado: 222.490.578-50 - DATE_ATOM: 2024-12-19T10:30:29-03:00

19 Dec 2024, 10:53:50
CRISTIANO MAX WRASSE **Assinou** - Email: cristiano.wrasse@inpe.br - IP: 150.163.55.151 (150.163.55.151 porta: 39768) - Documento de identificação informado: 592.645.940-00 - DATE_ATOM: 2024-12-19T10:53:50-03:00

19 Dec 2024, 13:36:24
FRANCISCO JAVIER AZPILICUETA **Assinou** - Email: azpi@fcaglp.unlp.edu.ar - IP: 181.1.28.180 (host180.181-1-28.telecom.net.ar porta: 23932) - Documento de identificação informado: Estrangeiro - DATE_ATOM: 2024-12-19T13:36:24-03:00

20 Dec 2024, 09:54:27
RODRIGO SÁVIO PESSOA **Assinou** - Email: rspessoa@ita.br - IP: 177.95.18.159 (177-95-18-159.dsl.telesp.net.br porta: 55648) - Documento de identificação informado: 278.174.178-73 - DATE_ATOM: 2024-12-20T09:54:27-03:00

21 Dec 2024, 06:40:52
ALYSSON BRHIAN DE SOUZA MUNIZ SILVA **Assinou** - Email: alysson_brhian@outlook.com - IP: 138.122.121.91 (138-122-121-91.host.stylosnet.com.br porta: 29114) - Documento de identificação informado: 965.292.022-34 - DATE_ATOM: 2024-12-21T06:40:52-03:00

23 Dec 2024, 08:57:59
ERICO LUIZ REMPEL **Assinou** (91008171-4147-4899-bb44-2dbb42e2f279) - Email: erico_rempel@yahoo.com.br - IP: 161.24.0.40 (161.24.0.40 porta: 58700) - Documento de identificação informado: 260.586.088-48 - DATE_ATOM: 2024-12-23T08:57:59-03:00

Hash do documento original
(SHA256):e54e5b1677369b89491f330ab9c982df0d93615a7688b8cb5506f87a29599115
(SHA512):0672a41bf3daea4d98eadf81c1e901c199150cb1e3934b8501270f6684f847a1b52a93a227db60a0bdc59ec3b7fa09e9c87700187e926e233f952c5a4e331680

Esse log pertence **única** e **exclusivamente** aos documentos de HASH acima

FOLHA DE REGISTRO DO DOCUMENTO

1. CLASSIFICAÇÃO/TIPO	2. DATA	3. DOCUMENTO Nº	4. Nº DE PÁGINAS
TD	18 of December of 2024	DCTA/ITA/TD-065/2024	143

5. TÍTULO E SUBTÍTULO:

Statistical Study of Gravity Waves in the Lower Atmosphere and Predictive Modeling of Low Latitude Ionospheric Irregularities

6. AUTOR(ES):

Alysson Brhian de Souza Muniz Silva

7. INSTITUIÇÃO(ÕES)/ÓRGÃO(S) INTERNO(S)/DIVISÃO(ÕES):

Instituto Tecnológico de Aeronáutica – ITA

8. PALAVRAS-CHAVE SUGERIDAS PELO AUTOR:

Gravity Waves; Lower Atmosphere; Ionosphere; Model Linear Generalized

9. PALAVRAS-CHAVE RESULTANTES DE INDEXAÇÃO:

Ionosfera; Ondas de gravidade; Baixa atmosfera; Densidade de energia; Transformada Rápida de Fourier; Métodos dos Mínimos Quadrados; Plasmas (Física); Física.

10. APRESENTAÇÃO: **(X) Nacional** **( ) Internacional**

ITA, São José dos Campos. Curso de Doutorado. Programa de Pós-Graduação em Física. Área de Dinâmica Não-Linear e Sistemas Complexos. Orientador: Prof. Dr. Marco Antonio Ridenti; coorientadores: Profª. Drª. Marisa Roberto (*in memorian*); Prof. Dr. Francisco Azpilicueta. Defesa em 17/12/2024. Publicada em 2024.

11. RESUMO:

This thesis presents a detailed statistical analysis of gravity waves (GWs) in the lower atmosphere over the Brazilian region, as well as a predictive model for ionospheric irregularities at low latitudes. In the context of the GWs, the study evaluates wind and temperature profiles to determine the kinetic and potential energy densities of GWs using a comprehensive dataset from radiosonde measurements from the Instituto de Controle do Espaço Aéreo (ICEA). Seasonal and spatial variations were investigated using Hierarchical Clustering, Fast Fourier Transform, and Least Squares Method analyses. The results reveal that the kinetic and potential energy densities of GWs exhibit well-defined seasonal and spatial patterns, clustered regionally. In the context of the ionosphere, a Generalized Linear Model (GLM) was developed to predict ionospheric conditions by training on Total Electron Content (TEC) data collected over 12 years in Brasília station (15°S, 47°W). The model includes independent variables such as time, solar flux, geomagnetic index and solar position parameters. The optimized GLM demonstrated high accuracy in discriminating between regular and irregular ionospheric states, improving our understanding of TEC variability and its influencing drivers. The model developed achieved over 90% accuracy in predicting ionospheric irregularities, outperforming existing models in the literature. This dual investigation advances both our knowledge of atmospheric GWs and the predictability of ionospheric irregularities, providing insights for space weather-related applications in navigation and communication systems.

12. GRAU DE SIGILO:

(X) OSTENSIVO **( ) RESERVADO** **( ) SECRETO**